Technical Report
TR-20-13
September 2020

Assessment of the formation of a cavity after the loss of bentonite

Part 1

Analysis of homogenization and appearance of a cavity during erosion of bentonite buffer material

Part 2

Formation and growth of cavities in buffer due to erosion

Lennart Börgesson
Jan Hernelind
Mattias Åkesson

SVENSK KÄRNBRÄNSLEHANTERING AB

SWEDISH NUCLEAR FUEL
AND WASTE MANAGEMENT CO

Box 3091, SE-169 03 Solna
Phone +46 8 459 84 00
skb.se

SVENSK KÄRNBRÄNSLEHANTERING

ISSN 1404-0344
SKB TR-20-13
ID 1890562

September 2020

Assessment of the formation of a cavity after the loss of bentonite

Part 1

Analysis of homogenization and appearance of a cavity during erosion of bentonite buffer material

Lennart Börgesson, Clay Technology AB

Jan Hernelind, Scanscot Technology AB

Part 2

Formation and growth of cavities in buffer due to erosion

Mattias Åkesson, Svensk Kärnbränslehantering AB

A pdf version of this document can be downloaded from www.skb.se.

© 2020 Svensk Kärnbränslehantering AB

Preface

An assessment regarding the formation and growth of a cavity in the buffer due to bentonite erosion has been performed. This report presents two different approaches for investigating these processes.

Jan Hernelind sadly passed away in the beginning of 2020 after a short time of disease. His contributions to modelling different scenarios with the finite element code Abaqus, reported here and in other reports, were necessary and irreplaceable. His modelling skill was outstanding and he never gave up but always came to a solution however difficult the problem seemed to be.

Contents

Part 1

Analysis of homogenization and appearance of a cavity during erosion of bentonite buffer material

Lennart Börgesson, Clay Technology AB

Jan Hernelind, Scanscot Technology AB

Abstract

The report is a description of the work to model the homogenization during colloid erosion with the FEM program Abaqus. The purpose of the calculations is to analyze how erosion affects the density distribution in a deposition hole as a function of time and erosion rate and to conclude how and when a cavity can be created at some stage of the erosion process. The erosion rates considered are 10 g/year and 150 g/year, which are derived by Neretnieks et al. (2017).

The idea of these calculations has been to include the erosion rate and model the swelling rate and by this investigate how the density distribution evolves with time and thus also investigate if there at any time may be a cavity created. Abaqus includes an adaptive subroutine that models loss of material with time by displacing a boundary with a specified rate. The swelling of the material is simultaneously modelled by re-meshing. By adapting the displacement rate to the erosion rate the correct material loss can be simulated.

As common in multiphysics problems with complex geometries, the convergence was problematic and simplifications of the geometry had to be done. The erosion has been assumed to take place in a horizontal fracture intersecting the entire rim of deposition hole in the centre of the canister. The investigation has led to the following results and conclusions:

- The mass loss can be well modelled with the Abaqus erosion subroutine that prescribes a constant displacement rate of the erosion front.
- The erosion process can be coupled to the swelling and homogenization processes modelled with the Porous Elastic and Drucker-Prager Plasticity models as well as the Claytech Plastic Cap model.
- The geometry of the erosion front had to be “simplified” in order to get any results since point erosion, corresponding to line erosion in the axial symmetric geometry, could not be modelled.
- A way to model the erosion with applying a small half donut on the rock surface in the deposition hole and use that donut surface as erosion front was tested. The erosion and subsequent homogenization were possible to model to a limited extent of erosion that corresponded to about 100 kg bentonite lost. Then it was not possible to continue the calculation due to convergence problems (probably due to buckling caused by high radial pressure for the innermost elements).
- The simplified assumption by applying the erosion front in a horizontal symmetry plane along the fracture through the buffer was at first tested with a very high erosion rate. Although the erosion rates and duration times were unrealistic a total erosion of 3 360–4 800 kg was modelled, but these cases are not fully comparable due to the high pore pressure gradients that do not occur at realistic erosion rates.
- At those unrealistically high erosion rates (15–150 kg/year) the cavity was formed earlier, i.e. after less loss of material than at lower erosion rates, since the swelling was not fast enough in order to keep track with the mass loss.
- The final calculations were done with a line erosion front stretching horizontally from the fracture to the canister corresponding to a surface erosion in the axial symmetric geometry. Both material models were used and the studied variation in erosion rate of 10–150 g/year was modelled. The calculations resulted in a total mass loss of between 5.1 and 7.6 tons dry bentonite before the contact in the erosion front was lost depending on the material model and the erosion rate. This corresponds to 4–6 bentonite rings with the thickness 0.5 m.
- At the studied erosion rates the time until contact loss is about inverse proportional to the erosion rate and the eroded mass at formation of a cavity thus independent of the erosion rate.
- The time to lost contact and thus formation of a cavity was 34 000–50 000 years at the erosion rate 150 g/year and 515 000–610 000 years at the erosion rate 10 g/year. The Claytech Plastic Cap model yielded the longest time due to a higher reached void ratio at the lost contact.

- The void ratio at lost contact was rather low (1.6–2.5) due to the material model and the stress situation in the element at the erosion front. Since these void ratios correspond to a swelling pressure between about 80 kPa and 180 kPa it is most probable that the void ratio would be higher and the time to lost contact longer and thus that the eroded mass of bentonite is underestimated at lost contact.
- In addition, the simplified geometry of a line erosion instead of a point erosion is expected to underestimate the time to when the cavity comes in contact with the canister and thus also the eroded mass.
- The influence of changing the hydraulic boundary condition at the erosion front to no flow boundary was found to be insignificant except for in the very beginning of the calculation.
- The influence of the friction angle between the rock surface and the bentonite was found to be rather significant. An increase in friction angle from 5.7° to 8.5° decreased the time and thus also the amount of bentonite lost until a cavity was formed with about 25 %.
- The influence of the initial density of the buffer was found to be rather insignificant for the acceptable ranges of buffer density.

The overall conclusion is that there will not be any open cavity stretching from the fracture to the canister until the dry bentonite mass lost is larger than 5 tons and that this figure most probably is an underestimation.

Sammanfattning

Rapporten beskriver det arbete som gjorts för att med FEM-programmet Abaqus modellera homogeniseringen av bufferten efter och under en kolloiderosion. Syftet med beräkningarna är att analysera hur erosionen påverkar densitetsfördelningen i ett deponeringshål som en funktion av tiden och erosionshastigheten och för att konkludera hur och när en kavitet kan uppstå vid något tillfälle under erosionsprocessen. De erosionshastigheter som beaktats är 10 g/år och 150 g/år, vilka härletts av Neretniks et al. (2017).

Avsikten med dessa beräkningar har varit att inkludera erosionshastigheten och modellera svällningshastigheten och därigenom undersöka hur densitetsfördelningen utvecklas med tiden och alltså också undersöka om det vid något tillfälle kan uppstå en kavitet. Abaqus innehåller en adaptiv funktion som modellerar förlust av material med tiden genom att förskjuta en rand med en specificerad hastighet. Materialets svällning modelleras simultant genom re-meshing (förnyande av elementnätet). Genom att anpassa förskjutningshastigheten till erosionshastigheten kan den avsedda materialförlusten simuleras.

Såsom ofta är fallet i beräkningar med många fysiska processer med komplicerade geometrier, medförde beräkningarna konvergensproblem och förenklingar av geometrin behövde göras. Erosionen antogs äga rum i en horisontell spricka som omger hela deponeringshålets rand i kapselns mitt. Beräkningarna ledde till följande resultat och slutsatser:

- Massförlusten kan modelleras med den använda Abaqus adaptiva funktionen som beskriver en konstant förskjutningshastighet av erosionsranden.
- Erosionsprocessen kan kopplas till svällnings- och homogeniseringsprocesserna som modelleras med elasticitetsmodellen Porous Elastic och plasticitetsmodellerna Drucker-Prager och Claytech Plastic Cap.
- Geometrin hos erosionsranden behövde ”förenklas” för att få genom beräkningarna eftersom punkterosion, som motsvara linjeerosion vid axialsymmetri, inte fungerade.
- En teknik att modellera erosion genom att lägga in en ”halv donut” i bentoniten mot bergytan och använda dess yta som erosionsrand testades. Erosionen och medföljande homogenisering gick att modellera till en gräns som motsvarade cirka 100 kg förlust av bentonit. Därefter kunde inte beräkningen drivas vidare pga konvergensproblem (antagligen pga av buckling av de innersta elementen orsakad av höga radiella tryck).
- Den förenklade modellen med en erosionsfront i ett horisontellt symmetriplan genom bufferten längs sprickan prövades först med en mycket stor erosionshastighet. Fastän erosionshastigheten och tiden var orealistiska resulterade beräkningarna i en total erosion på 3 360–4 800 kg, men dessa fall är inte helt relevanta och jämförbara med de realistiska fallen pga de alltför höga portrycksgradienterna.
- Vid dessa orealistiskt höga erosionshastigheter (15–150 kg/år) uppkom en kavitet tidigare, dvs efter mindre materialförlust, än vid låga erosionshastigheter, eftersom svällningen inte är tillräckligt snabb för att hålla stånd mot materialförlusten.
- De slutliga beräkningarna gjordes med en rotationssymmetrisk modell med en erosionsrand som sträcker sig horisontellt från sprickan till kapseln och alltså motsvarar en erosionsyta. Båda materialmodellerna användes och erosionshastigheten 10–150 g/år modellerades. Beräkningarna resulterade i en total massförlust på mellan 5,1 och 7,6 ton torr bentonit innan kontakten i erosionsfronten tappades. Totala mängden var beroende på materialmodellen och erosionshastigheten. Detta motsvarar 4–6 bentonitringar med tjockleken 0,5 m.
- Beräkningarna visar att vid de aktuella erosionshastigheterna är tiden till tappad kontakt ungefär omvänt proportionell mot erosionshastigheten och alltså den totala eroderade massan då en kavitet bildas oberoende av erosionshastigheten.

- Tiden tills kontakten förlorades och alltså tiden till en kavitet bildades var 34 000–50 000 år vid erosionshastigheten 150 g/år och 515 000–610 000 år vid erosionshastigheten 10 g/år. Materialmodellen Claytech Plastic Cap gav den längsta tiden eftersom den medgav ett högre portal innan kontakten tappades.
- Det modellerade portalet vid förlorad kontakt var ganska lågt (1,6–2,5) på grund av materialmodellen och spänningstillståndet i elementet vid erosionsranden. Dessa portal motsvarar ett svälltryck på mellan 80 kPa och 180 kPa som borde hålla ihop bentoniten. Det är alltså troligt att i ett verkligt fall, tiden till förlorad kontakt är längre och att den totala eroderade massan då en kavitet bildas är underskattad i beräkningarna.
- Dessutom förväntas den förenklade rotationssymmetriska geometrin med linjeerosion istället för punkterosion underskatta tiden tills kaviteten sträcker sig till kapseln och alltså även den totala eroderade massan.
- En förändring av det hydrauliska randvillkoret i bergytan från att ha fri tillgång till vatten till att ha ingen tillgång till vatten påverkade förloppet obetydligt förutom i början av beräkningen.
- Beroendet av friktionsvinkeln mellan bergytan och bentoniten var ganska liten. En ökning av friktionsvinkeln från 5.7° till 8.5° minskade tiden och alltså mängden eroderad bentonit tills en kavitet uppstod med ungefär 25 %.
- Beroendet av densiteten hos den installerade bufferten befanns också vara mycket liten vid de densitetsvariationer som accepteras.

Den övergripande slutsatsen är att en kavitet som sträcker sig från sprickan till kapseln uppstår inte förrän bufferten förlorat mer än 5 ton torr bentonit genom kolloiderosion och att denna mängd förmodligen är underskattad.

1 Background

SKB has been requested by the Swedish Radiation Safety Authority SSM to complete the motivation why a naked area on the canister wall cannot take place after colloid erosion of bentonite in a deposition hole. The present report is a description of the work to model the homogenization during colloid erosion. The purpose of the new calculations is to analyze how erosion affects the density distribution in a deposition hole as a function of time and erosion rate and to conclude how and when a cavity can be created at some stage of the erosion process. The erosion rates considered are 10 g/year and 150 g/year, which are derived by Neretnieks et al. (2017).

The task has been divided into two parts. Part A of this task is to define and motivate the models to be used, the parameters of those models and the assumptions made for the modelling. Part B is to do the actual modelling, a sensitivity analysis and comparison with earlier homogenization calculations. This report describes the work done in both parts and also the attempts and tests to simulate erosion with finite element modelling and the subsequent swelling and homogenization of the bentonite in the deposition hole. Part A is mainly included in Chapters 2-4 and part B in Chapter 5.

2 Modelling strategy

The FEM code Abaqus has been used. This code was used in earlier calculations of self-healing and homogenization after either loss of bentonite that created a cavity or when 1–3 bentonite rings were missing after installation (Åkesson et al. 2010a). The latter could also be regarded as a large cavity created by erosion.

Since the earlier calculation did not consider the erosion rate or the homogenization rate it was not possible to judge whether there at some stage of the erosion actually existed a cavity in the buffer although the very slow erosion rate makes it very probable that the swelling and closing of the hole will be so fast that there will not be any open cavity until after long time when the bentonite has lost so much in density that the homogenization is insufficient.

The idea in the new modelling is to include the erosion rate and model the swelling rate and by this investigate how the density distribution evolves with time and thus also investigate at what time a cavity may be created. Abaqus has included a user defined subroutine that models loss of material with time by displacing a boundary with a specified rate. The swelling of the material is simultaneously modelled by re-meshing. By adapting the displacement rate to the erosion rate the correct material loss can be simulated.

This procedure had not been used before in Abaqus for swelling bentonite and for the geometries of a deposition hole. Therefore, at first the erosion process combined with the swelling process was tested and the possibility to include a growing circular cross section was investigated. Then the actual modelling of the process was done with the appropriate geometry that could be modelled and with realistic erosion rates.

3 Definition of models and data

3.1 General

The material model of the bentonite has been developed and tested during different tasks and projects during the last 20 years. The model and the data are used in SR-Site and described by Åkesson et al. (2010a, b). The model has been further developed and tested in the TF EBS (Task Force for Engineering Barrier Systems) and reported in Börgesson et al. (2020). The parameters used here for the erosion modelling are the data derived in that project. They differ slightly from the parameters used in SR-Site and in addition another model has also been developed and used.

3.2 Material models and parameters

3.2.1 Mechanical models of the buffer

Two slightly different models are used. The models are in detail described in Börgesson et al. (2020) and Dueck et al. (2019) and will not be described here in detail. They consist of one elastic model (Porous Elastic), which is the same for both models, and one plastic model, which differ. The two plastic models are Drucker-Prager Plasticity model and Claytech Plastic Cap model.

The effective stress theory for completely water saturated bentonite is applied:

$$p = p_t - u$$

where p = effective mean stress, p_t = total mean stress and u = pore water pressure.

Porous Elastic

Porous Elastic is in Abaqus defined as a logarithmic relation between the void ratio e and the mean effective stress p according to Equation 3-1.

$$\Delta e = -\kappa \cdot \Delta \ln p \qquad (3\text{-}1)$$

where κ = porous bulk modulus

Poisson's ratio v is also required.

For the Drucker-Prager model the following values are used (same as in SR-Site):

$\kappa = 0.21$

$v = 0.3$

For the Claytech Plastic Cap model the following values are used (updated and derived by calibration calculations in Börgesson et al. (2020)):

$\kappa = 0.175$

$v = 0.3$

This relation is not valid for low densities (see Börgesson et al. 1995) but only in the interval $0.7 < e < 1.5$, which correspond to 1 110 kg/m$^3 < \rho_d <$ 1 635 kg/m^3. At lower densities the porous bulk modulus is much larger ($\kappa \approx 1.37$) but this change in modulus is not included in the model. If swelling causes a lower density the swelling will not be correctly modelled for that part. For lower density the model is in better agreement with the behaviour of MX-80 at high salinity or after Ca-conversion.

Drucker-Prager Plasticity model

This model is included in Abaqus standard. The parameters are the same as used in SR-Site.

Drucker-Prager Plasticity contains the following parameters:

β = friction angle in the p-q plane
d = cohesion in the p-q plane
Ψ = dilation angle
$q = f(\varepsilon^{d}_{pl})$ = yield function

The parameter values in this model are as follows:
$\beta = 17°$
d = 100 kPa
$\Psi = 2°$
$q = f(\varepsilon_{pl})$ according to Table 9-1.

Table 9-1. Yield function.

q **(kPa)**	$\boldsymbol{\varepsilon}_{\mathbf{pl}}$
112	0
138	0.005
163	0.02
188	0.04
213	0.1

Figure 3-1 illustrates the Drucker-Prager model.

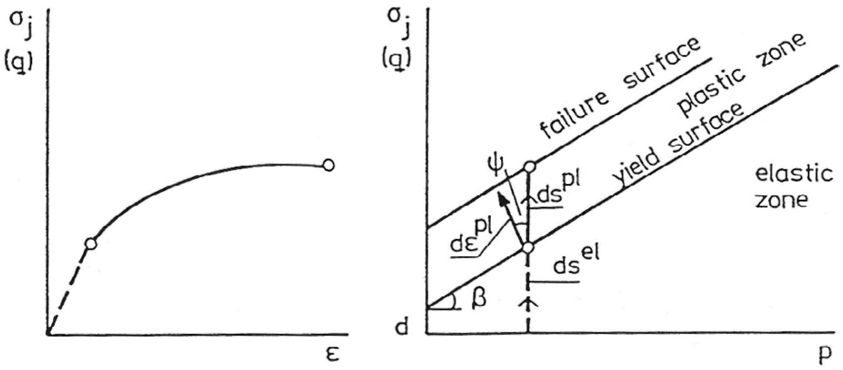

Figure 3-1. *Illustration of the Drucker-Prager model.*

Claytech Plastic Cap model

This model has been developed for bentonite and implemented in Abaqus. The parameters of the model were calibrated and validated in Börgesson et al. (2020), where they are also defined and described.

Claytech plastic cap model

$a = 2.45$
$c = 2.20$
$b = 0.77$
$K = 1.0$
$\gamma = 0.2$
$R = 0.1$
$p_b = 30\,000$ kPa
$p_f = -25\,000$ kPa

Cap hardening = see Table 9-2

Table 9-2. Cap hardening function.

p (kPa)	$^e\log(1+\varepsilon^v_{pl})$
100	0
331	0.1133
934	0.2112
2 160	0.2904
3 247	0.3289
4 294	0.3553
8 240	0.4169
10 044	0.4356
12 530	0.4565
13 299	0.4621
17 562	0.4884
30 000	0.5390

3.2.2 Hydraulic model of the buffer

The hydraulic conductivity relation is shown in Table 9-3 (see Section 3.4 in Börgesson et al. 2020).

Table 9-3. Hydraulic conductivity as a function of void ratio.

e	k (m/s)
0.45	0.5×10^{-14}
0.70	4.0×10^{-14}
1.00	2.0×10^{-13}
1.5	1.0×10^{-12}
2.00	0.5×10^{-11}
3.00	1.0×10^{-11}
5.00	3.5×10^{-11}
10.00	1.5×10^{-10}
20.00	0.75×10^{-9}

3.2.3 Other parts

The rock and the canister are modelled as very stiff elastic materials with no pore pressure elements, i.e. impervious.

3.3 Contact properties

The shear resistance between bentonite and a steel surface has been investigated with a large number of friction tests and long tube tests (see e.g. Dueck et al. 2019).

The results have yielded an average friction angle of $\phi_c = 7.2°$ at completed swelling when the surface of the steel was very raw (1 mm deep grooves) at a swelling pressure varying from 200 kPa to 6 MPa along the tube.

Some calculations for investigating the modelling capability have also been made with no friction between the rock or canister and the bentonite in order to simplify the initial calculations.

The final calculations were done with contact surfaces between the bentonite and the rock or the canister with friction and the Mohr Coloumb friction angle

$\phi_c = 7.2°$

3.4 Initial conditions

The bentonite is assumed to be completely water saturated from start with full swelling pressure applied. The initial conditions are

$e_0 = 0.70$
$p_0 = 10\,000$ kPa
$u_0 = 0$ kPa

$e = 0.7$ corresponds to the density at saturation $\rho_m = 2\,047$ kg/m^3 and the dry density $\rho_d = 1\,635$ kg/m^3. At the sensitivity analyses also the initial void ratio 0.77 was used and the corresponding initial swelling pressure 7 000 kPa. These relations were round numbers taken from Börgesson et al. (1995).

3.5 Boundary conditions

Mechanical boundaries of the rock: fixed nodes.

Hydraulic boundaries:

- Between the rock surface and the bentonite: pore water pressure 0 kPa.
- The upper bentonite surface: no flow.
- The erosion front: either fixed pore water pressure 0 kPa or no flow boundary.

The hydraulic boundary conditions between the rock surface and the bentonite means that water is modelled as being freely available at the rock surface. This is motivated by the very slow erosion rate that requires very slow water inflow into the deposition hole. The erosion means that the water volume required to replace the lost dry mass of bentonite is

$$dV/dt = d(m_s/\rho_s)/dt = (0.01 \text{ to } 0.15\text{kg/y})/2\,780 \text{ kg/m}^3 = 3.6 \times 10^{-6} \text{ to } 5.4 \times 10^{-5} \text{ m}^3\text{/y} = 0.0036 \text{ L/y} =$$

$$= 7 \times 10^{-9} \text{ to } 1 \times 10^{-7} \text{ L/min.}$$

Thus, the rock may supply water enough to replace eroding bentonite even if the inflow rate from the rock matrix is as low as 1×10^{-7} L/min into a deposition hole.

3.6 Motivation for the used models and parameters

The values used for the Drucker-Prager model are motivated by that they were used in SR-Site and yielded good results at the modelling of the SH1 test (Self Healing test) (Börgesson et al. 2020). The values used for the Claytech Plastic Cap model are motivated by that they were calibrated and validated at the modelling of the small scale HR (High Resolution) tests (Börgesson et al. 2020).

3.7 Erosion model and erosion rate

According to Neretnieks et al. (2017) the erosion rate will be in the interval 10–150 g/year (see Section 5.1).

The erosion has been modelled according to the following description (ABAQUS 2017):

Adaptive meshing, using Abaqus/Standard, can model effects of ablation, or wear, by enabling definition of boundary mesh motions independent of the underlying material motion. An example is the wearing of a tire during its life, an effect that can significantly affect the performance of the structure.

Adaptive meshing in Abaqus/Standard uses a single smoothing algorithm that works well for the modeling of ablation processes

ALE adaptive meshing in Abaqus/Standard:

- maintains a topologically similar mesh,
- can be used to model effects of ablation, or wear (in which material is eroded at the boundary),
- can be used in static stress/displacement analysis, steady-state transport analysis, coupled pore fluid flow and stress analysis, and coupled temperature-displacement analysis,
- can be used only in geometrically nonlinear general analysis steps.
- Nodes in the interior region are defined as nodes that are surrounded entirely by elements in the adaptive mesh domain. By default, the new position of an interior node is computed from the positions of the adjacent nodes that are connected through element edges to the node in question. These nodes can move in any direction.
- To control the displacement of these nodes, an adaptive mesh constraint can be applied in any direction.
- Surface nodes are defined as nodes at which the surrounding surface facets have the same normal vector within a user-defined angle. These nodes are constrained against movement in the normal direction but sliding in any tangential direction is permitted. The new position of a surface node is computed from the positions of the adjacent nodes that are connected through the edges of the surface facets to the node in question.
- Edge nodes are nodes in a three-dimensional model at which the surrounding surface facets have two different normal directions and where the vectors along two of the surface edges are colinear. Nodes on an edge can slide only along the edge. The new position of an edge node is computed from the positions of the two adjacent nodes along the edge.
- Corner nodes are nodes at which all the surrounding surface facet normal directions are different. These nodes are constrained against all mesh smoothing movement.
- The displacement of these node types on the boundary region can be controlled by applying an adaptive mesh constraint in any direction.
- In most adaptive mesh problems, the motion of nodes in the mesh is determined by the mesh smoothing algorithm, with constraints imposed by the domain boundary and the boundary region edges. However, there may be cases when there is a need to define the motion of the nodes explicitly or to keep certain nodes fixed, to move nodes in a particular direction, or to force certain nodes to move with the material.
- Adaptive mesh constraints give the flexibility to define the motion of the node explicitly.
- Spatial mesh constraints are applied to define the motion of the nodes explicitly. Spatial mesh constraints allow full control over the mesh movement and can be applied to any node except those that have Lagrangian mesh constraints applied to them.
- The spatial mesh constraints can be prescribed via user subroutine UMESHMOTION. The user subroutine allows to have the spatial mesh constraints depend on available nodal or material point information.

Displacement constraints define a node's displacement relative to its original coordinates. Use a displacement constraint to control a node's motion to a specific coordinate location.

The Abaqus/Standard implementation of adaptive meshing has the following limitations:

- Initial mesh sweeps cannot be used to improve the quality of the initial mesh definition.
- Diagnostics capabilities are currently limited.

Spatial mesh constraint is applied without regard to the current material displacement at the node. This behavior allows to prescribe mesh motion that differs from the current material displacement at the free surface of the adaptive mesh domain, effectively eroding, or adding, material at the boundary. Using adaptive mesh constraints this way is an effective technique for modeling wear or ablation processes. In addition, for general boundary shapes the most effective interface for ablation is the user defined subroutine UMESHMOTION, where spatial mesh constraints can be applied to the nodes on the free surface in general ways according to solution-dependent variables, if needed. The user subroutine interface provides a local coordinate system that is normal to the free surface at the surface node, enabling mesh motions definitions in this local system.

4 Element mesh and calculations made to test the possibility to model erosion and homogenization

4.1 General

The erosion process in Abaqus has not been used on swelling bentonite before so in order to understand the possibility to use it in combination with the swelling and homogenization models and evaluate the capability, a number of modelling tests have been performed.

The geometry is illustrated in Figure 4-1.

The dimensions are equal to the dimensions of the reference deposition hole and canister.

Canister:

Diameter 1.05 m
Height 5.0 m

Buffer:

Outer diameter 1.75 m
Height below the canister 0.5 m
Height above the canister 1.5 m

The eroding fracture is assumed to be located as a horizontal plane intersecting the deposition hole at the center of the canister. The erosion front is thus at the periphery of the entire deposition hole. In order to simplify the geometry, the fracture is made a symmetry plane and only the upper part is modelled. This means that the total mass of the bentonite below the canister is too large but as concluded later this does affects the results very little and does not affect the conclusions of the modelling. The geometry is 2D axial symmetric around the vertical center of the deposition hole.

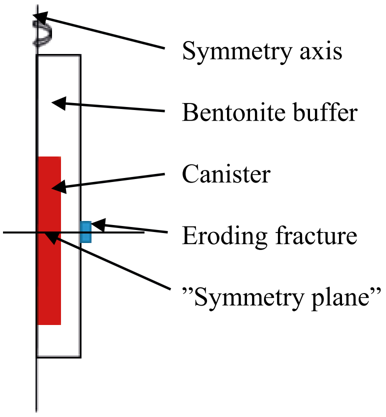

Figure 4-1. *Illustration of the geometry.*

4.2 Expanding half "donut"

The erosion procedure requires the there is an erosion front that moves in a specified way so a point or line source cannot be used. The geometry of the eroded cavity is instead assumed to be like a growing half donut or expanding half circle in a vertical cross section (SKB 2010). This makes it necessary to include such a boundary where the donut starts to expand inwards. The element mesh shown in Figure 4-2 was at first used in order to test the erosion procedure. A very small half donut added to the rock surface was applied as an erosion front. Then the material loss was modelled by moving the erosion front as shown in the figure. At the same time as the front is moving the mesh is re-meshed and swells back towards the rock.

The Drucker-Prager plasticity model was used in this calculation together with the models and parameter values described in Chapter 3.

Due to convergence problems, the front could not be moved far enough to simulate the large erosion that is requested. New improved element meshes were tested. Also the rock surface half donut erosion front size was increased. Figure 4-3 shows the last one. In this calculation there was no friction between the rock and the buffer. This model stopped converging after about 100 kg bentonite was lost. The erosion rate was quite high or about 2 kg/year, which corresponds to 4 kg/year due to the symmetry plane. Figure 4-4 shows the element mesh and the resulting void ratio distribution at the end of the calculation. Figure 4-5 shows the total eroded volume as a function of time. In spite of the fast erosion there was no cavity that evolved during the erosion.

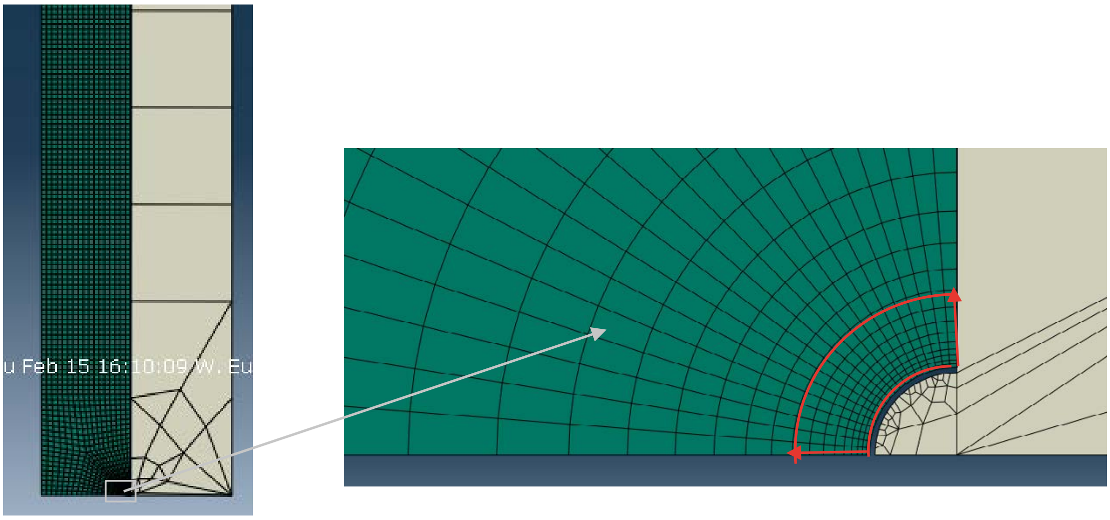

Figure 4-2. *Element mesh used to test the erosion and swelling procedures. A small inner half donut was applied in the rock in order to have an erosion front from where the cavity can grow. The red quarter circles show the erosion front that moves according to the arrows.*

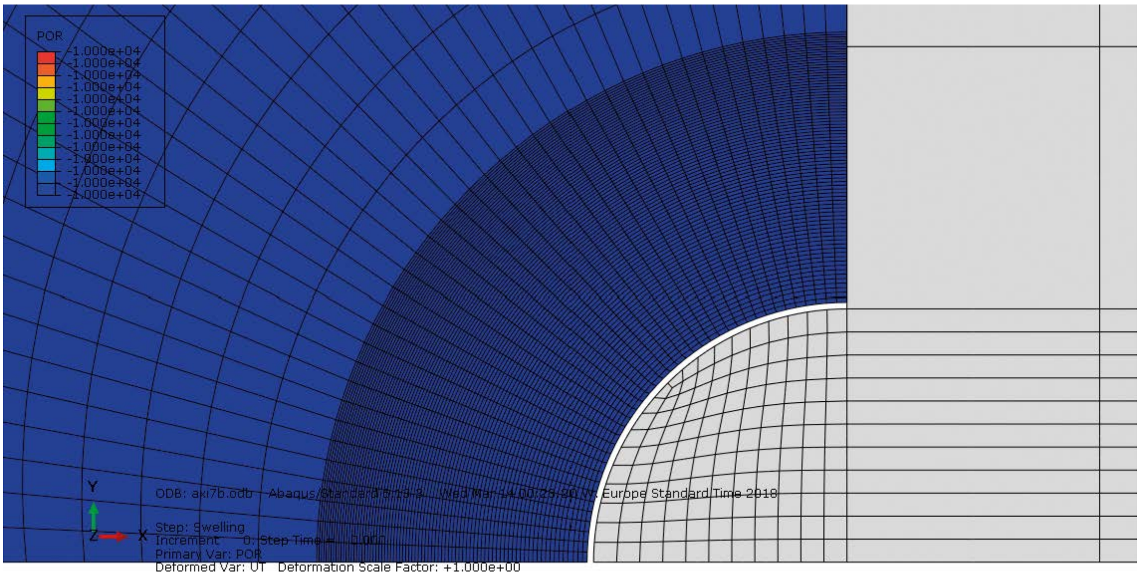

Figure 4-3. *New element mesh. Enlargement of the erosion front area.*

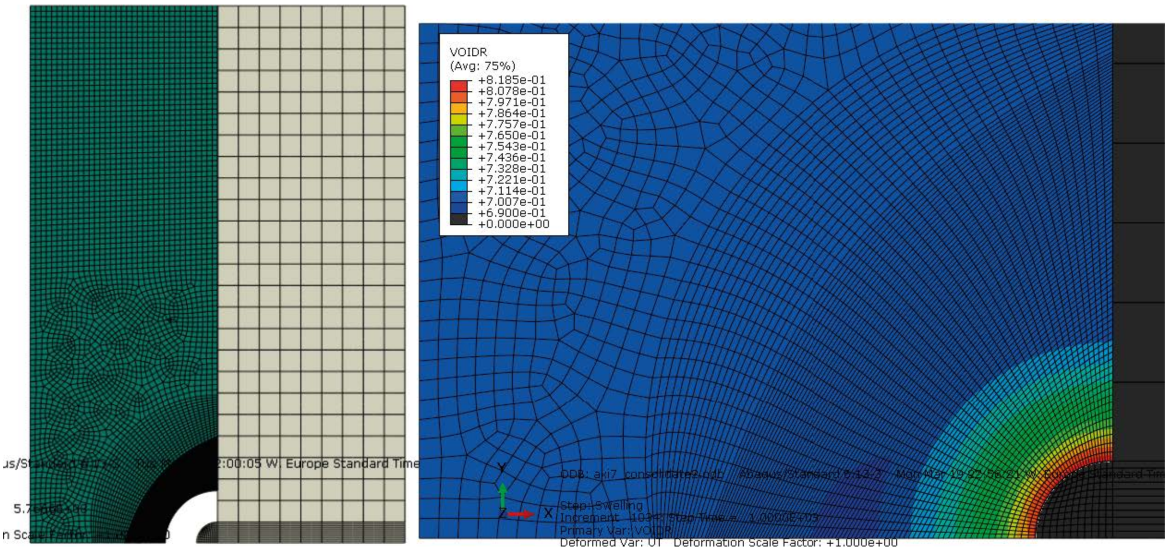

Figure 4-4. *Expansion of the erosion front (left) and the resulting void ratio distribution at the end of the calculation. Observe that the cavity never evolves so the left element mesh only describes the fictive movement of the erosion front.*

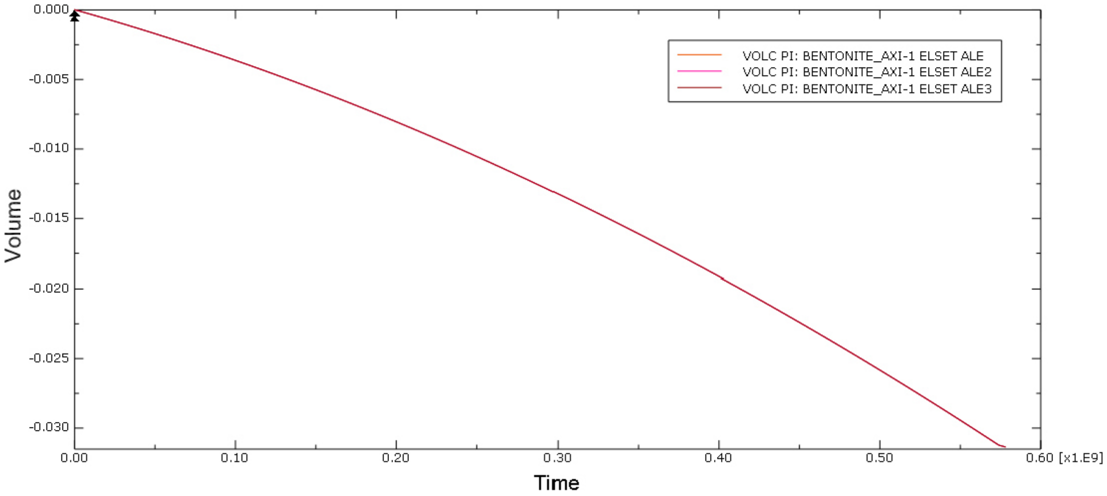

***Figure 4-5.** Eroded volume (m^3) of buffer at its original density as a function of time (s). The erosion thus continued for about 19 years and then stopped due to convergence problems. A total mass of about 100 kg was lost.*

4.3 Expanding horizontal surface

4.3.1 General

The problems with convergence of the expanding half donut calls for another solution. A reason for the lack of convergence in the geometry used is the strong deformation of some of the elements that degenerates the elements, which in turn is caused by the swelling geometry that forces the elements to shrink towards the small donut surface. A much simpler geometry would be to have a more linear swelling.

Such a geometry is shown in Figure 4-6, where the symmetry plane in the buffer is used as the erosion front. This is of course not in agreement with the actual erosion scenario, where the bentonite is lost in a small rim at the rock surface. However, if this simplified boundary condition with an erosion front stretching all the way into the canister can lead to completed calculations the results would be very useful for evaluating the consequences of erosion. In particular they would be rather pessimistic concerning the density distribution close to the canister. However, they are very relevant for investigating if there can be a cavity stretching all the way between the rock and the canister as indicated in Figure 4-2 in SKB (2010).

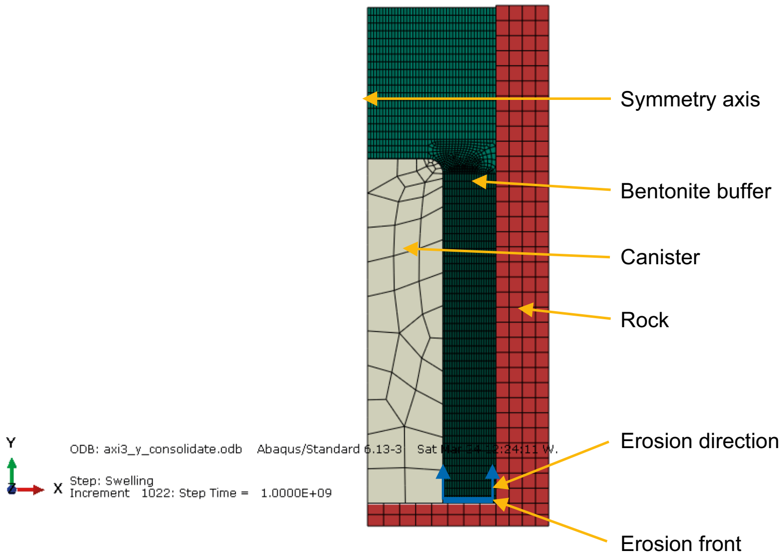

***Figure 4-6.** Geometry of the element mesh with a horizontal erosion front in the "symmetry plane".*

Some preliminary calculations were at first done in order to check the modelling technique and the results. The geometry and erosion front shown in Figure 4-6 were used. These results are shown in Chapter 4 while the actual final modelling is presented in Chapter 5.

4.3.2 Drucker-Prager model

Erosion rate 150 kg/year

Also in this calculation the Drucker-Prager plasticity model was used together with the models and parameters shown in Chapter 3. In order to test the behavior, at first a very high constant erosion rate was tested, about 75 kg/year for the model shown in Figure 4-6. This corresponds to a total erosion rate of 150 kg/year, which is 1 000 times higher than the highest predicted erosion rate (Neretnieks et al. 2017).

The results showed that the swelling was not fast enough in order to keep the buffer closed without forming a cavity. The calculation was run until 10^9 seconds or about 32 years, where altogether about 2 400 kg bentonite was eroded. Including the symmetry conditions it means a total bentonite loss of 4 800 kg. Figure 4-7 shows the resulting void ratio distribution at the end of the calculation. The figure shows that a cavity is formed that stretches about 8 cm from the erosion front. The pore water pressure distribution also shown in Figure 4-7 shows that there is still high suction in the bentonite meaning that the swelling is far from completed, which of course is caused by the too fast erosion rate.

4 800 kg bentonite lost would for the erosion rate limits 10 and 150 g/year yield a total erosion time of about 32 000 – 475 000 years.

The modelled eroded volume (equal to half the actual) as a function of time from start of the erosion is plotted in Figure 4-8.

The vertical displacement of the nodes in the erosion front is plotted as function of time in Figure 4-9. The figure shows that the cavity starts forming after about 0.7 × 10^9 seconds (about 22 years) when the nodes starts to move. The rate of the expansion of the cavity then actually increases with time.

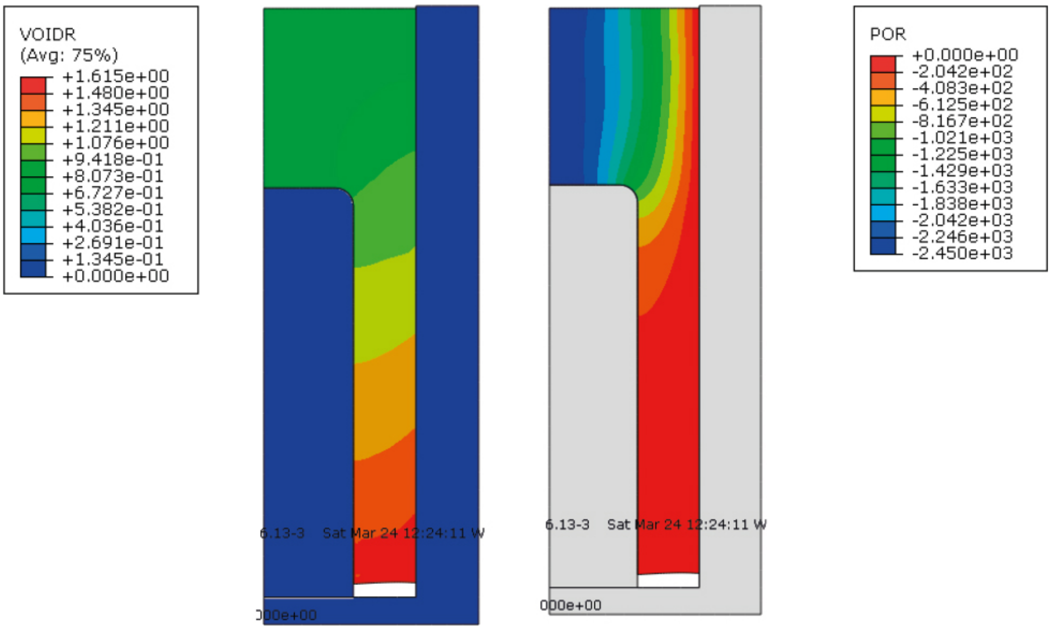

Figure 4-7. *Void ratio distribution (left) and pore water pressure (kPa) at the end of the calculation (32 years) with the total erosion rate 150 kg/year.*

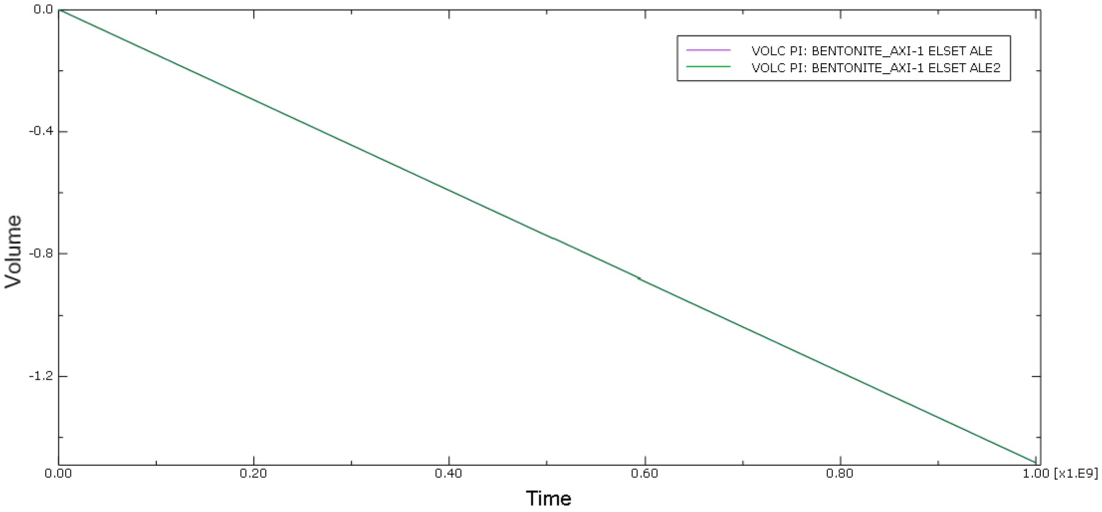

***Figure 4-8.** Half the eroded volume of buffer at its original density (m^3) as function of time (s).*

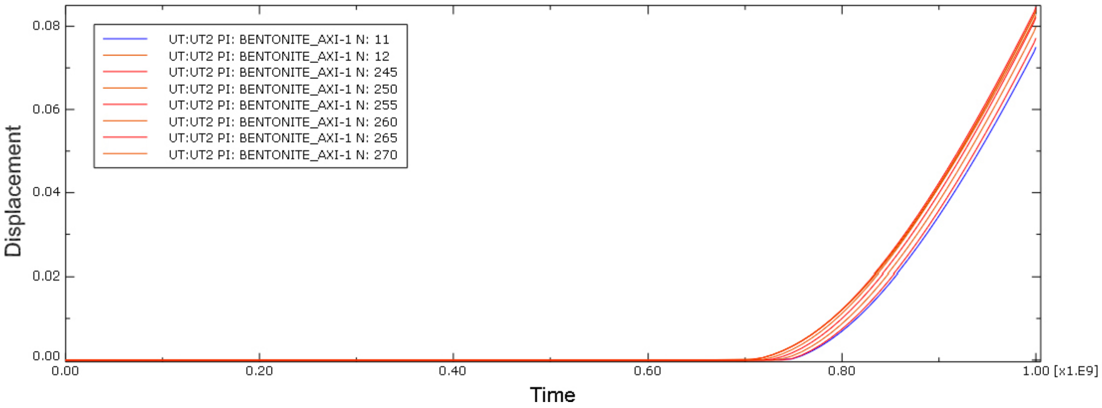

***Figure 4-9.** Vertical displacement of the nodes in the erosion front (m) as function of time (s).*

The contact at the erosion front was thus lost after about 22 years after a total loss of dry bentonite of about 3 360 kg. Considering bentonite rings of 0.5 m thickness, that are planned to be used for the buffer installation, the volume V and dry mass m_s of such a ring are (considering the average void ratio 0.7 used in the calculations)

$V = 0.77\ \text{m}^3$

$m_s = 1\,258\ \text{kg}$

3 360 kg dry bentonite mass thus corresponds to between 2 and 3 bentonite rings.

Erosion rate 15 kg/year

In order to test the behavior with slower erosion rate and longer erosion time the erosion rate was made 10 times lower or about totally 15 kg/year and the calculation was made to run 10 times longer (10^{10} s) with otherwise identical models and conditions. In this calculation the convergence stopped after a little less than 6×10^9 s or about 180 years. Figure 4-10 shows corresponding results at the end of the calculation. Figure 4-11 shows the eroded volume as a function of time from start of the erosion.

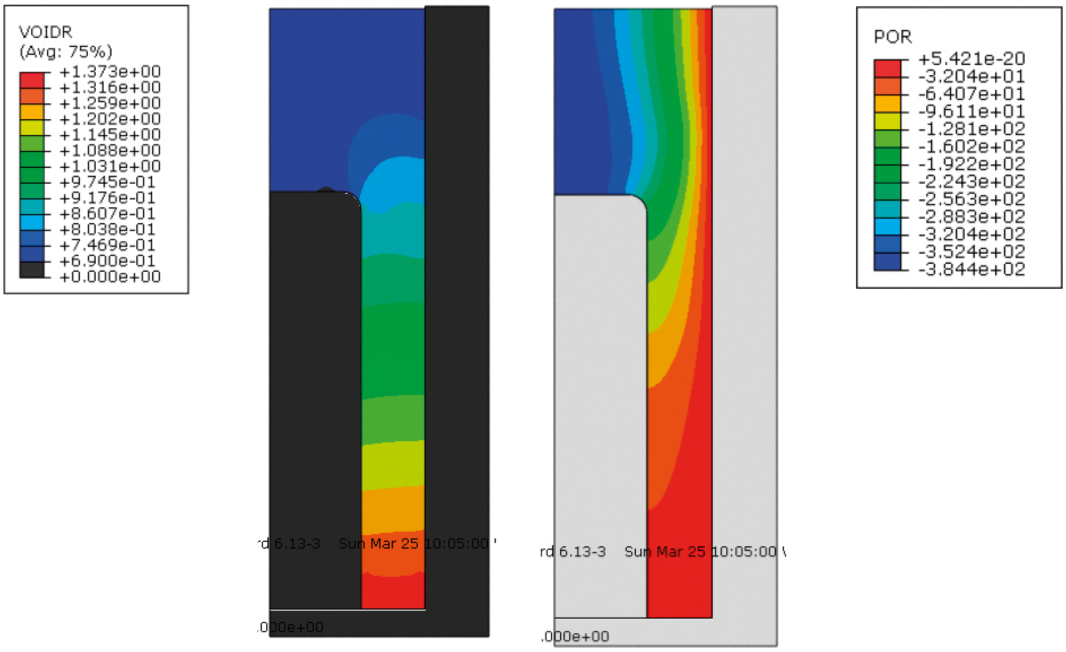

Figure 4-10. *Void ratio distribution (left) and pore water pressure (kPa) with the erosion rate 15 kg/year when the calculation stopped (180 years).*

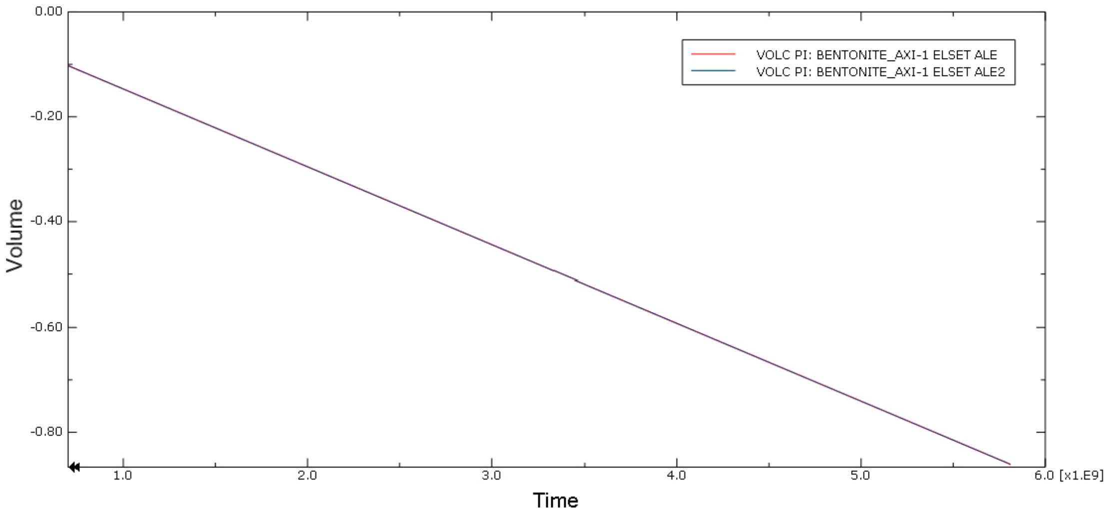

Figure 4-11. *Half the eroded volume of buffer at its original density as a function of time (s) from start of the erosion.*

The calculation stopped when the erosion had continued for 5.8×10^9 s (about 180 years). It is not obvious whether there would have been a cavity also for this case or not. However, the convergence problems occurring at the end of the calculation indicates that the model is very close to loose contact and thus form a cavity. The same problems occurred in the calculation with 150 kg/year erosion but there the problems were overcome and the contact lost. So the conclusion is that the contact is lost close to when the convergence run into large problems and the calculation stops. The total mass lost after 180 years was about 2 800 kg.

The lower erosion rate yields logically lower suction since the pore water has more time to equilibrate.

4.3.3 Claytech Plastic Cap model

Also the Claytech Plastic Cap model was used and tested for the same modelling scenario and element mesh as the Drucker-Prager model. In this calculation the erosion rate was the same as the lower rate i.e. totally 15 kg/year. The test was run for 10^{10} seconds or about 320 years. Figure 4-12 shows the void ratio and the pore water distributions at the end of the calculation. The pore water pressure is similar to the corresponding calculation with Drucker-Prager yielding the highest remaining suction in the bentonite of about 340 kPa.

Unlike the corresponding calculation with the Drucker-Prager model this calculation ran until the end without lost contact. Figure 4-13 shows the eroded volume as a function of time from start of the erosion.

For this case there was no cavity formed in spite of that 2 400 kg (or totally 4 800 kg) dry weight of bentonite was lost.

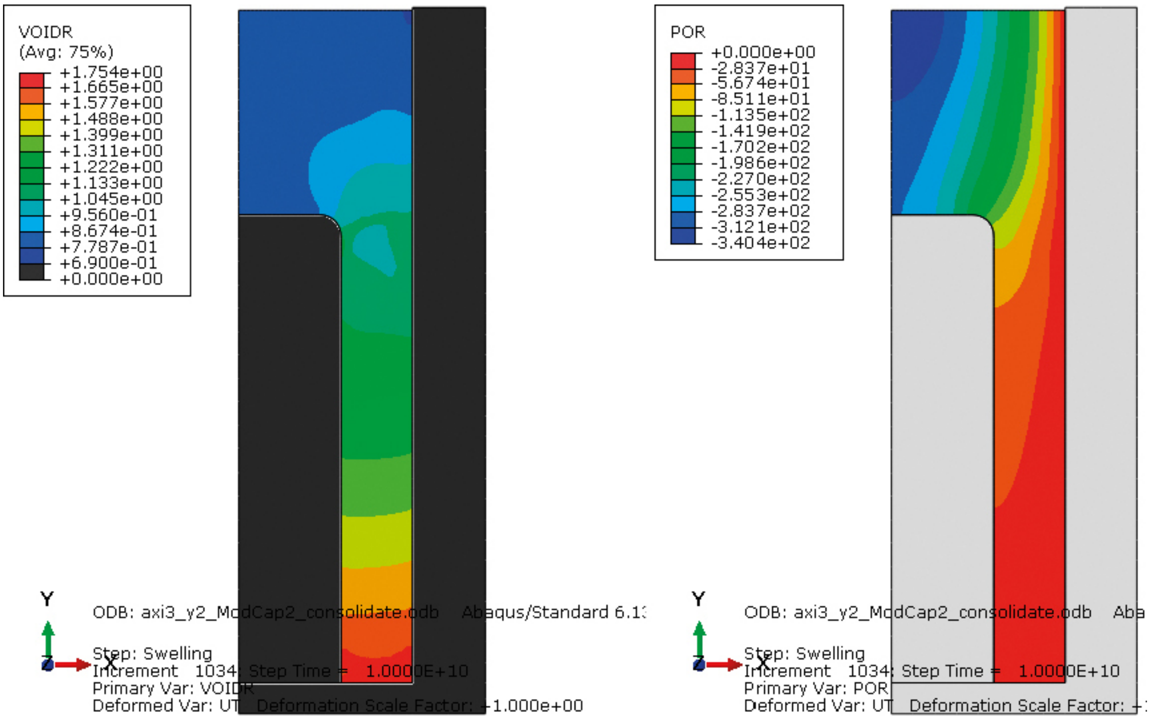

Figure 4-12. Void ratio distribution (left) and pore water pressure (kPa) after 320 years at the erosion rate 15 kg/year for the Claytech Plastic Cap model.

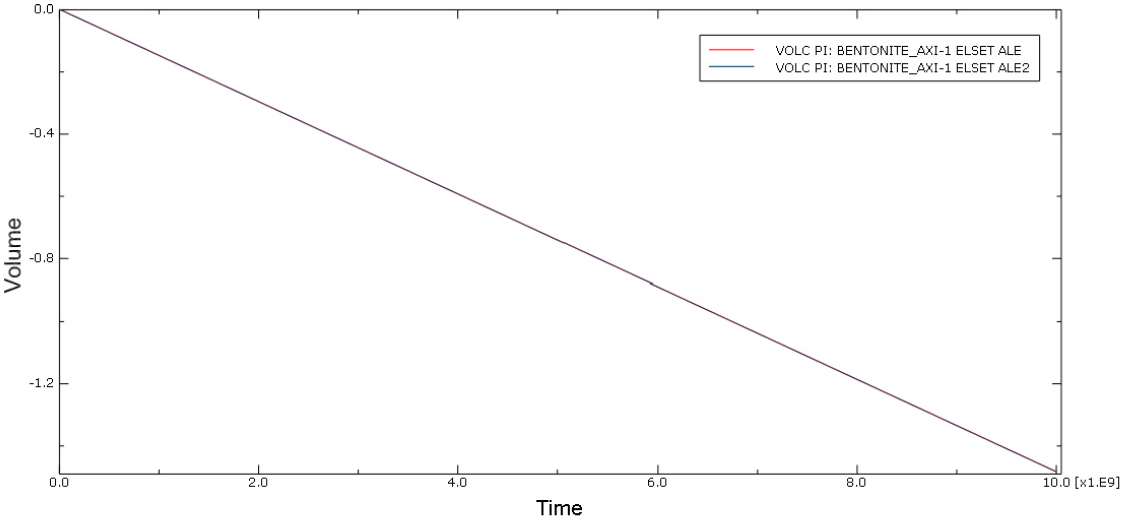

Figure 4-13. Half the eroded volume of buffer at its original density as a function of time (s) from start of the erosion. Claytech Plastic Cap model.

Figure 4-14 shows the plastic strain in the bentonite at the end of the calculation. Very high plastic strains (>30 %) occur up to about 1 m from the erosion front and around the corner of the lid of the canister.

4.3.4 Conclusions

The preliminary calculations done and reported in this chapter showed that

- Point erosion (corresponding to line erosion and subsequent expanding half donut, since axial symmetric models were used) could not be modelled due to convergence problems
- Line erosion (corresponding to erosion along a horizontal surface) according to Figure 4-6 could successfully be modelled until the contact at the erosion front was lost (and thus a cavity was formed)

The conclusions thus led to that the model shown in Figure 4-6 was used for the actual erosion calculations. As shown later this model yields pessimistic results.

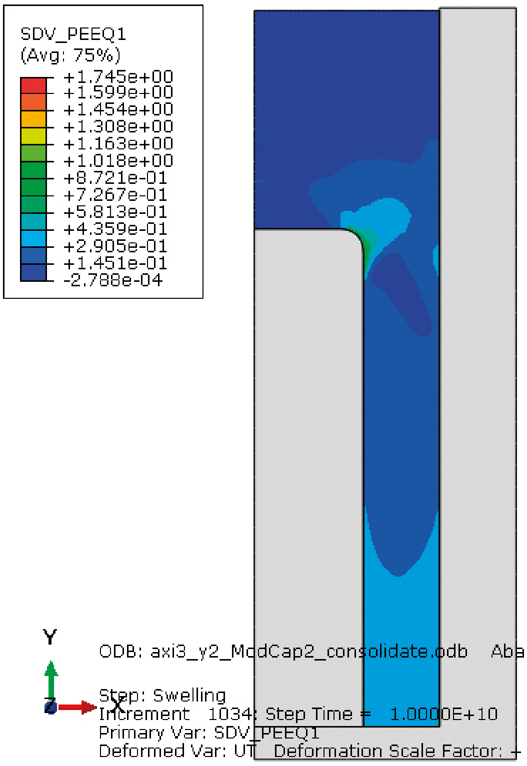

Figure 4-14. Plastic strain in the bentonite at the end of the calculation.

5 Final calculations of the erosion homogenization

5.1 General

The expected erosion rates differ substantially from the ones used in the test calculations shown in Section 4.3. Neretnieks et al. (2017) have modelled the erosion rate and the results are shown in Figure 5-1.

According to Figure 5-1 the erosion rates are a function of the NaCl concentration and the water flow rate in the fracture. Between the flow rates 5×10^{-8} m/s and 1.0×10^{-4} m/s the loss rate is between 5 g/year and 150 g/year. The loss rates 10 g/year and 150 g/year will be modelled.

Due to the convergence problems that made the calculations stop very early when point erosion was modelled, the line erosion tested in Section 4.3 were used for the modelling.

5.2 Models

The same material models, boundary conditions and initial conditions were used as shown in Chapter 3. The element mesh is similar to the one shown in Figure 4-6, which is also shown in Figure 5-2.

Variations of the element mesh with denser element mesh have also been tested but without any different results.

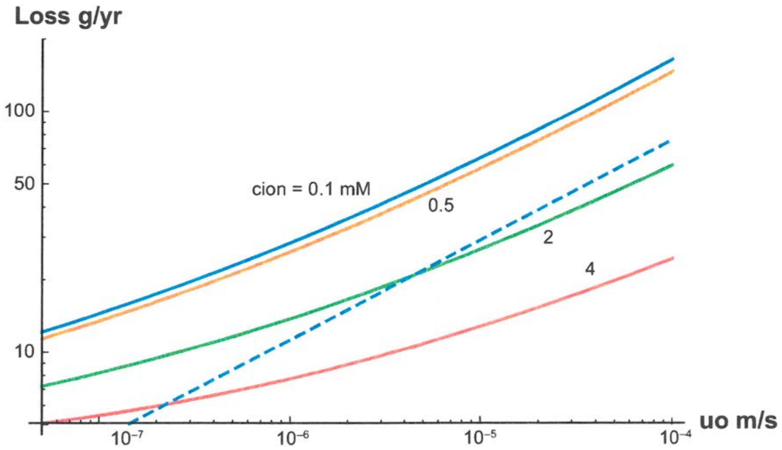

Figure 5-1. *Loss rate as function of water velocity for different ion concentrations in mM for a 0.1 mm aperture fracture. Dashed line shows the old model results from Neretnieks et al. (2009).*

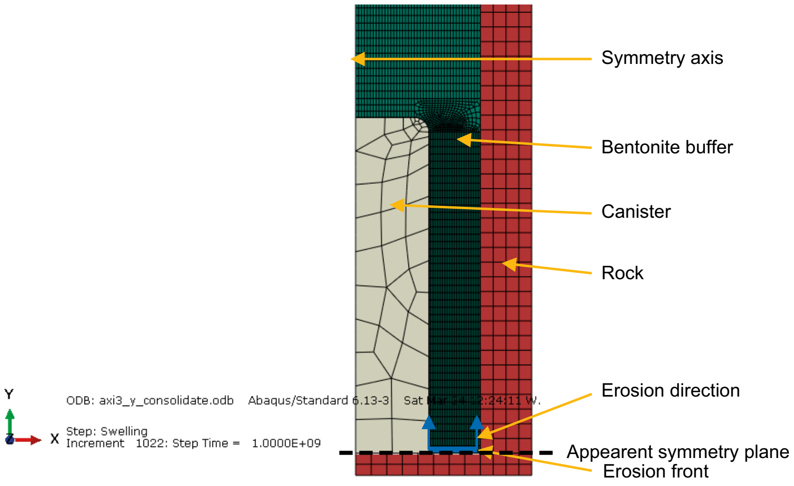

Figure 5-2. *Geometry of the element mesh with a horizontal erosion front in the "symmetry plane".*

5.3 Calculations

Two main cases have been modelled with both material models. They are summarized in Table 5-1. In addition a number of cases have been modelled in order to study the influence of the hydraulic boundary condition, the friction between the rock surface and the bentonite, and the density of the buffer.

Table 5-1. Performed calculations.

Material model	Erosion rate / model		Erosion rate / model	
Drucker-Prager	10 g/year	y4_DP	150 g/year	y3_DP
Claytech Plastic Cap	10 g/year	y4_ModCap	150 g/year	y3_ModCap

All calculations could be run until the contact between the symmetry plane and the buffer was lost, which corresponds to a time close to when a cavity is formed. However, the expansion of the cavity could not be modelled for these cases in spite of several different attempts to solve the problems. In fact, the reason seems to be a problem in the process formulation in the Abaqus code.

5.4 Results

5.4.1 Erosion rate 150 g/year

Both material models were tested for this erosion rate. The erosion rate 150 g/year corresponds to a loss of 15 000 kg dry clay in 100 000 years, which in turn means that about 6 m axially of the bentonite in the deposition hole would be lost. Figure 5-3 illustrates the erosion model. Since the erosion takes place from a symmetry plane the vertical "gap" in the figure is half of the total "gap".

The rate of loss dry mass is given as the rate of how the erosion moves upwards simulating that all material is lost (but without losing the contact since the swelling takes place simultaneously) is for this case $dz/dt = 0.95 \times 10^{-12}$ m/s. This rate is used in the calculation since the average dry density of the bentonite between the canister and the rock is $\rho_d = 1\,635$ kg/m^3 and the eroded volume in axial direction of the deposition hole V is (calculated from $\rho_d = 1\,635$ kg/m^3)

$$V = z\pi(1.75^2 - 1.05^2)/4 = 1.539z \text{ m}^3$$

where z is the vertical erosion calculated as there was no swelling as shown in Figure 5-3, which yields the dry mass $m_s = V \cdot \rho_d = 2\,517z$ kg.

150 g/year yields thus $z = 0.15/2\,517 = 5.96 \times 10^{-5}$ m/y or 1.89×10^{-12} m/s, which corresponds to 0.95×10^{-12} m/s in each direction due to the symmetry plane.

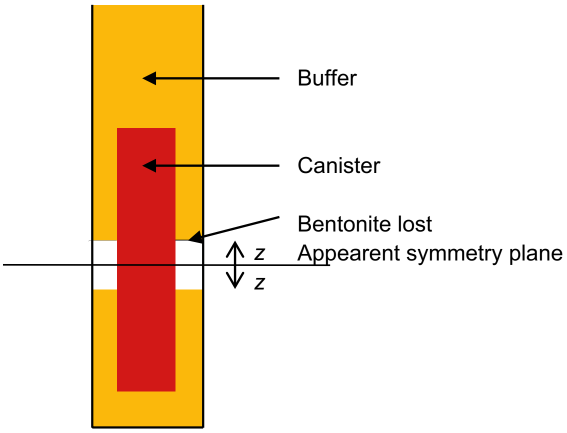

Figure 5-3. *Illustration of how the bentonite is lost.*

Drucker-Prager plasticity model (axi3_y3_DP)

The Drucker-Prager model ran to about 34 000 years when it stopped due to lost contact between the bentonite and the symmetry plane. This corresponds to L = 2.03 m, which in turn corresponds to a loss of bentonite of 5 100 kg when the cavity starts to be formed.

The modelled eroded volume is plotted in Figure 5-4 as function of time.

The void ratio distribution and the pore water pressure distribution at the end of the calculation are shown in Figure 5-5.

The dry density distribution at the end of the calculation is shown in Figure 5-6. The void ratio distribution at different times is plotted in Figure 5-7.

The calculation with the Drucker-Prager model thus shows that the swelling is so fast for about 34 000 years that the homogenization hinders a cavity to be formed but after that time the void ratio is so high that according to the model the contact is lost. This takes place at the void ratio about *e* = 1.6 at the interface.

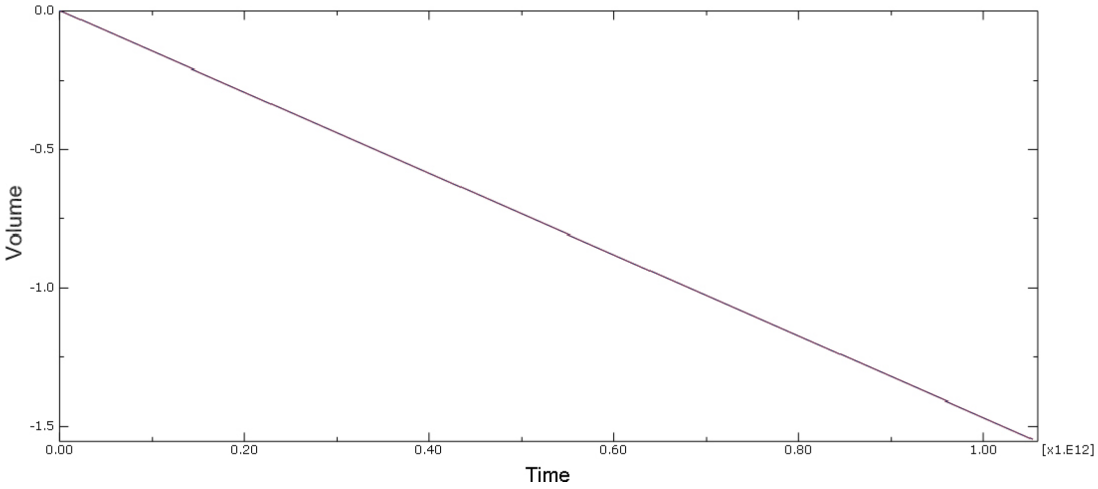

Figure 5-4. *Half the eroded volume of buffer at its original density (m^3) as function of time (s) for the DP calculation with the erosion rate 150 g/year.*

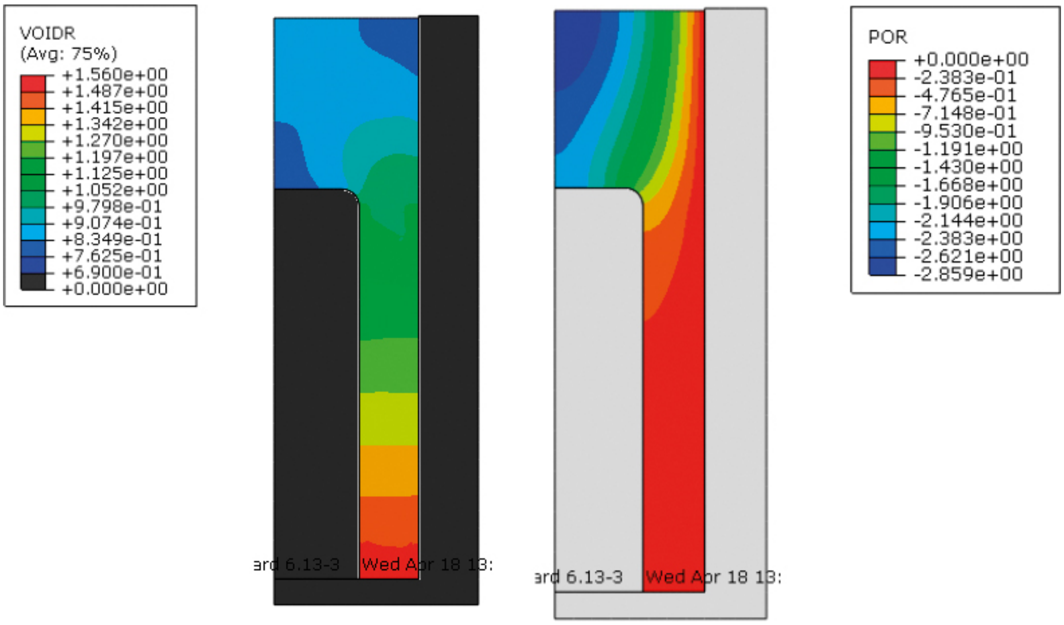

Figure 5-5. *Void ratio distribution (left) and pore water pressure (kPa) close to when the cavity is formed after 30 000 years for the DP calculation with the erosion rate 150 g/year.*

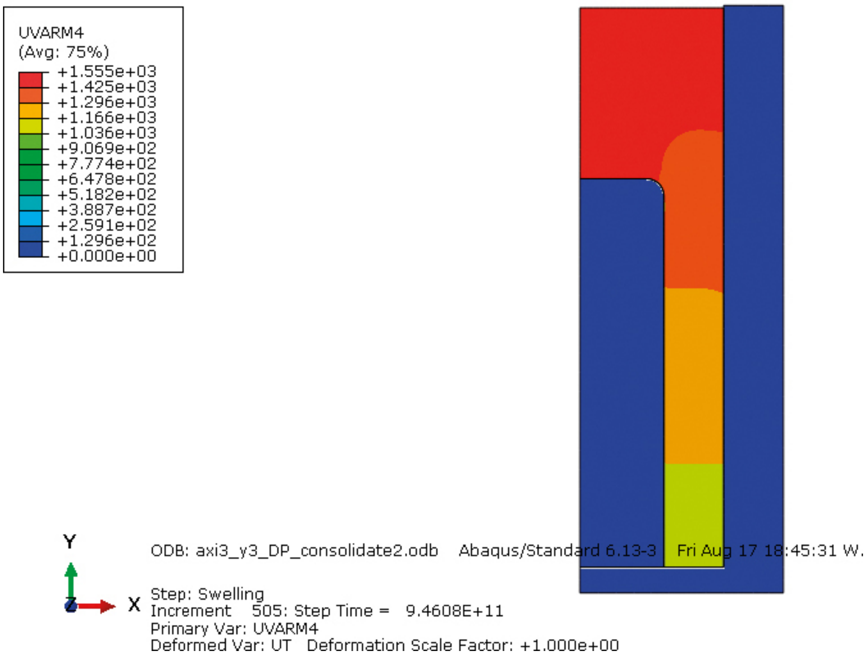

Figure 5-6. *Dry density distribution (kg/m³) after 30 000 years for the DP calculation with the erosion rate 150 g/year close to when the cavity is formed.*

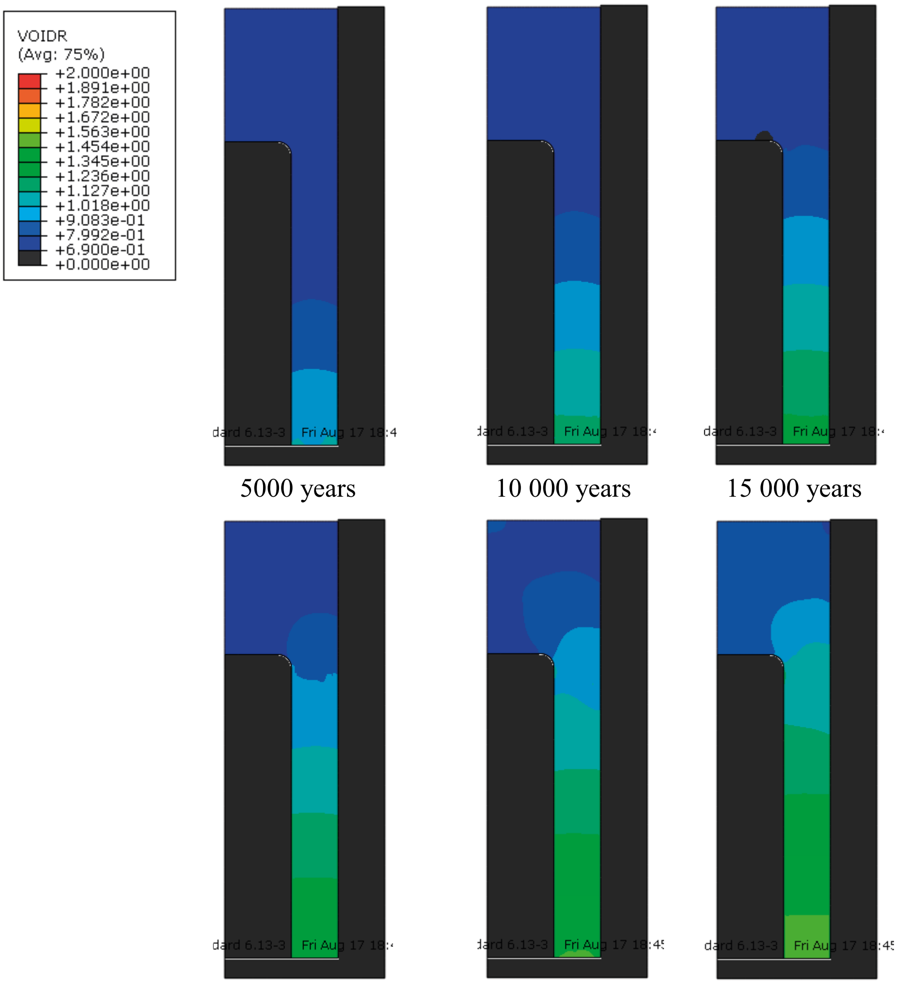

5000 years 10 000 years 15 000 years

20 000 years 25 000 years 30 000 years

Figure 5-7. *Evolution of the void ratio distribution plotted in the same scale.*

Claytech Plastic Cap model (axi3_y3_ModCap)

The Plastic Cap model ran to about 50 000 years when it stopped due to lost contact between the bentonite and the symmetry plane. This corresponds to a total loss of bentonite of 3.03 m, which in turn corresponds to a loss of bentonite of 7 620 kg when the cavity starts to be formed.

The volume eroded is plotted in Figure 5-8 as function of time.

The void ratio distribution and the pore water pressure distribution at the end of the calculation are shown in Figure 5-9.

The dry density distribution at the end of the calculation is shown in Figure 5-10. The void ratio distribution at different times is plotted in Figure 5-11.

The calculation with the Plastic Cap model thus shows that the swelling is so fast for about 50 000 years that the homogenization hinders a cavity to be formed but then the void ratio is so high that according to the model the contact is lost. This takes place at the void ratio about $e = 2.5$ at the interface.

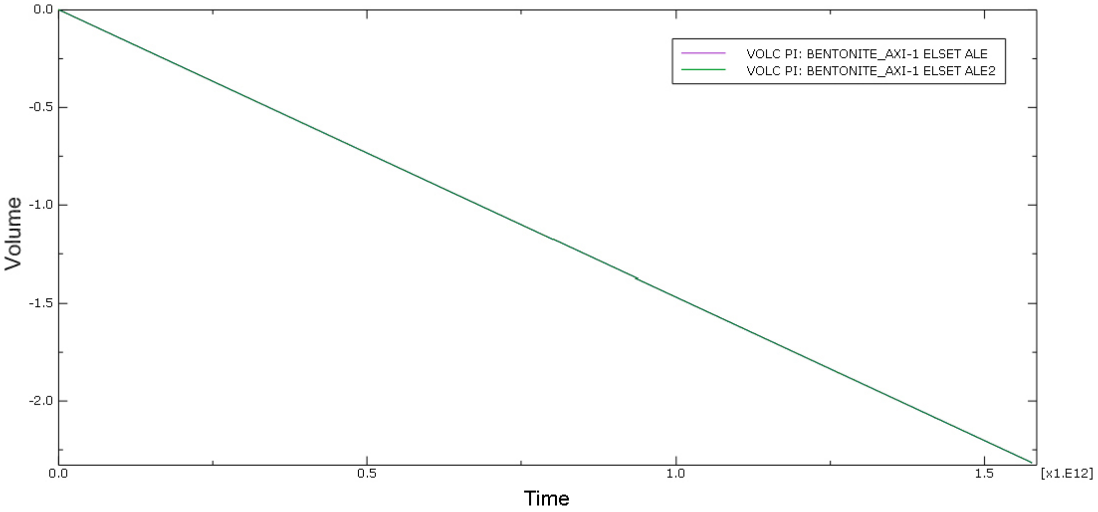

Figure 5-8. *Eroded volume of buffer at its original density (m^3) as function of time (s) for the Plastic Cap calculation with the erosion rate 150 g/year.*

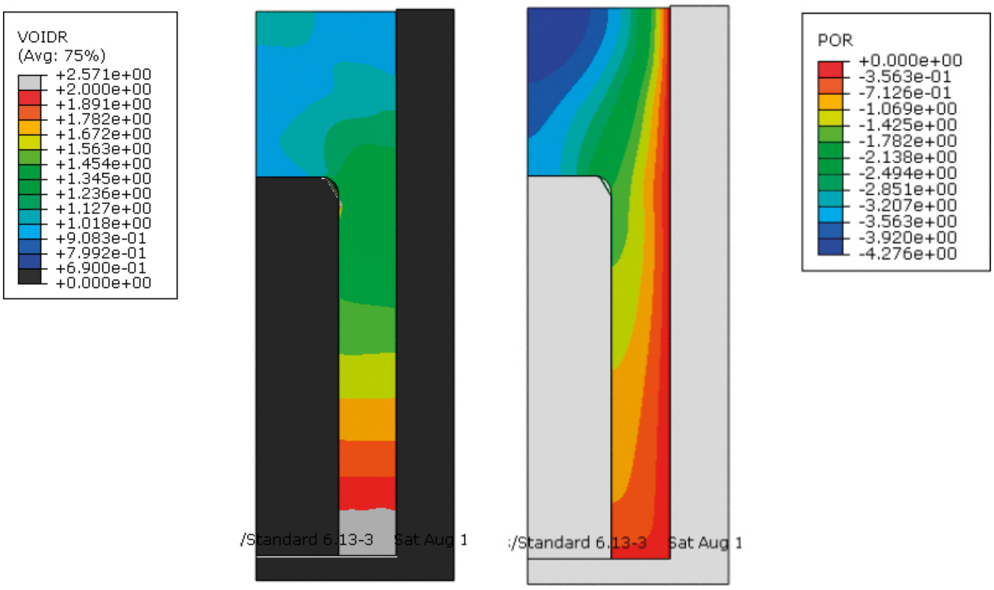

Figure 5-9. *Void ratio distribution (left) and pore water pressure (kPa) for the Plastic Cap calculation with the erosion rate 150 g/year when the cavity is formed after 50 000 years.*

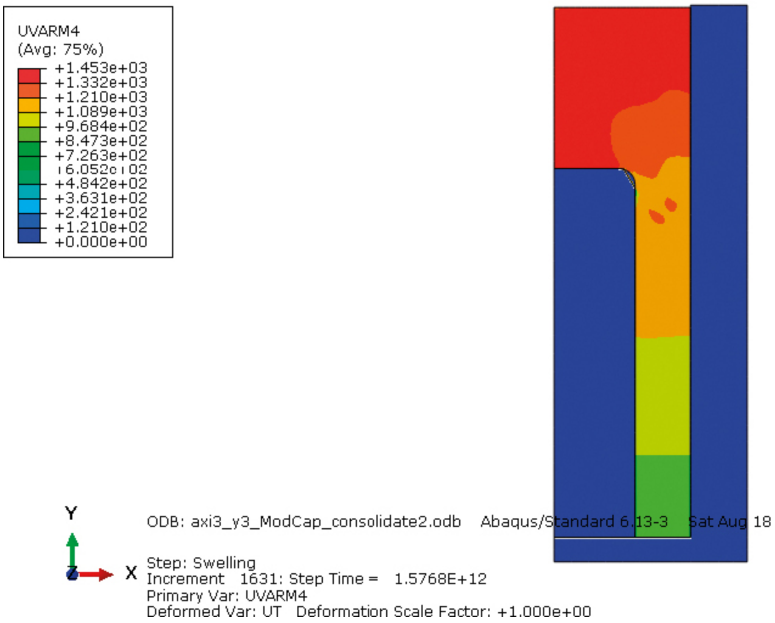

***Figure 5-10.** Dry density distribution (kg/m³) for the Plastic Cap calculation with the erosion rate 150 g/year when the cavity is formed after 50 000 years.*

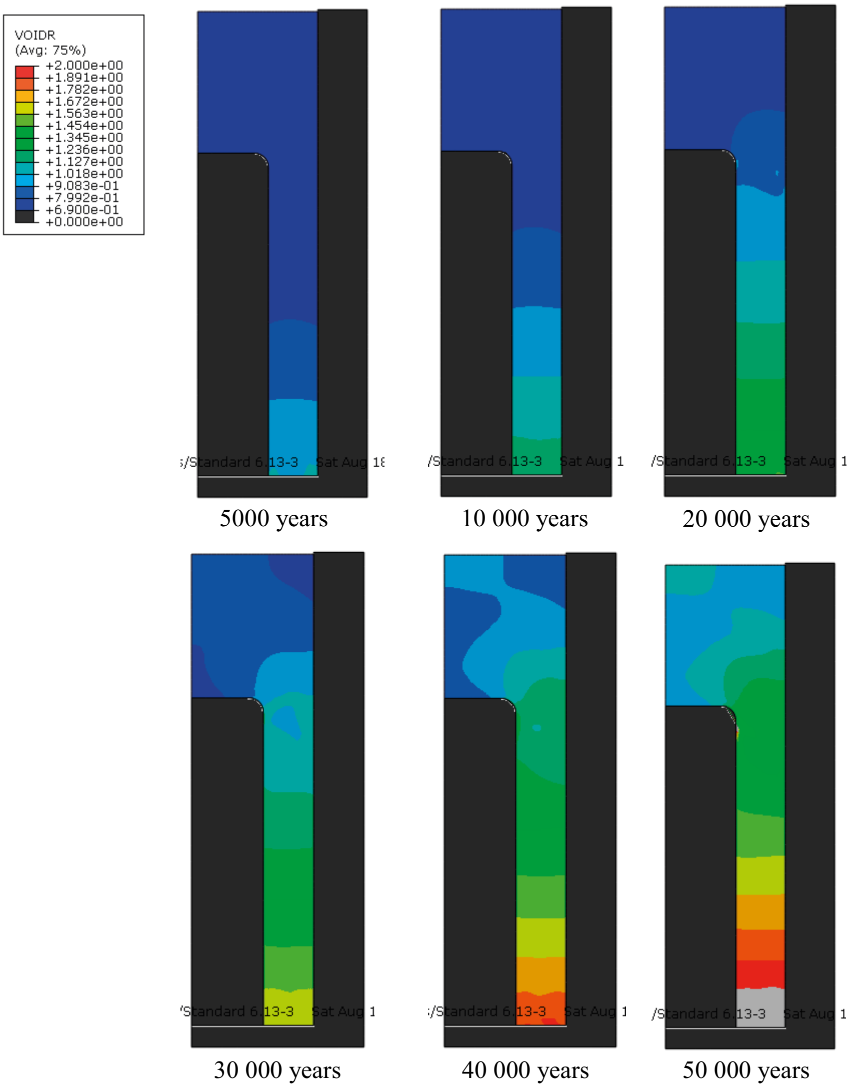

5000 years

10 000 years

20 000 years

30 000 years

40 000 years

50 000 years

***Figure 5-11.** Evolution of the void ratio distribution plotted in the same scale.*

The difference in time for the two calculations depends mainly on the void ratio difference when the contact is lost and to some extent also on the material model (but these are of course coupled). The void ratio after 30 000 years at the interface is for the Plastic Cap model $e = 1.6$, which can be compared to $e = 1.6$ for the DP model.

It can also be noted that the pore pressure gradient that drives the swelling is very low in the buffer. It is only about 4 kPa along the entire deposition hole.

5.4.2 Erosion rate 10 g/year

Both material models were used for this erosion rate. The erosion rate 10 g/year corresponds to a loss of 1 000 kg dry clay in 100 000 years, which in turn means that about 0.40 m axially of the bentonite in the deposition hole is lost. Since the erosion takes place from a symmetry plane the vertical “gap” in the figure is half of that ($z = 0.2$ m). See also Figure 5-3.

The rate of loss given as the rate of how the erosion moves upwards (but without losing the contact since the swelling takes place simultaneously) is for this case $dz/dt = 6.40 \times 10^{-14}$ m/s. This rate is used in the calculation.

Drucker-Prager plasticity model (y4_DP)

The Drucker-Prager model ran to about 515 000 years when it stopped due to lost contact between the bentonite and the symmetry plane. This corresponds to $z = 1.04$ m or a total loss of bentonite at the initial density of 2.08 m, which in turn corresponds to a total loss of bentonite of 5 230 kg when the cavity starts to be formed.

The void ratio distribution and the pore water pressure distribution at the end of the calculation are shown in Figure 5-12.

The dry density distribution at the end of the calculation is shown in Figure 5-13. The void ratio distribution at different times is plotted in Figure 5-14.

The calculation with the Drucker-Prager model thus shows that the swelling is so fast for 515 000 years that the homogenization hinders a cavity to be formed but after that the contact is lost. This takes place at the void ratio about $e = 1.6$ at the interface.

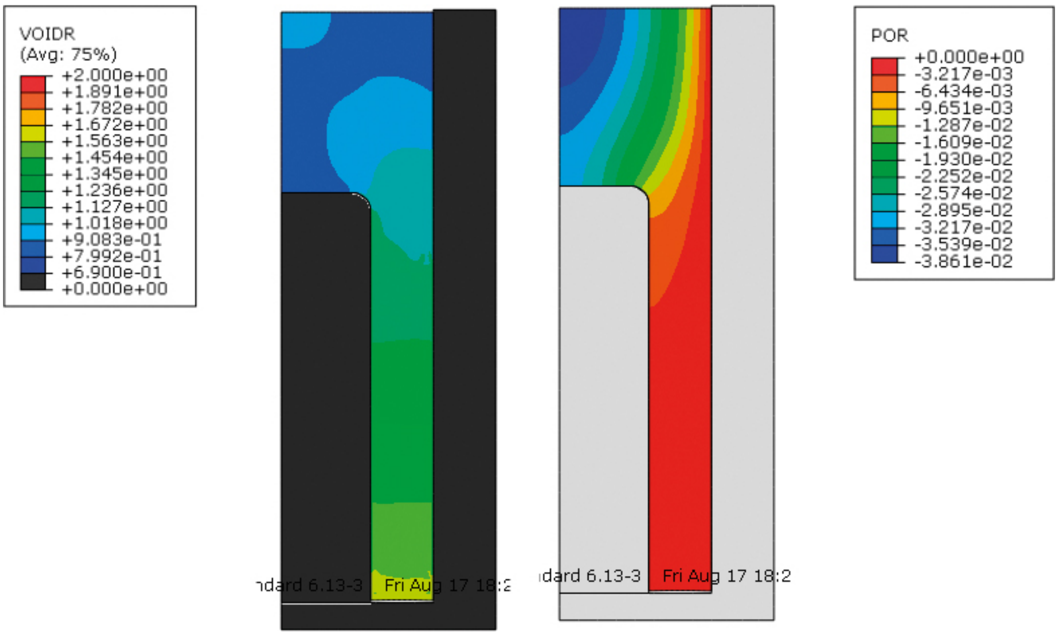

Figure 5-12. *Void ratio distribution (left) and pore water pressure (kPa) for the DP calculation with the erosion rate 10 g/year when the cavity is formed after 515 000 years.*

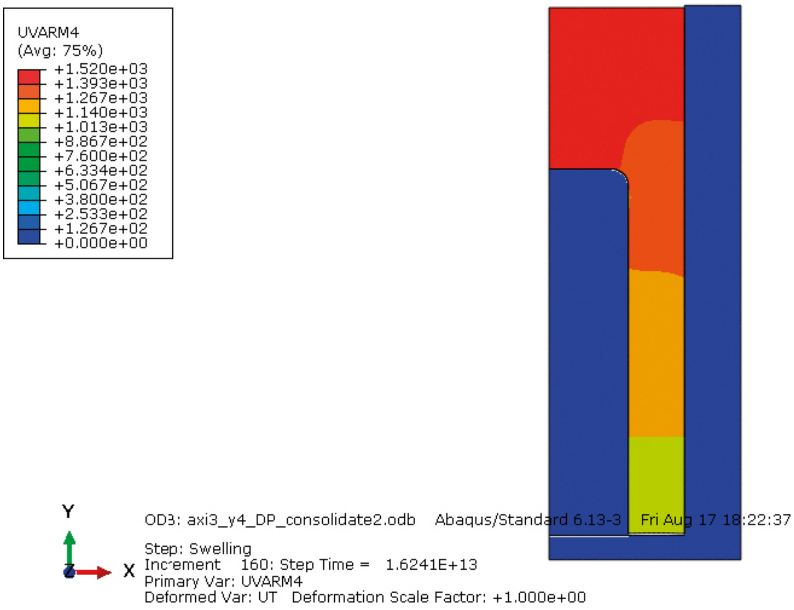

Figure 5-13. *Dry density distribution (kg/m^3) for the DP calculation with the erosion rate 10 g/year when the cavity is formed after 515 000 years.*

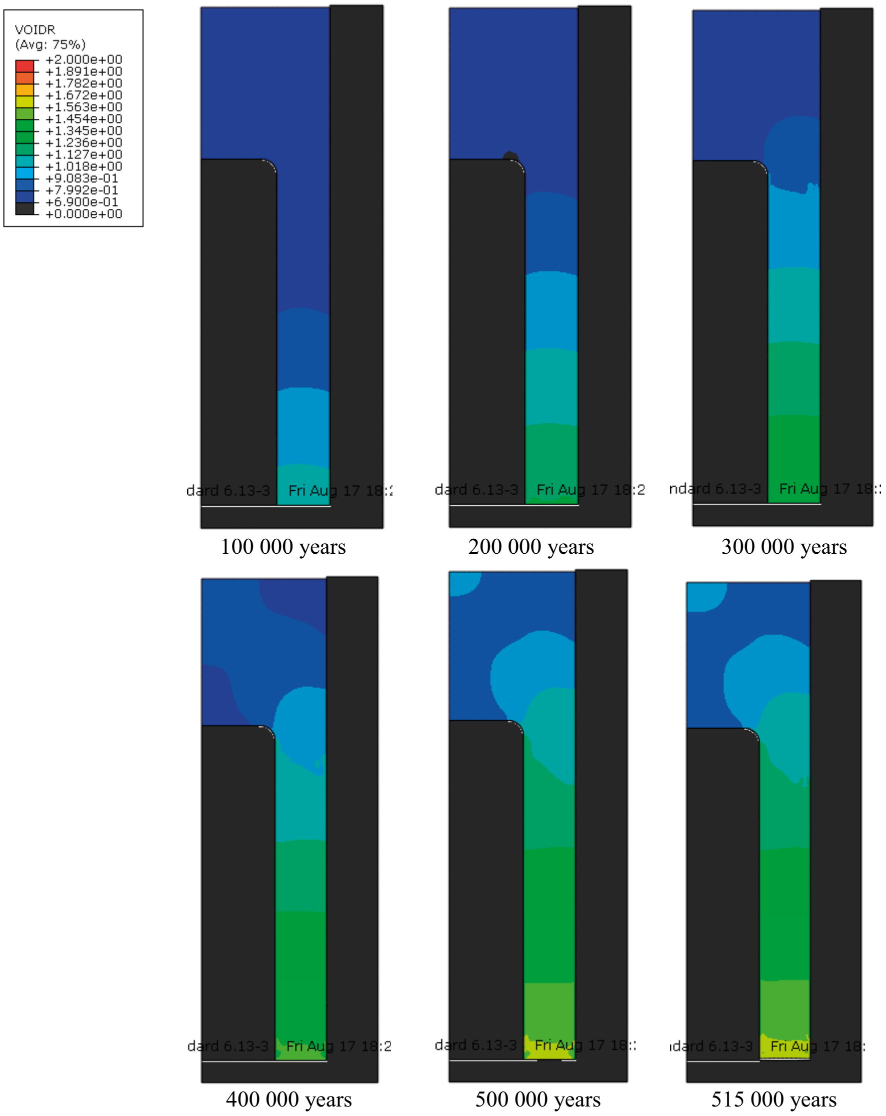

100 000 years 200 000 years 300 000 years

400 000 years 500 000 years 515 000 years

Figure 5-14. *Evolution of the void ratio distribution plotted in the same scale.*

Claytech Plastic Cap model (y4_ModCap)

The Plastic Cap model ran to about 610 000 years when it stopped due to lost contact between the bentonite and the symmetry plane. This corresponds to $z = 1.23$ m or a total loss of bentonite of 2.46 m at the initial density, which in turn corresponds to a total loss of bentonite of 6 200 kg when the cavity starts to be formed.

The void ratio distribution and the pore water pressure distribution at the end of the calculation are shown in Figure 5-15.

The dry density distribution at the end of the calculation is shown in Figure 5-16. The void ratio distribution at different times are plotted in Figure 5-17.

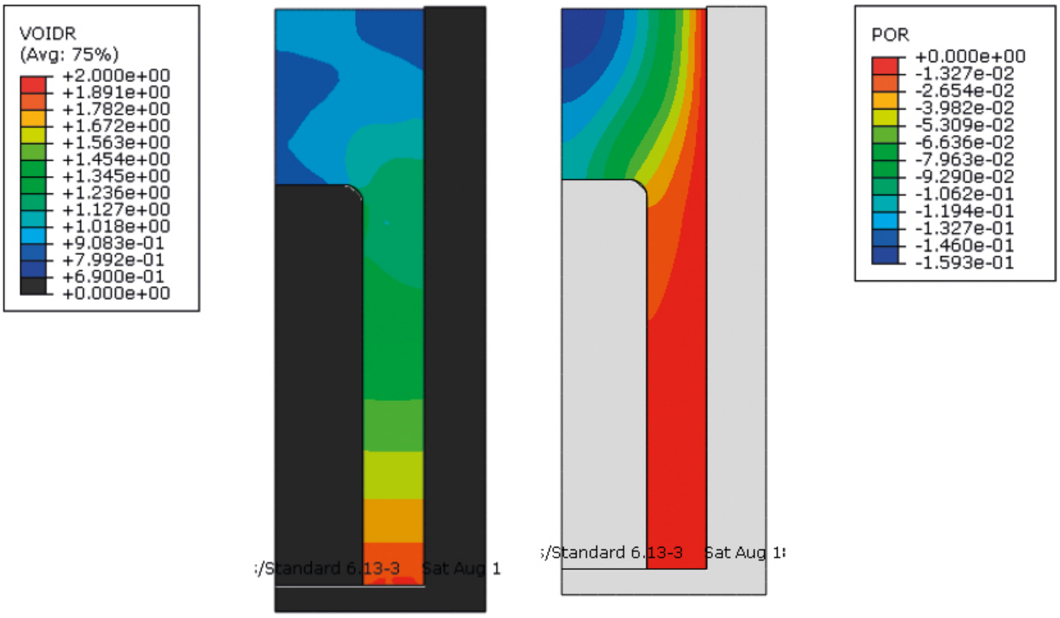

***Figure 5-15.** Void ratio distribution (left) and pore water pressure (kPa) for the Plastic Cap calculation with the erosion rate 10 g/year when the cavity is formed after 610 000 years.*

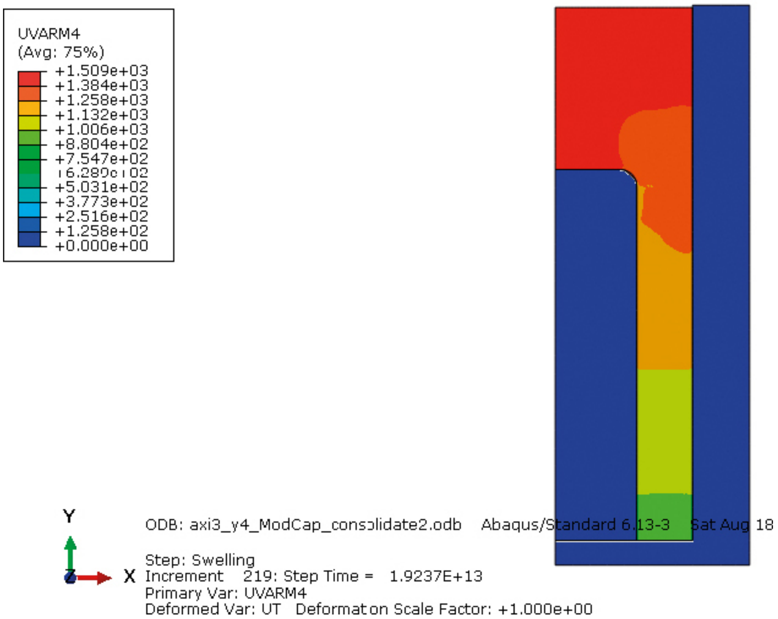

***Figure 5-16.** Dry density distribution (kg/m^3) for the Plastic Cap calculation with the erosion rate 10 g/year when the cavity is formed after 610 000 years.*

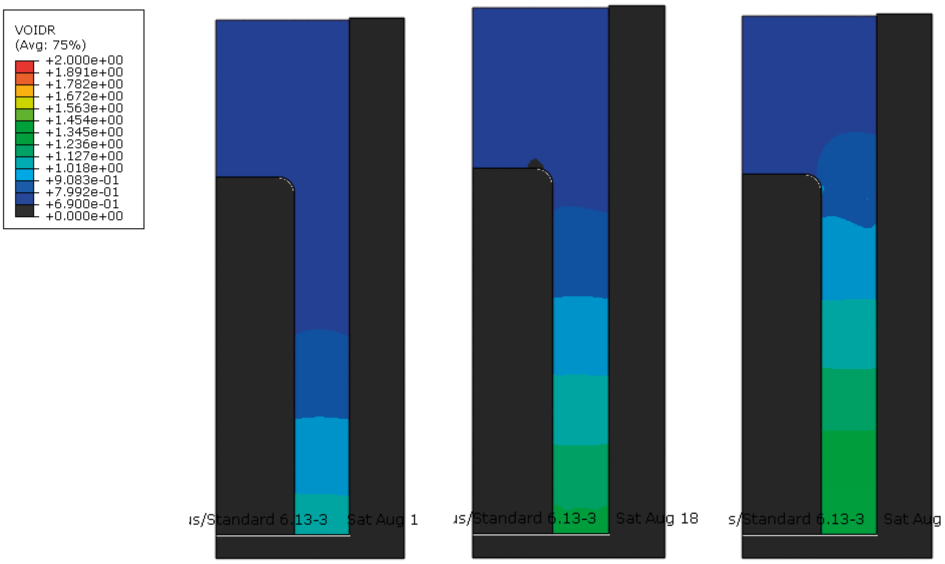

100 000 years 200 000 years 300 000 years

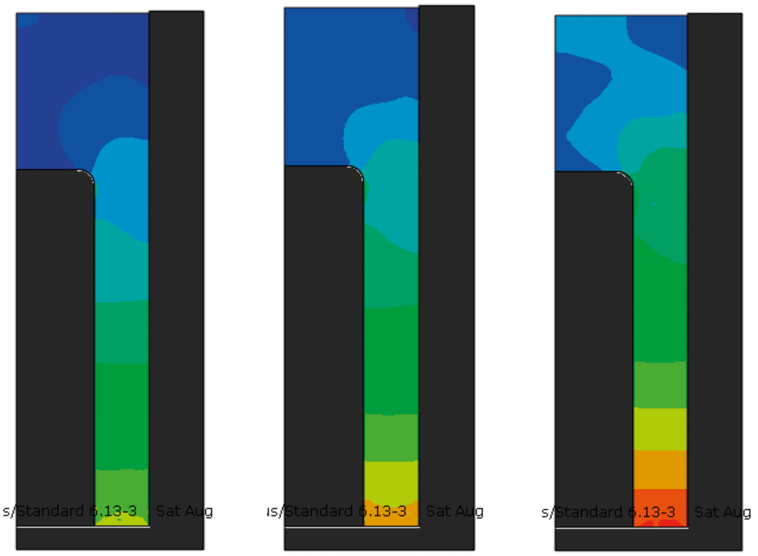

400 000 years 500 000 years 610 000 years

Figure 5-17. *Evolution of the void ratio distribution plotted in the same scale.*

The calculation with the Plastic Cap model thus shows that the swelling is so fast for 610 000 years that the homogenization hinders a cavity to be formed but then the contact is lost. This takes place at the void ratio about $e = 1.9$ at the interface.

5.4.3 Water available only along the rock surface

The models described stem from hydraulic boundary conditions with water freely available not only from the rock surface but also from the erosion front. This is the case after lost contact but not before. In order to investigate the influence of this condition the same calculations have been performed but with no water available at the erosion front.

The results show that there is an influence in the beginning of the erosion but after some time the influence disappears and at the end when the contact is lost the influence is negligible.

Figure 5-18 shows the pore water pressure after 10 000 years at the erosion rate 150 g/year with the Plastic Cap model. The hydraulic gradient is very low but the figure clearly shows the difference in boundary conditions at the erosion front. Figure 5-19 shows comparison of the void ratio distribution after 30 000 years. Practically no difference of results between the calculations can be seen after that time.

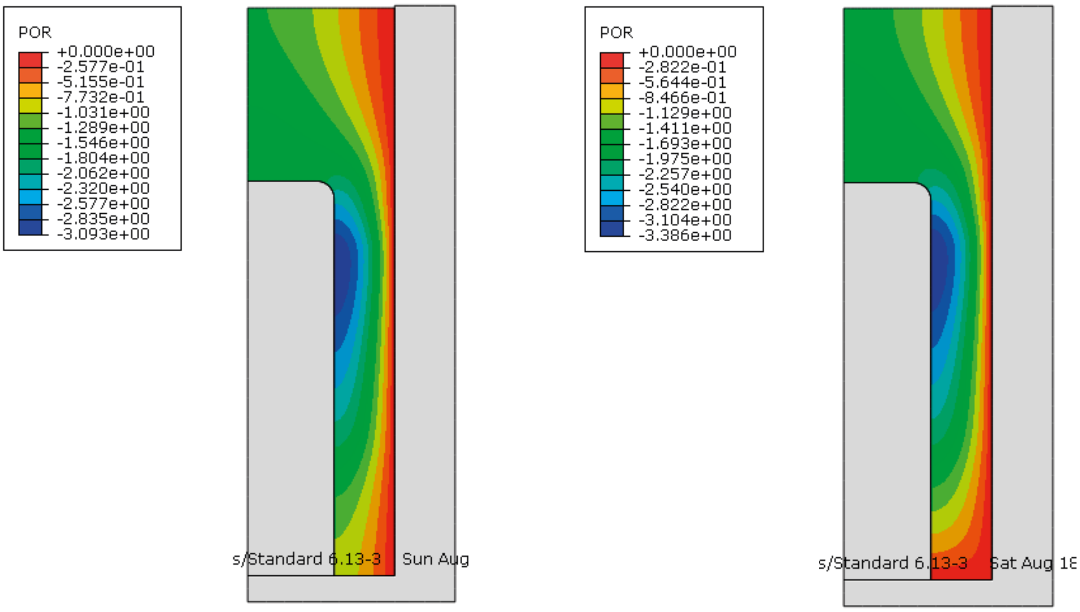

No water at the erosion front

Water at the erosion front

***Figure 5-18.** Comparison of the calculations with and without water available at the erosion front. The pore water pressure (kPa) after 10 000 years at the erosion rate 150 g/year. The Plastic Cap model.*

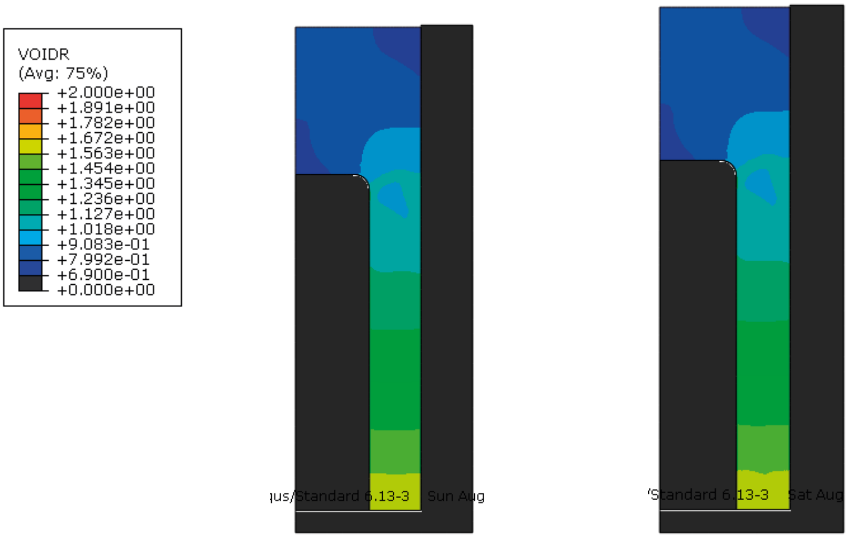

No water at the erosion front

Water at the erosion front

***Figure 5-19.** Comparison of the calculations with and without water available at the erosion front. The void ratio after 30 000 years at the erosion rate 150 g/year. The Plastic Cap model.*

All other calculations with the alternative hydraulic boundary condition have the same behavior, so the conclusion is that the hydraulic boundary condition at the erosion front does not influence the results.

5.4.4 Influence of the friction angle

The friction angle between the rock surface and the bentonite and between the canister and the bentonite was set to 7.2 degrees based on the findings by Dueck et al. (2019). See also Section 3.4. However, the friction angle is a function of the mean effective stress (or the void ratio) and increases with decreasing stress and increasing void ratio. In order to study the influence of the friction angle on the homogenization during erosion, a sensitivity study was performed by repeating the calculations with three different friction angles.

Since there were convergence problems a slight change in the element mesh was done compared to the mesh shown in Figure 4-6 but otherwise identical input data was used for the calculations. The erosion rate 150 g/y was modelled.

The following friction angles were used in these calculations:

$\phi = 5.71°$ (*axi6e*)
$\phi = 7.2°$ (*axi6*)
$\phi = 8.53°$ (*axi6d*)

The calculations were not run until complete loss of contact so the results are illustrated by a comparison between the void ratio distribution after 40 000 years in Figure 5-20. The Plastic Cap Model was used for these calculations.

Figure 5-20 shows that the void ratio gradient is stronger for high friction angles than for low. This is logical since the bentonite is more "hanging" on the walls by the higher resistance to sliding for a higher friction angle. The logical result should be longer time to lost contact and thus also more lost bentonite before appearance of the cavity but the models did not run that far.

However, the Drucker-Prager models were run to complete loss of contact. Figure 5-21 shows the void ratio distribution at the time when the contact just was lost.

Figure 5-21 shows that the time to lost contact is longer for lower friction angles. It also shows that the void ratio at the contact surface is about the same when the contact is lost (about $e = 1.6$) and that the void ratio gradient is stronger for the higher friction angles.

These calculations thus show that the friction angle between the rock surface and the bentonite has a rather strong influence on the time to when the contact is lost and thus also the amount of lost bentonite.

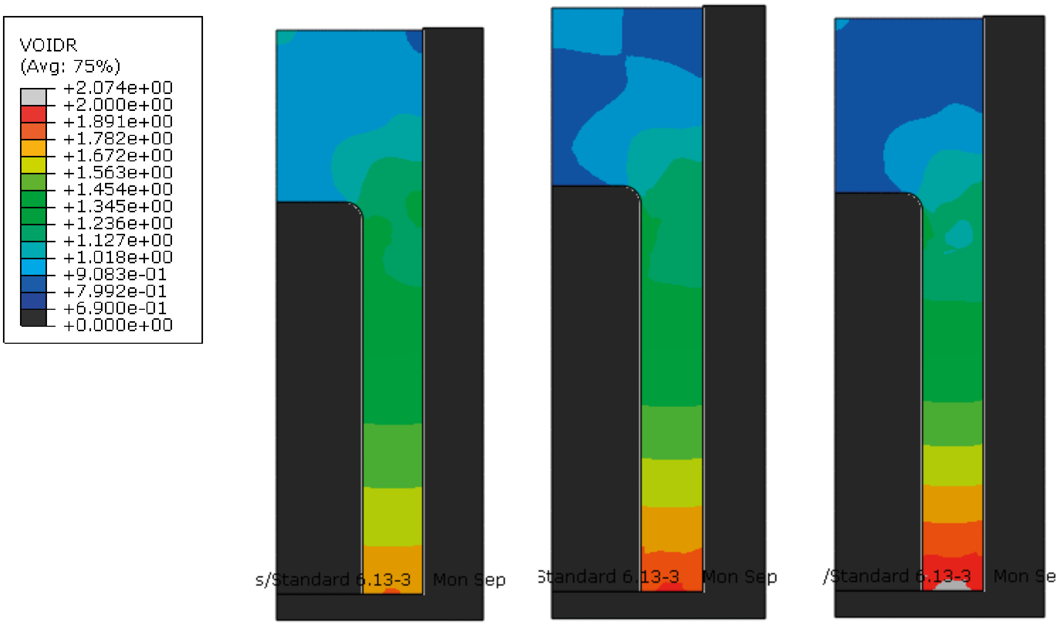

ϕ=5.71° (*axi6e*) ϕ=7.2° (*axi6*) ϕ=8.53° (*axi6d*)

Figure 5-20. *Modelled void ratio distribution after 40 000 years for different friction angles at the erosion rate 150 g/y. The Plastic Cap model.*

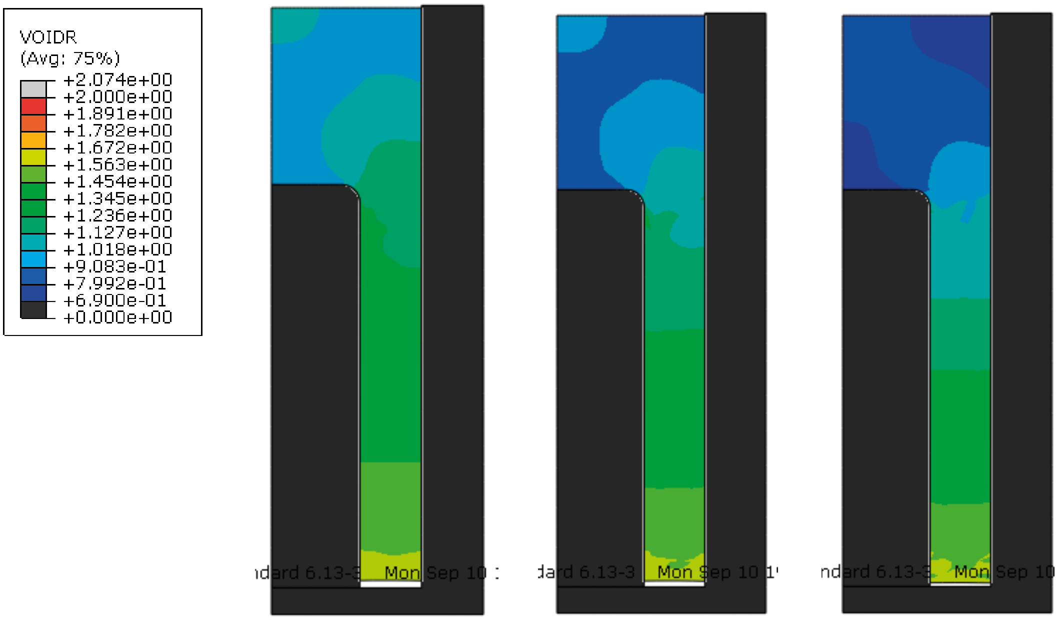

ϕ=5.71° (*axi6e*)
40 000 years

ϕ=7.2° (*axi6*)
35 000 years

ϕ=8.53° (*axi6d*)
30 000 years

Figure 5-21. *Modelled void ratio distribution after lost contact for different friction angles at the erosion rate 150 g/y. The Drucker-Prager model.*

5.4.5 Influence of buffer density

A rather high buffer density was used for the calculations. One can expect faster loss of contact if the buffer density is lower since the void ratio limit should be reached earlier. In order to see if there is any difference new calculations were done with the initial void ratio $e=0.77$ ($\rho_d=1\,571$ kg/m^3, $\rho_m=2\,006$ kg/m^3) instead of $e=0.70$ ($\rho_d=1\,635$ kg/m^3, $\rho_m=2\,047$ kg/m^3).

The same rate of loss of bentonite $dz/dt=0.95\times10^{-12}$ m/s was used. This caused a slightly lower erosion rate $dm_s/dt=144$ kg/year (compared to 150 kg/year) due to the lower density.

The Plastic Cap model was used for the calculations. Similar time to lost contact was reached in the calculation with lower density as in the calculation with the original high density (in fact slightly longer time for the low density calculation). Figure 5-22 shows a comparison between the void ratio distribution just before lost contact after 45 000 years.

Figure 5-22 shows that the void ratio logically is lower for the calculation with the initially higher void ratio of the buffer, but also that there is still contact at the erosion front and thus no cavity formed.

The conclusion is that the influence of the initial density of the buffer is small within the acceptable ranges of buffer density.

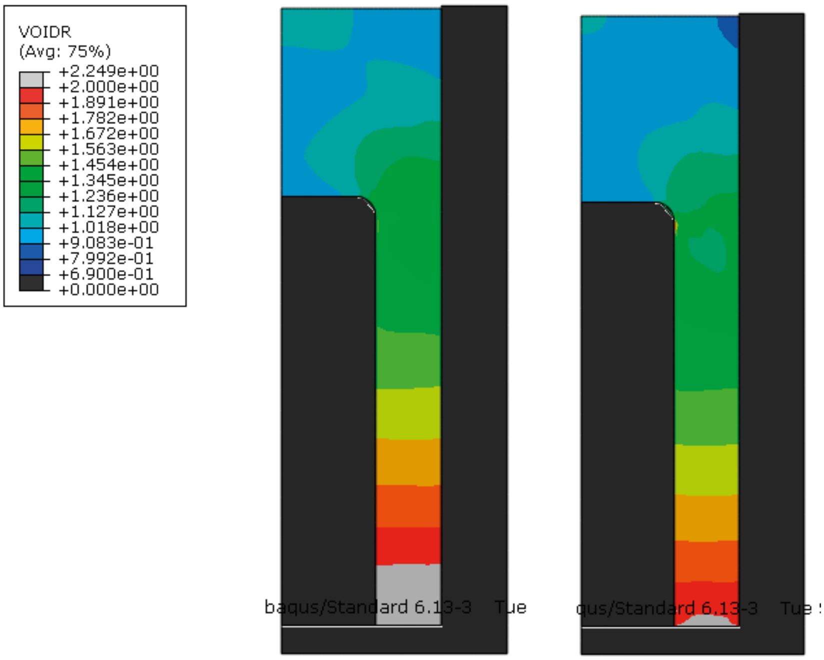

e=0.77 *e*=0.70

Figure 5-22. *Comparison of the void ratio distribution just before lost contact after 45 000 years for two slightly different initial void ratios.*

5.5 Comments to and evaluation of the results

The erosion rates considered are 10 g/year and 150 g/year caused by colloid erosion, which are derived by Neretnieks et al. (2017). The void ratio distribution at the end of the calculations is very similar for the two different erosion rates for both material models in the basic calculations. For both erosion rates the Plastic Clay model yields longer time until the contact is lost than the DP model. The time until contact is lost is for the Plastic Clay model about 12 times longer at the slow erosion rate than at the fast one and for the DP model 15 times longer. This shows that the time to contact loss is approximately proportional to the erosion rate. The difference for the Plastic Cap model is caused by the higher void ratio reached at the fast erosion rate.

The difference between the results from the two material models is as mentioned above mainly caused by the difference in void ratio at the contact surface. Table 5-2 shows a comparison between some results.

The void ratios at contact loss are not very high especially in the DP calculations and should for non-saline conditions yield a swelling pressure of about between 80 kPa and 180 kPa. The contact is in spite of this lost, which is caused partly by the material model, which is more relevant for saline conditions, and partly by the uneven stresses in the elements in contact with the symmetry plane, which can make the contact stress zero in spite of a rather high mean stress in the element. So, the time until lost contact is probably underestimated. Looser clay should be able to fill the void before the contact is lost.

Table 5-2. Comparison between some results of the calculations.

	Erosion rate 10 g/year		**Erosion rate 150 g/year**	
	DP model	**Plastic Cap model**	**DP model**	**Plastic Cap model**
Time to contact loss (y)	515 000	610 000	34 000	50 000
Void ratio at contact surface	1.6	1.9	1.6	2.5
Loss of material (kg)	5 230	6 200	5 100	7 620
Loss length in axial dir. (m)	2.08	2.46	2.03	3.03

Table 5-2 shows thus that the total loss in bentonite when the contact is lost and when there is a direct open space between the rock surface and the canister corresponds to 2–3 m bentonite rings, which in turn corresponds to 4–6 bentonite rings with the thickness 0.5 m. This is 2–3 times more than used in the safety analysis (Åkesson et al. 2010a, SKB 2010).

The initial test calculations of the erosion procedure with much faster erosion (100–1 000 times faster) resulted in less material lost before formation of a cavity (2 800–4 800 kg). These results also showed a much higher void ratio gradient in the buffer and a much higher remaining negative pore water pressure close to lost contact, which indicates that the erosion goes faster than the swelling. This explains why the contact is lost earlier. There is too little mass of bentonite to swell and keep the gap closed, but if the erosion was interrupted swelling would most probably continue and close the gap.

It is difficult to estimate the influence of having a line erosion instead of a point erosion (or actually erosion at a 0.1 mm aperture). For the same erosion rate the point erosion will yield much higher erosion rate per area in the beginning so it is probable that the cavity will be formed much earlier in that case. However, a circular cavity means that the erosion will take place along that surface instead of along a straight line surface. Figure 5-23 illustrates the difference.

At constant erosion rate in g/year the material loss per area is a direct function of the total area in contact with the bentonite that is available for erosion. The surface will move when the swelling rate is lower than the erosion rate. This means that the radius *r* of the erosion front quarter circle at point erosion will move until the erosion rate per area is lower than the swelling rate. This also means that we can conclude that when the contact surface area of the half donut from point erosion is equal to the surface area of the line erosion, the swelling will be equally fast and the half donut will not expand earlier than when the contact area at the line erosion is lost. This is not entirely true since there is a difference in geometry that to some extent will influence the swelling. In addition, the swelling will most likely be faster in axial direction of the deposition hole than in radial direction, since there is much more bentonite available axially than radially so the geometry of the cavity will look more like the geometry shown in Figure 5-24.

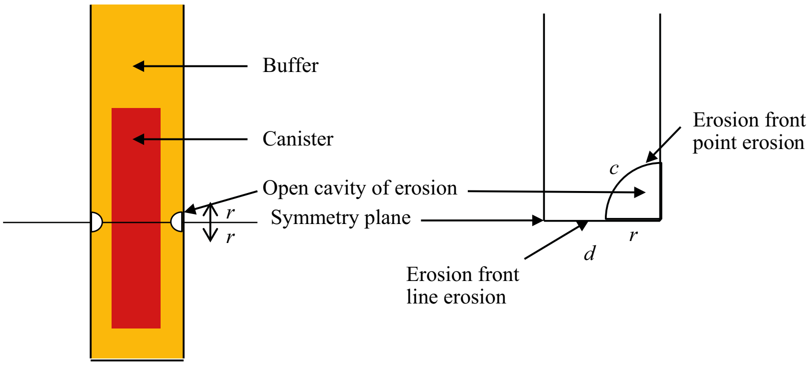

Figure 5-23. *Illustration of the difference between line erosion and point erosion. d is the length of the erosion front at line erosion, r is the radius of the quarter circle and c is the length of the erosion front at point erosion leading to a circular cross section.*

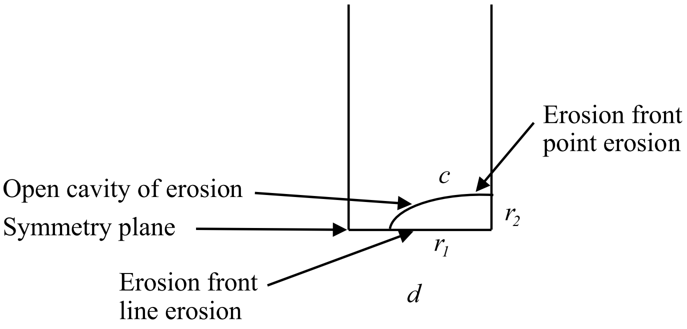

Figure 5-24. *Expected shape of cavity at point erosion*

c is always larger than r_1, so c will be larger than d when r_1 gets close to d, i.e. when the cavity will get close to reaching the canister. This means that the erosion rate per area will be lower than from line erosion and the time until the cavity at point erosion hits the canister is expected to be longer than the time until the contact at line erosion is lost.

Since the model assumes a symmetry plane at the centre of the canister the late swelling from below may be slightly less than from above.

As noted in the description of the material model Porous Elastic (Section 3.2.1) this model is not valid for void ratios larger than 1.5 for MX-80 at non-saline conditions. The swelling to higher void ratios yields higher swelling pressure than modelled by this model. The model is more relevant for Ca-bentonite and Na-bentonite at high salinity. Since the colloid erosion takes place under very low ion concentrations the swelling and homogenization at low densities will be underestimated by this model and thus also the time to when the contact is lost.

The conclusion is thus that there will not be any open cavity in contact with the canister until a time that is longer than derived according to the line erosion calculations shown in Table 11-2. The loss of dry bentonite at that time is larger than 5 tons corresponding to more than 4 bentonite rings.

6 Conclusions

The possibility to model colloid erosion from a fracture intersecting a deposition hole with constant mass loss of the bentonite buffer has been investigated. The erosion has been modelled with a new Abaqus user defined routine and the swelling has been modelled with material models derived for bentonite homogenization. As common in multiphysics problems with complex geometries, the convergence was problematic and simplifications of the geometry had to be done. The erosion has been assumed to take place in a horizontal fracture intersecting the entire rim of deposition hole in the centre of the canister. The investigation has led to the following results and conclusions:

- The mass loss can be well modelled with the Abaqus erosion subroutine that prescribes a constant displacement rate of the erosion front. However, after lost contact at the erosion front there were convergence problems that stopped the calculations.
- The erosion process can be coupled to the swelling and homogenization processes modelled with the Porous Elastic and Drucker-Prager Plasticity models as well as the Claytech Plastic Cap model.
- The geometry of the erosion front had to be "simplified" in order to get any results since point erosion, corresponding to line erosion in the axial symmetric model, could not be modelled.
- A way to model the erosion with applying a small half donut on the rock surface in the deposition hole and use that donut surface as erosion front was tested. The erosion and subsequent homogenization were possible to model to a limited extent of erosion that corresponded to about 100 kg bentonite lost. Then it was not possible to continue the calculation due to convergence problems (probably due to buckling caused by high radial pressure for the innermost elements).
- The simplified assumption by applying the erosion front in a horizontal symmetry plane along the fracture through the buffer was at first tested with a very high erosion rate. Although the erosion rates and duration times were unrealistic a total erosion of 3 360–4 800 kg was modelled, but these cases are not fully comparable due to the high pore pressure gradients that do not occur at realistic erosion rates.
- At those unrealistically high erosion rates (15–150 kg/year) the cavity was formed earlier, i.e. after less loss of material than at lower erosion rates, since the swelling was not fast enough in order to keep track with the mass loss.
- The final calculations were done with a line erosion front stretching horizontally from the fracture to the canister corresponding to a surface erosion in the axial symmetric geometry. Both material models were used and the studied variation in erosion rate of 10–150 g/year was modelled. The calculations resulted in a total mass loss of between 5.1 and 7.6 tons dry bentonite before the contact between in the erosion front was lost depending on the material model and the erosion rate. This corresponds to 4–6 bentonite rings with the thickness 0.5 m.
- At the expected erosion rates the time until contact loss is about inverse proportional to the erosion rate and the eroded mass at formation of a cavity thus independent of the erosion rate, since the swelling is fast enough to keep track with the mass loss.
- The time to lost contact and thus formation of a cavity was 34 000–50 000 years at the erosion rate 150 g/year and 515 000–610 000 years at the erosion rate 10 g/year. The Plastic Cap model yielded the longest time due to a higher reached void ratio at the lost contact.
- The void ratio at lost contact was rather low (1.6–2.5) due to the material model and the stress situation in the element at the erosion front. Since these void ratios correspond to a swelling pressure between about 80 kPa and 180 kPa it is most probable that the void ratio would be higher and time to lost contact longer and thus that the eroded mass of bentonite is underestimated at lost contact.
- In addition, the simplified geometry of a line erosion instead of a point erosion is expected to underestimate the time to when the cavity comes in contact with the canister and thus also the eroded mass.

- The influence of changing the hydraulic boundary condition at the erosion front to no flow boundary was found to be insignificant except for in the very beginning of the calculation.
- The influence of the friction angle between the rock surface and the bentonite was found to be rather significant. An increase in friction angle from 5.7° to 8.5° decreased the time and thus also the amount of bentonite lost until a cavity was formed with about 25 %.
- The influence of the initial density of the buffer was found to be rather insignificant for the acceptable ranges of buffer density.
- There are of course several uncertainties like for all modelling results, like the material model. However, most uncertainties, like the geometry of the erosion front and the limited swelling capacity included in the material model, are judged to yield pessimistic results.

The overall conclusion is that there will not be any open cavity stretching from the fracture to the canister until the dry bentonite mass lost is larger than 5 tons and that this figure most probable is an underestimation.

Appendix A

Storage of files

This report is based on the results of many FE simulations using ABAQUS, which is a commercially available code and is thus not stored as part of the work (ABAQUS 2017). Below is a short description of the files used in the project and the directories for their storage. These files are also stored at SKB.

The files are stored in the following directories:

Geometry
InputFiles
Plots
Scripts
Subroutines

A1 Input files used for the simulations

Each analysis is initiated by abaqus job=input-file (w/o .inp).

Contents of C:\Users\jhd\mappar\clay\erosion\InputFiles

axi3_y_consolidate.inp	vertical erosion with rate 70 kg/year using DruckerPrager
axi3_y2_consolidate.inp	vertical erosion with rate 7 kg/year using DruckerPrager
axi3_y2_ModCap2_consolidate.inp	vertical erosion with rate 7 g/year using Modified Cap
axi3_y3_DP_consolidate2.inp	final vertical erosion with rate 150 g/year using DruckerPrager
axi3_y3_DP2_consolidate2.inp	final vertical erosion with rate 150 g/year using DruckerPrager and initial void ratio equal to 0.77
axi3_y3_ModCap_consolidate2.inp	final vertical erosion with rate 150 g/year using Modified Cap
axi3_y3_ModCap2_consolidate2.inp	final vertical erosion with rate 150 g/year using Modified Cap and initial void ratio equal to 0.77
axi3_y4_DP_consolidate2.inp	final vertical erosion with rate 10 g/year using DruckerPrager
axi3_y4_ModCap_consolidate2.inp	final vertical erosion with rate 10 g/year using Modified Cap
axi7_consolidate2.inp	toroidal erosion
axi7_erode2.inp	toroidal erosion without homogenization
axi6d_y3_DP_consolidate2.inp	friction sensitivity (0.15)
axi6d_y3_ModCap_consolidate2.inp	friction sensitivity (0.15)
axi6e_y3_DP_consolidate2.inp	friction sensitivity (0.10)
axi6e_y3_ModCap_consolidate2.inp	friction sensitivity (0.10)
axi6_y3_DP_consolidate2.inp	friction sensitivity (0.126329)
axi6_y3_ModCap_consolidate2.inp	friction sensitivity (0.126329)

A2 Scripts used for post-processing

These scripts are used inside ABAQUS/CAE or by “abaqus cae startup=script.py” after the appropriate editing of the job name inside the script file.

Contents of C:\Users\jhd\mappar\clay\erosion\Scripts

ModCap.py	generate plots for axi3 and axi6

A3 Geometry definitions

Contents of C:\Users\jhd\mappar\clay\erosion\Geometry

exa.cae	ABAQUS/CAE-database
exa.jnl	ABAQUS/CAE journal file

A4 Subroutines

Contents of C:\Users\jhd\mappar\clay\erosion\Subroutines

axi_y_erode.f	user defined subroutine with erosion rate 70 kg/year
axi_y2_erode.f	user defined subroutine with erosion rate 7 kg/year
axi_y3_erode.f	user defined subroutine with erosion rate 150 g/year
axi_y4_erode.f	user defined subroutine with erosion rate 10 g/year
axi7_erode.f	user defined subroutine with erosion rate 7 kg/year
axi7b_erode.f	user defined subroutine with erosion rate 70 kg/year

Part 2

Formation and growth of cavities in buffer due to erosion

Mattias Åkesson, Svensk Kärnbränslehantering AB

Abstract

The aim of this task was to investigate the potential formation and growth of cavities in the buffer due to bentonite erosion. Of special interest was the question whether a hypothetical cavity which exhibits a semi-circular shape and which precisely exposes the canister surface is realistic or not.

The approach for this task was to develop hydromechanical numerical models, implemented in the MathCad software, for simulating the loss of bentonite from the buffer and the resulting homogenization, and to assess the conditions and governing processes for the formation of cavities in the buffer for a constant erosion rate. The motive for developing such models was that the available finite element tools, with relevant hydromechanical models implemented, do not usually facilitate the prescription of the loss of solids. The new numerical models included several novel features: i) a prescribed mass loss at one of the boundaries; ii) the discretization of the geometry in elements with constant dimension until the formation of a cavity; iii) the representation of wall friction between the bentonite and lateral surfaces; and iv) introduction of a critical void ratio which defines how far the bentonite can swell until a cavity is formed. The used material model was the Hysteresis Based Material model (HBM) with a parameter setting adopted for MX-80 bentonite.

The numerical models were developed for two different one-dimensional geometries, with axial and radial swelling, respectively. These models were used to calculate the time until cavity formation and the corresponding total mass loss for cases with assumed erosion rates and frictions angles. The total mass loss required to reach cavity formation with the base case axial swelling model was approximately 5 tons, while the corresponding mass loss for the radial swelling model was 1.2 tons.

Finally, simplified solutions derived from analytical void ratio profiles based on the stress equilibrium relations and the HBM model were found to give results which were similar to the results from the numerical models. In addition, a void ratio profile associated with axial swelling with wall friction was compared with profiles associated with radial swelling without wall friction. From this comparison, it was argued that a hypothetical cavity which exhibits a semi-circular shape which precisely exposes the canister surface is not realistic. An additional argument for this was that the forces upheld by the tangential stresses in an arch are much larger than the potential friction forces acting on the canister surface in such a condition.

Sammanfattning

Syftet med föreliggande arbete var att undersöka den eventuella uppkomsten och tillväxten av hålrum i bufferten till följd av bentoniterosion. Av särskilt intresse var frågan om huruvida ett hypotetiskt hålrum som uppvisar ett halvcirkulärt tvärsnitt och som precis exponerar kapselytan är realistiskt eller ej.

Angreppssättet för detta arbete var att utveckla hydromekaniska numeriska modeller, implementerade i MathCad, för att simulera förlusten av bentonit från bufferten och den resulterande homogeniseringen, samt att uppskatta förutsättningarna och de styrande processer för uppkomsten av hålrum i bufferten vid en konstant erosionshastighet. Motivet för att utveckla sådana modeller var att tillgängliga finita-element-verktyg, med relevanta implementerade hydromekaniska modeller, vanligtvis inte möjliggör en föreskriven massförlust. De nya numeriska modellerna inkluderade flera nya delar: i) en föreskriven massförlust vid ena randen; ii) diskretisering av geometrin i element med konstanta dimensioner fram till dess att ett hålrum bildas: iii) representation av väggfriktion mellan bentonit och sidoytor; iv) introduktion av ett kritiskt portal som definierar hur långt bentoniten kan svälla innan ett hålrum bildas. Som materialmodell användes den Hysteresbaserade materialmodellen (HBM) med en parameteruppsättning framtagen för MX-80 bentonit.

De numeriska modellerna utvecklades för två olika endimensionella geometrier; med axiell respektive radiell svällning. Dessa modeller användes för att beräkna tiden till uppkomst av hålrum och motsvarande totala massförlust för olika beräkningsfall med antagna erosionshastigheter och friktionsvinklar. Den totala massan som krävdes för att hålrum skulle bildas i basfallet med den axiella svällningsmodellen uppgick till c:a 5 ton, medan den motsvarande massförlusten med den radiella svällningsmodellen var 1.2 ton.

Förenklade lösningar som härletts från analytiska portalsprofiler, vilka baseras på spänningsjämviktsrelationer och HBM-modellen, visade sig ge resultat som liknade resultaten från de numeriska modellerna. Därtill jämfördes en portalsprofil för axiell svällning och väggfriktion med olika portalsprofiler för radiell svällning utan väggfriktion. Baserat på denna jämförelse kan ett hypotetiskt hålrum som uppvisar ett halvcirkulärt tvärsnitt och som precis exponerar kapselytan betraktas som orealistisk. Ett ytterligare argument för detta var att krafterna som upprätthålls av tangentialspänningarna i en sådan valvbåge är betydligt högre än de potentiella friktionskrafter som verkar mot kapselytan under sådana förhållanden.

7 Introduction

Background

SKB (2010) presented copper corrosion calculations for a case in which a cavity penetrating the bentonite buffer exhibits a semi-circular shape which precisely reaches the canister surface. Such a shape of the cavity was regarded to be a pessimistic and unrealistic assumption by SKB (2011). The Swedish Radiation Safety Authority (SSM) has subsequently requested a more detailed motivation for this judgement. The aim of this task was therefore to investigate the potential formation and growth of cavities due to erosion.

Approach

The approach for this task was to develop hydromechanical (HM) numerical models, implemented in the MathCad software, for simulating the loss of bentonite from the buffer and the resulting homogenization, and to assess the conditions and governing processes for the formation of cavities in the buffer for a constant erosion rate. The motive for developing such models was that the available finite element tools, with relevant HM models implemented, do not usually facilitate the prescription of the loss of solids.

The used material model is the Hysteresis Based Material model (HBM), with a parameter set adopted for MX-80, which originally was developed within the EBS Taskforce (Börgesson et al. 2020) and subsequently implemented in Comsol Multiphysics within the Homogenization project (Dueck et al. 2019). Compared to numerical models presented in the EBS TF report, the new model included several new features: i) a prescribed mass loss at one of the boundaries; ii) the discretization of the geometry in elements with constant dimension until the formation of a cavity; iii) the representation of wall friction between the bentonite and lateral surfaces; and iv) introduction of a critical void ratio which defines how far the bentonite can swell until a cavity is formed.

Numerical models were developed for two different one-dimensional geometries, with axial and radial swelling, respectively. These models were used to calculate the time until cavity formation and corresponding total mass loss for cases with assumed erosion rates and frictions angles.

In addition, simplified solutions derived from analytical void ratio profiles based on the stress equilibrium relations and the HBM model were found to give results which were similar to the results from the numerical models. These void ratio distributions were finally used to comment on the relevance of the shape of the cavities mentioned above.

Outline of report

The used models are described in Chapter 8. The results from these models are presented in Chapter 9. The shape of the cavity and the remaining uncertainties are discussed in Chapter 10. Finally, a summary and some concluding remarks are given in Chapter 11. In addition, detailed descriptions of the used material model and the different models are presented in Appendix B–D.

8 Model description

8.1 HBM model

The Hysteresis Based Material model (HBM) was defined by Börgesson et al. (2020) for water saturated conditions. This was based on a description for which a clay potential Ψ (defined as the sum of stress and suction) for a specific void ratio is assigned in an allowed interval bounded by two lines, for swelling ($\Psi_M(e) - \Psi_{\Delta/2}(e)$) and consolidation ($\Psi_M(e) + \Psi_{\Delta/2}(e)$), respectively. The swelling pressure curve and the water retention curve can thereby be viewed as two sides of the same coin.

The actual state between these lines is controlled by a path variable (f), with values between −1 and +1, i.e. $\Psi = \Psi_M(e) + f \cdot \Psi_{\Delta/2}(e)$. The path variable is in turn governed by the strain (ε) history. This is achieved by defining a set of three differential equations, each of which includes f and ε for each principal direction. These equations are also linked in order to limit the maximum difference between the f-value in different direction to the value of 1. This description can thereby capture both the hysteretic behaviour (path dependency) observed in oedometer tests and water retention measurements, and the shear strength observed in unconfined compression tests and triaxial tests.

The HBM model is described in depth in Appendix B.

8.2 Axial and radial swelling models

Two numerical methods were developed to solve one-dimensional homogenization processes (axial and radial) for a water-saturated bentonite specimen which is confined in all directions, but from which bentonite is lost at a specified rate at one of the boundaries. The specimen has also free access of water (i.e. zero suction) at this boundary and will therefore swell in this direction, but this is countered by the frictional forces acting along two of the lateral sides of the geometry. If the void ratio at the boundary reaches a critical value, then this void ratio will be kept constant. This will therefore act as a mechanical boundary condition, which in turn means that the length of the specimen will decrease.

The geometry for each numerical method was discretized as an array of n elements and with n+1 adjacent nodes. The axial model was discretized so that all elements had equal initial length. In contrast, the radial model was discretized so the ratio between the radiuses of all adjacent nodes was the same. The length of all elements (axial) and the radius of all nodes (radial) stayed constant as long as the void ratio at the mass loss boundary was below the critical value. However, as soon as this value was reached, the grid was displaced with a homogenous size reduction of each element. This either implied equal length of all elements (axial) or equal ratio between the radii of all adjacent nodes (radial).

Several quantities were used in the analyses and almost all of these were defined on the elements: centre coordinate, length, displacement, dry mass, void ratio, clay potential, suction, stresses and strains. Only the velocities for water, solids and the nodes, and the radius for the radial swelling, were defined on the nodes.

The algorithm was divided in two phases: one constant length phase, and one cavity evolution phase, during which the boundary void ratio was fixed. The initial conditions were defined so that suction was zero and stresses in all directions were equal to the clay potential for the initial void ratio. The processes were driven by differences in suction which in turn were caused by the loss of dry mass from the boundary. The simulation ended once the modelled time reached a pre-defined value.

With this framework of discretization and boundary conditions, and after assigning initial conditions to all quantities, the analysis was performed in a series of time steps quantified with a time-increment.

A sequence of operations, which were based on Darcy's law, the continuity equation, relations between strains and displacements, the stress equilibrium relation, and the constitutive relations defined by the HBM model, were successively performed during each time step.

1. Water velocities are calculated from the suction gradients. The solid velocity is given by the boundary condition.
2. Velocities of nodes (in case of cavity formation) are calculated from the velocities at the boundary element.
3. Coordinates and lengths are calculated from node velocities.
4. Solid masses and void ratios are calculated from coordinates, lengths, water and node velocities.
5. Strains and displacements are calculated from void ratios, coordinates and lengths.
6. Path variable and clay potentials are calculated from void ratios and strain increments.
7. The suction profile is integrated from the stress equilibrium relation, clay potentials and boundary condition.
8. Stresses are calculated from clay potentials and suction.

Each model resulted in profiles of the void ratio, stresses in different directions and suction. They also gave the time evolution of the length of the geometry, as well as the cumulative mass loss.

The derivation of the numerical models is described in Appendix C.

8.3 Geometries, parameter sets and model cases

The dimensions of the axial swelling model (d, B and L, see Figure 8-1) were adopted in the following way:

- The thickness (d) was calculated as half the difference between the diameter of the deposition hole and the canister $(1.750-1.052)/2 \approx 0.35$ m
- The width (B) was calculated as the circumference for the mean value of the diameter of the deposition hole and the canister $\pi(1.750+1.052)/2 \approx 4.4$ m
- The length (L) was calculated as half the buffer volume (which is approx. 15 m^3) divided with the section area $d \cdot B \approx 4.9$ m.

The dimensions of the radial swelling model (R_{in}, R_{out} and d, see Figure 8-2) were adopted in the following way:

- The thickness (d) was the same as for the axial model: 0.35 m.
- The inner radius (R_{in}) was set to a low value: 0.05 m.
- The outer radius (R_{out}) was calculated to yield the same volume as the buffer (i.e. approx. 15 m^3): 3.7 m.

Parameter values for the HM material model were identical to the values presented by Börgesson et al. (2020). These are presented in Section B.4.

The initial void ratio was set to 0.78 which is equivalent to a saturated density of 2 000 kg/m^3. The critical void ratio was set to 3. This corresponds to a swelling pressure of approx. 10 kPa for the lower bounding line in the HBM model. This value was chosen since the material model has not been used above this level before. This choice is further discussed in Section 9.2.

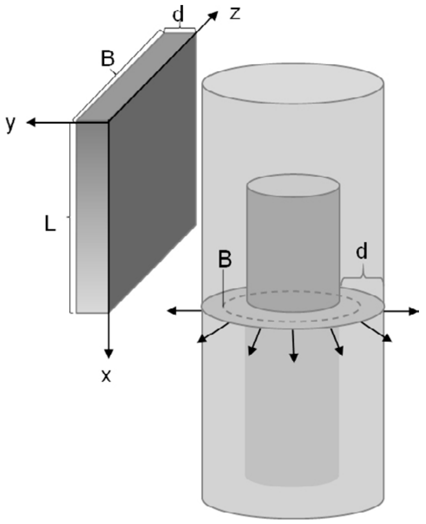

Figure 8-1. *Schematic illustration of the model geometry for axial swelling.*

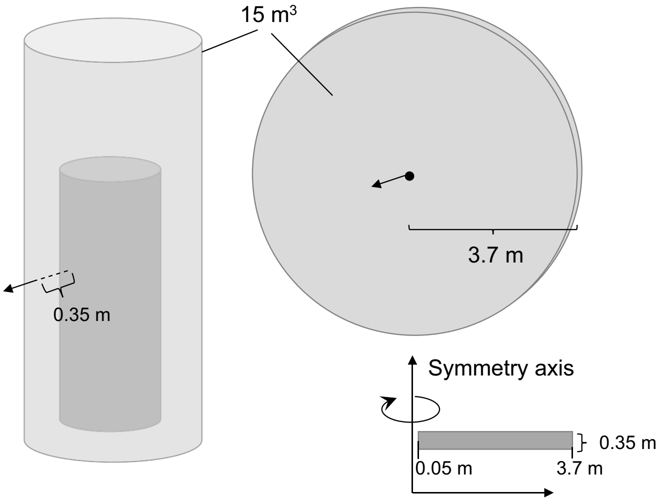

Figure 8-2. *Schematic illustration of the model geometry for radial swelling.*

A compilation of the modelled cases is given in Table 8-1.

The investigated erosion rates (150 and 10 g/yr) were chosen from the model results presented by Neretnieks et al. (2017) and were the same as those analysed in Part 1 of this report.

The base case friction angle (7.2°) was based on results from friction tests and long tube tests and was the same as the one analysed in Part 1 of this report. In order to investigate the influence of the friction angle on the time to reach the critical void ratio, model cases with half the value (i.e. 3.6°) were also analysed.

The shear stiffness associated with wall friction (K_s in Eq C-8) was set to 10 MPa/m by default. In order to investigate the influence of this parameter on the time to reach the critical void ratio, model cases with a value two orders om magnitude higher (i.e. 1 000 MPa/m) were also analysed. These cases are marked "Ks" in Table 8-1.

The geometries for the axial and the radial geometry were discretized in 15 and 12 elements, respectively. In order to check the accuracy of the numerical solution, model cases with twice as many elements were also analysed. These cases are marked "mesh" in Table 8-1.

Table 8-1. Compilation of model cases.

Friction angle	Axial swelling		Radial swelling	
	150 g/l	**10 g/l**	**150 g/l**	**10 g/l**
7.2°	A1 A1_mesh A1_mesh_Ks	A2	R1 R1_mesh	R2
3.6°	A3 A3_mesh_Ks		R3	

8.4 Simplified models based on analytical void ratio profiles

The stress equilibrium relations, which are used as fundamental conditions in the numerical solutions, can be directly used together with the constitutive relations defined by the HBM model to derive analytical expressions for stable void ratio profiles under the assumption that suction is zero throughout the geometry. In the axial case the stress gradient is countered by the shear stresses acting on the lateral sides. In the "pure" radial case without any wall friction the radial stress gradient is countered by arching effect caused by the difference between the tangential and radial stresses. Void ratio profiles can also easily be generated. A simple numerical scheme is however needed for the more general case with radial swelling together with wall friction. Such profiles were compared with results from the numerical methods (cases A1, A3, R1, R3) for the time when the critical void ratio level was reached in each case.

A more advanced utilization of these void ratio profiles is to integrate the dry density along the volume of the geometry and thereby calculating the total dry mass of the entire geometry. And by relating this mass to the initial dry mass and the rate of erosion, the time to reach a given void ratio profile can be calculated. Different dependencies were analysed in this way for both axial and radial swelling: e.g. time versus boundary void ratio and time versus friction angle. Moreover, for radial swelling the relation between time and the inner radius was analysed.

Finally, the issue of whether a hypothetical cavity which exhibits a semi-circular shape and which precisely reaches the canister surface is realistic or not was addressed. This was made through a comparison of void ratio profiles, associated with axial swelling with wall friction on one hand, and with radial swelling without wall friction, on the other.

The derivation of the analytical void ratio profiles is described in Appendix D.

9 Analysis of formation and growth of cavities

9.1 Axial and radial swelling model

Base case model behaviour and time scales

Model results for the four base cases (A1, A2, R1 and R2) are shown in Figure 9-1 to Figure 9-3. Profiles for different variables (void ratio, dry density, axial stress, shear stress and suction) are illustrated for different times (1, 2, 5, 10, 20, 34 and 60 kyr) for the case A1 (with axial swelling, a mass loss rate of 150 g/yr and a friction angle of 7.2°) in Figure 9-1. In addition, the time evolution of the total mass loss and the length of the geometry is shown. The void ratio at the erosion plane increases successively up to a level of 3, corresponding to a dry density level of ~700 kg/m^3, after a time period of 34 kyr. A cavity is formed after this and the erosion plane starts to move inwards, which means that the length of the entire geometry decreases (lower right graph in Figure 9-1). The total loss of dry mass at the time of cavity formation is 5 160 kg. It can be noted that the dry density level at the far end of the geometry is hardy affected at the when the cavity is formed. The stress conditions are characterized by a non-homogenous axial stress distribution in which the axial stress drops significantly at the erosion plane, and that these stress profiles are balanced by the shear stresses at the lateral boundaries. The shear stress displays profiles with a local maximum at level of 0.5–0.6 MPa. The triangular shape is caused by the lateral stress distribution and the friction angle on the slope towards the erosion plane, and by the displacements and the assumed shear modulus on the slope towards the far end. Finally, the initial suction profile displays a slope from zero at the erosion plane to a level of ~ 200 kPa at the far end of the geometry. This level decreases with time to a level of ~ 20 kPa when the cavity is formed, after which the suction profile change sign.

The radial swelling model with a mass loss rate of 150 g/yr and a friction angle of 7.2° (R1) displays many similarities but also some differences (Figure 9-2). The void ratio at the inner radius increases successively up to a level of 3, although the gradient is more pronounced than in the axial case. This implied that the cavity formation occurred already after 8 kyr and a total mass loss of 1 206 kg. The radial stress profile was balanced both by the arching effect, reflected by the relatively high tangential stresses, and the shear stresses caused by the wall friction. Finally, the suction value at the outer radius was approximately twice as high as for the A1 model.

Profiles of void ratio and suction are shown for different times for the corresponding models with a mass loss rate of 10 g/yr and a friction angle of 7.2° (A2 and R2) in Figure 9-3 together with time evolutions of the total mass loss and the dimension of the model geometries. It can be noted the void ratio profiles are very similar to the cases with higher erosion rates. However, the time scale to reach the different profiles is significantly longer, and the critical void ratio level of 3 is reached after 517 kyr and 125 kyr for the models with axial and radial swelling, respectively. This is virtually 15 times longer than for the A1 and R1 cases described above, and therefore strongly related to the assumed erosion rates.

The time evolution of the mass losses in the lower graphs shows that the mass losses at the time when the cavities are formed are very similar to the mass losses for the A1 and R1 cases. The results therefore show that the hydraulic conductivity has a very limited influence on the results for the investigated erosion rates. It can nevertheless be noted that the suction levels are essentially one order of magnitude lower than for the A1 and R1 cases.

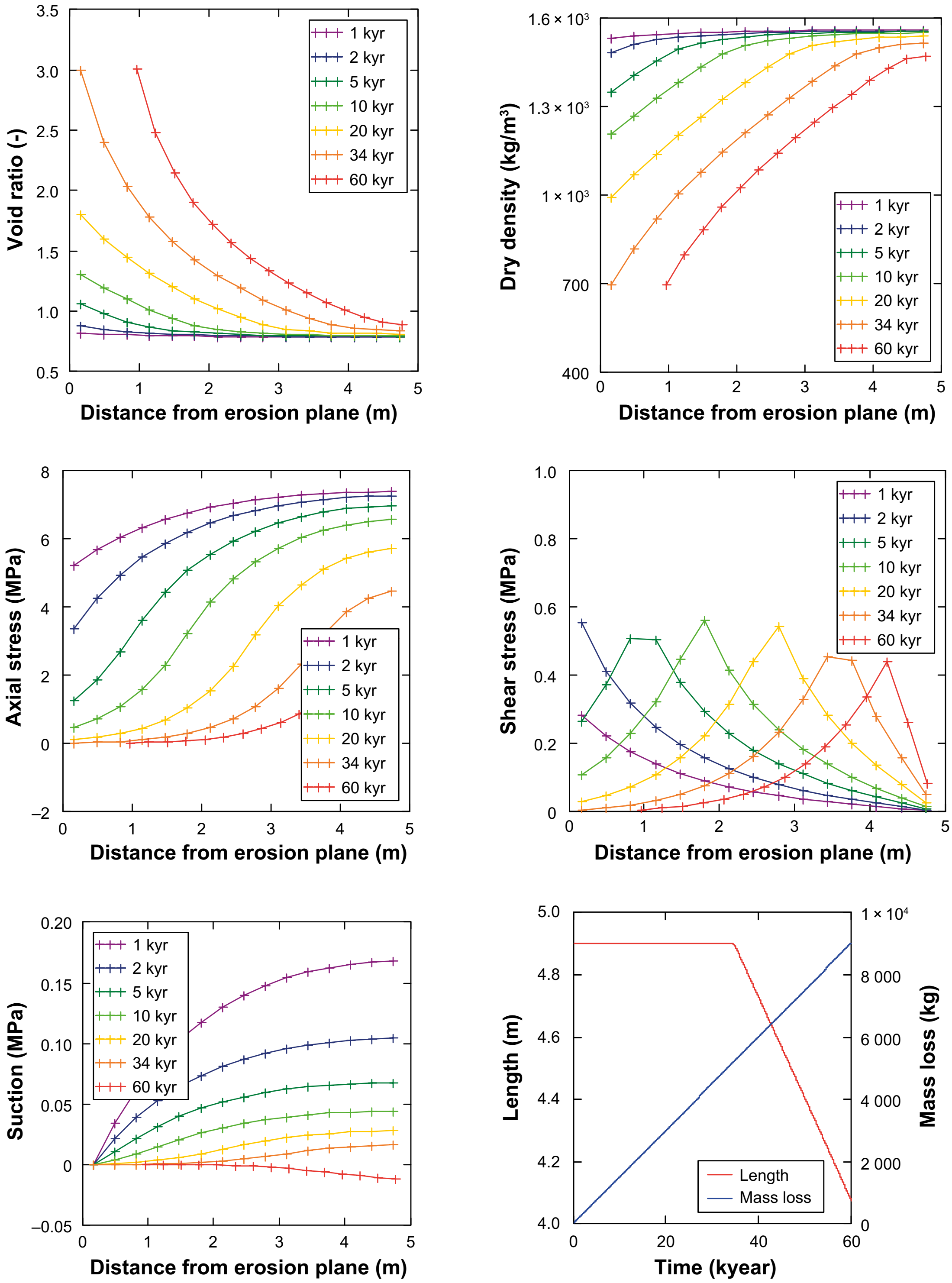

Figure 9-1. *Model results for a case with axial swelling, a mass loss rate 150 g/yr and θ = 7.2° (A1).*

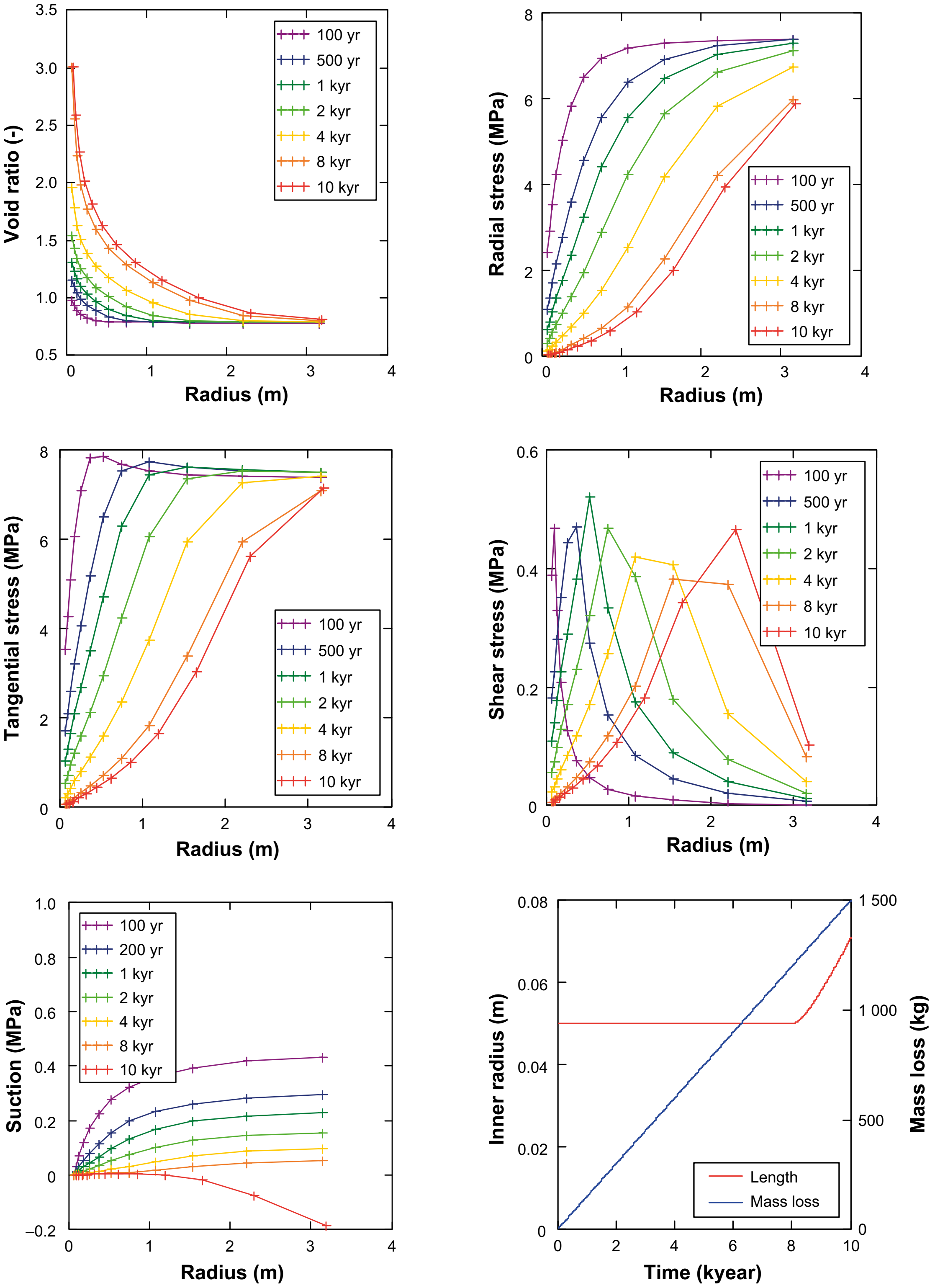

Figure 9-2. *Model results for a case with radial swelling, a mass loss rate 150 g/yr and θ = 7.2° (R1).*

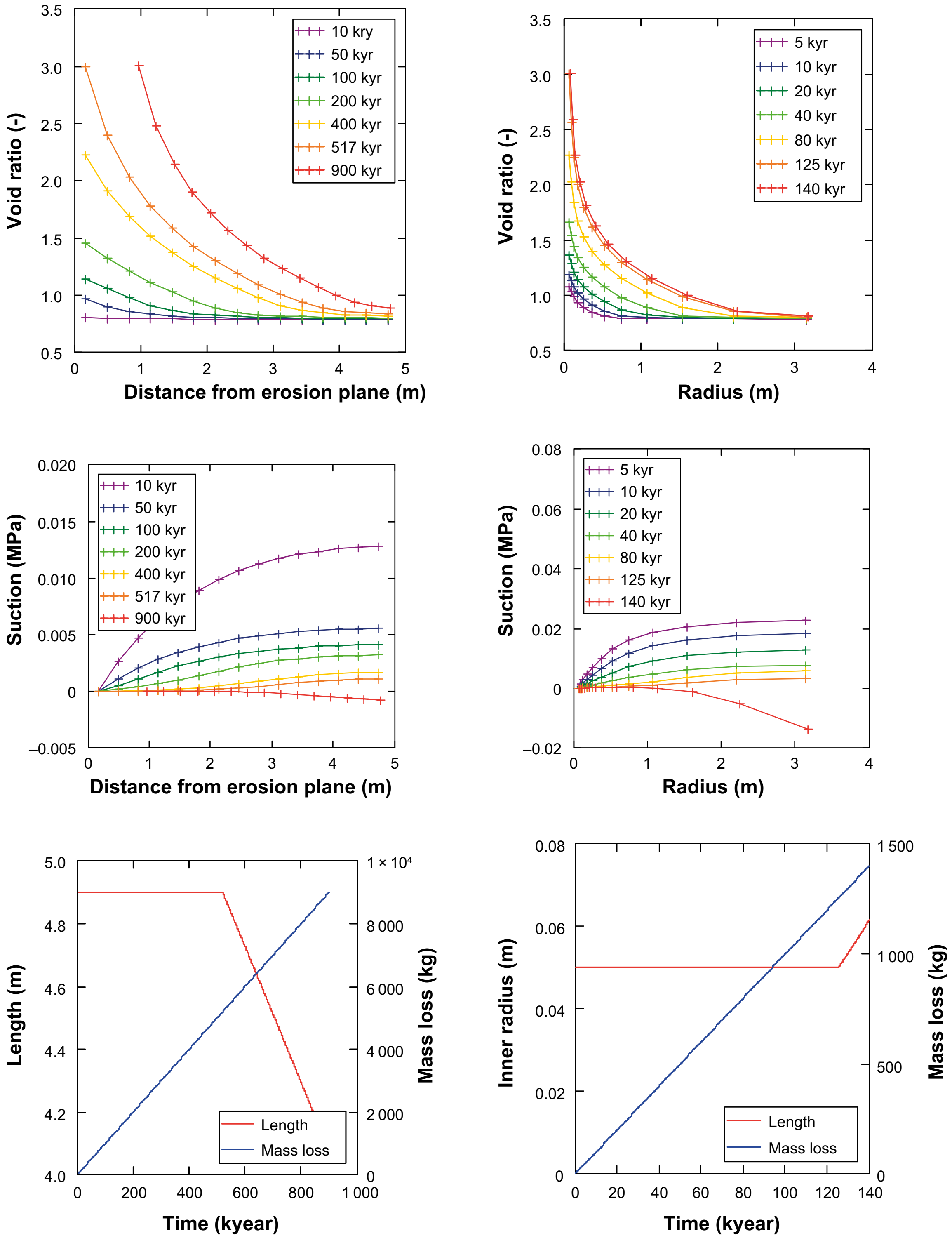

Figure 9-3. *Model results for cases with a mass loss rate 10 g/yr and θ = 7.2°. Axial swelling, A2 (left) and radial swelling R2 (right).*

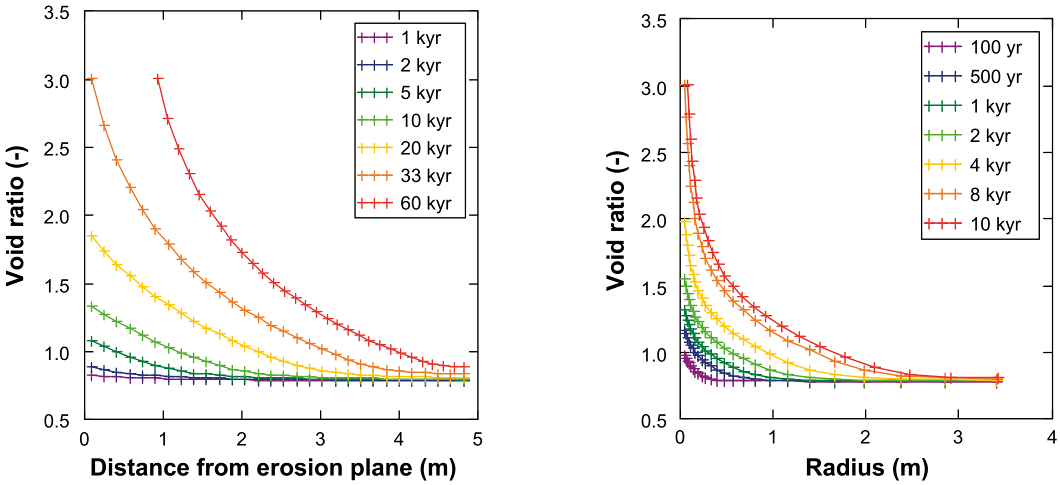

Figure 9-4. *Model results for cases with mass loss rate 150 g/yr and $\theta = 7.2°$ and double number of elements. Axial swelling, A1_mesh (left) and radial swelling R1_mesh (right).*

Numerical convergence

The accuracy of the numerical method could be tested and verified by rerunning the A1 and R1 models for cases with twice as many elements as in the base case models. The number of elements for the axial swelling cases was increased from 15 to 30, and the corresponding number for the radial swelling was increased from 12 to 24. Void ratio profiles are shown for different times in Figure 9-4. It can be noted that these profiles are virtually identical to the void ratio profiles in Figure 9-1 and Figure 9-2, respectively. This therefore shows that the numerical solution was sufficiently accurate.

Relevance of used material model

The relevance of the used material model was verified by calculation of the mean stress (p) and the von Mises stress (q) for a set of different times for each element in the base case models with doubled mesh. These are illustrated by plotting the void ratio versus the mean stress, and the von Mises stress versus the mean stress in different graphs (Figure 9-5). These graphs can in turn be compared with empirical data from swelling pressure tests (shown separately in the lower graph) and triaxial compression tests (shown as an adopted $q_f(p)$-relation together with the modelled q-p results). It can be noted that the modelled e-p results are very similar to the measured swelling pressure data, and that the modelled p-q results fall precisely on, or just below, the empirical relation from the triaxial compression tests. The used material model could therefore be regarded as verified.

Influence of friction angle and shear module

The base cases were defined for an assumed friction angle (7.2°) between the bentonite and the boundaries corresponding to the canister and the rock wall. The potential reduction of wall friction with time motivated an analysis of the influence of the friction angle on the time to reach cavity formation. Results on shear stress profiles and time evolution of the total mass loss are shown in Figure 9-6 for models with half the friction angle (i.e. 3.6°). It can be noted that the maximum shear stress is approximately 0.3 MPa, and that the time to reach the critical void ratio level was 55 kyr and 15 kyr for the models with axial (A3) and radial (R3) swelling, respectively, which is more than 50 % longer as compared with the base cases A1 and R1.

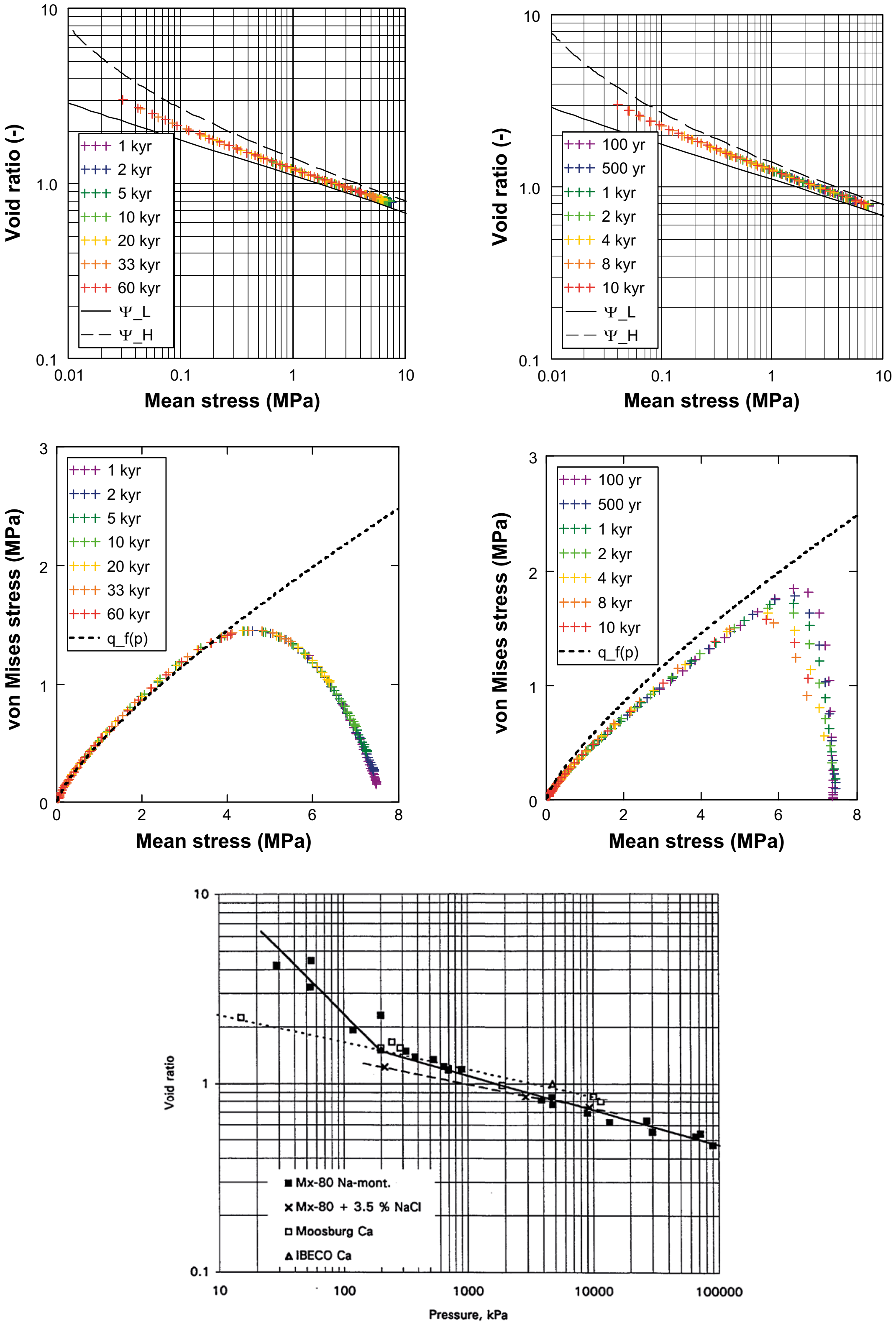

Figure 9-5. *Model results for cases with mass loss rate 150 g/yr and θ = 7.2° and double number of elements. Axial swelling, A1_mesh (left) and radial swelling R1_mesh (right). Void ratio versus evaluated mean stresses (upper graphs) and evaluated von Mises stresses versus mean stresses (middle graphs). Experimental swelling pressure data (lower graph) and empirical line for triaxial compression tests, i.e. deviatoric stress at the point of failure, versus the mean effective stress, (middle graphs) from Börgesson et al. (1995).*

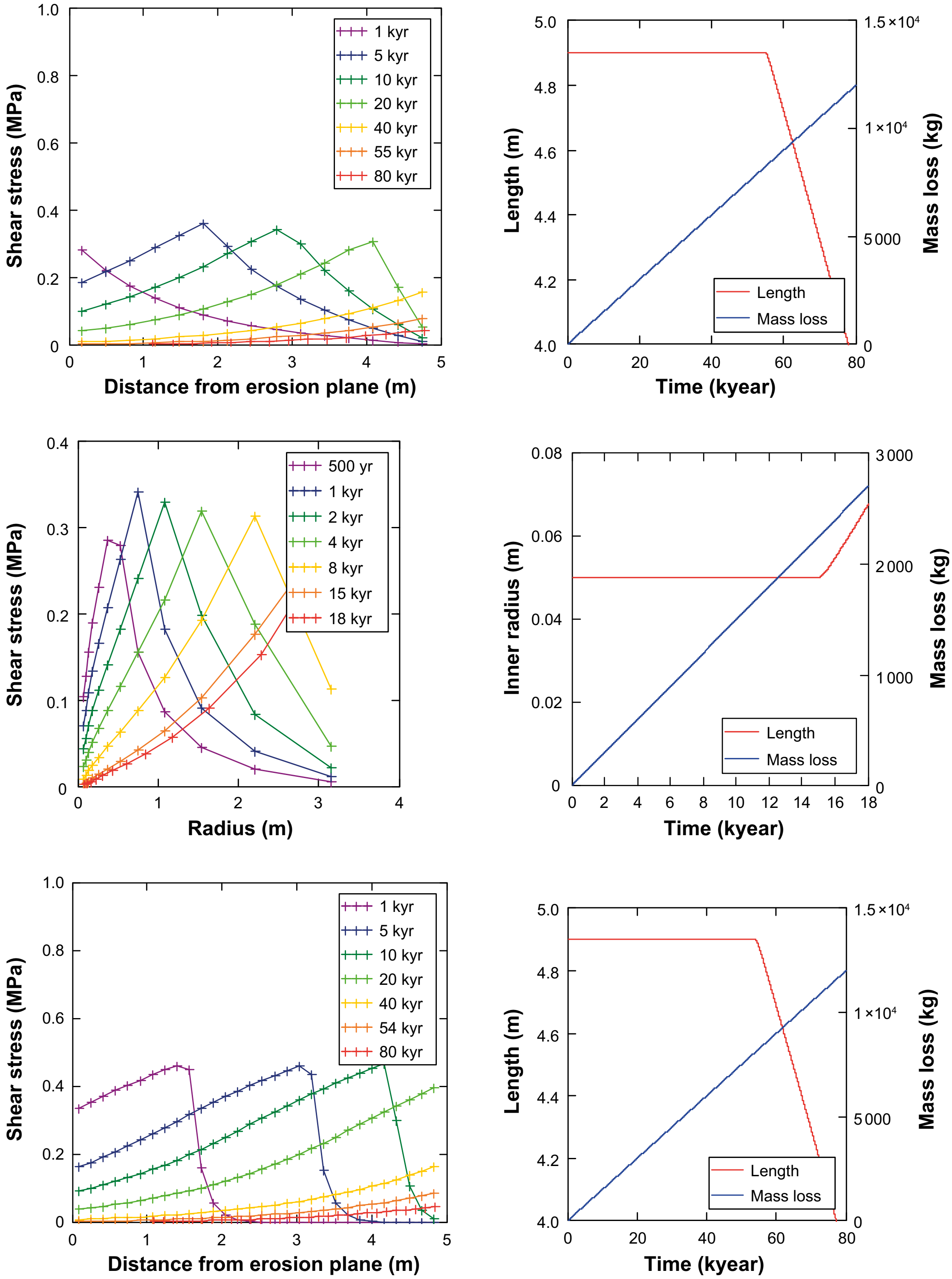

Figure 9-6. *Model results for cases with mass loss rate 150 g/yr and $\theta = 3.6°$. Axial swelling, A3 (upper), radial swelling R3 (middle row) and axial swelling with $K_s = 1\,000$ MPa/m and double number of elements, A3_mesh_Ks (lower).*

In addition, the influence of the shear module (K_s) was investigated by increasing this parameter with two orders of magnitude (from 10 to 1 000 MPa/m) for the A3 model. The time scale to reach cavity formation (i.e. 54 kyr) was only slightly shorter than for the case with the lower K_s value. The increased K_s value had however a significant influence on the shape of distributions of stresses and suction, especially the shear stress profiles as shown in Figure 9-6. These display a saw-toothed shape with a sloping gradient towards the plane of erosion (caused by the lateral stress distribution and the friction angle), and a sharp drop towards the far end of the geometry (caused by the displacements and the K_s value).

The time to reach cavity formation and the corresponding mass losses for all modelled cases are compiled in Table 9-1.

9.2 Simplified models

The simplified models described in Appendix D can be used in two ways. The simplest way is to generate void ratio profiles for a given boundary void ratio and a given friction angle. A more advanced utilization it to integrate the dry density along the volume of the geometry and thereby calculated the total dry mass of the entire geometry, and by relating this mass to the initial dry mass and the rate of erosion, the time to reach the given void ratio profile can be calculated.

Analytical void ratio profiles are shown together with results from the numerical models (A1, A3, R1 and R3) for the times when the critical void ratio of 3 is reached (Figure 9-7). It can be noted that the overall agreement between numerical and simplified solutions is quite good. Small discrepancies arise from the fact that the void ratio of each element in the numerical models is representative for the entire width of each element. This means that the boundary void ratio is located half an element-width from the actual boundary on the "inside" of the geometry. And this is one of the causes for the differences displayed, especially for the axial models. A second deviation is that the analytical solutions don't have any inherent mechanism for levelling out at the initial void ratio. This is instead handled with a simple condition that the void ratio shall not fall below the initial value. This can be noted for the base case with radial swelling (R1).

The method of calculating the time to reach a specific void ratio at the boundary is demonstrated for a number of conditions in Figure 9-8. On one hand, the boundary void ratio is presented as a function of time for two different friction angles (upper graphs). On the other hand, the time to reach a boundary void ratio of 3 is presented as a function of the friction angle (lower graphs). The corresponding times obtained by the numerical models with an erosion rate of 150 g/yr are also marked in the graphs. It can be noted that the agreement is fair although that some differences are noticeable. These results also strengthen the notion that the hydraulic conductivity doesn't influence the time to reach a specified void ratio level for these erosion rates, which was noted above in the comparison of the results for some of the numerical models above.

Table 9-1. Compilation of model results.

Model	Erosion rate (g/yr)	Friction angle (°)	Time (kyr)	Mass loss (kg)
A1	150	7.2	34.4	5 160
A1_mesh	150	7.2	33.2	4 986
A1_mesh_Ks	150	7.2	32.6	4 885
A2	10	7.2	517	5 170
A3	150	3.6	54.8	8 223
A3_mesh_Ks	150	3.6	53.9	8 081
R1	150	7.2	8.04	1 206
R1_mesh	150	7.2	7.92	1 188
R2	10	7.2	125	1 250
R3	150	3.6	15.0	2 245

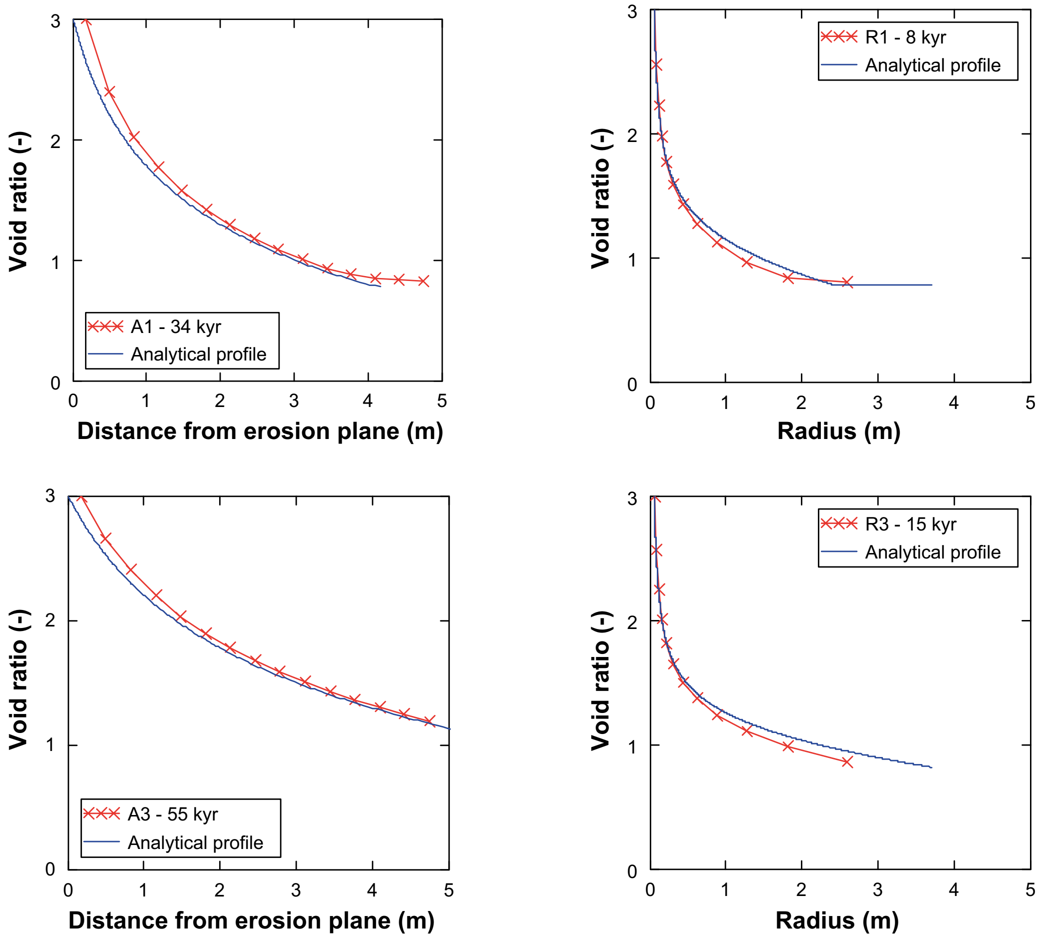

***Figure 9-7.** Model results for cases with mass loss rate 150 g/yr and θ = 7.2° (upper) and 3.6° (lower).*

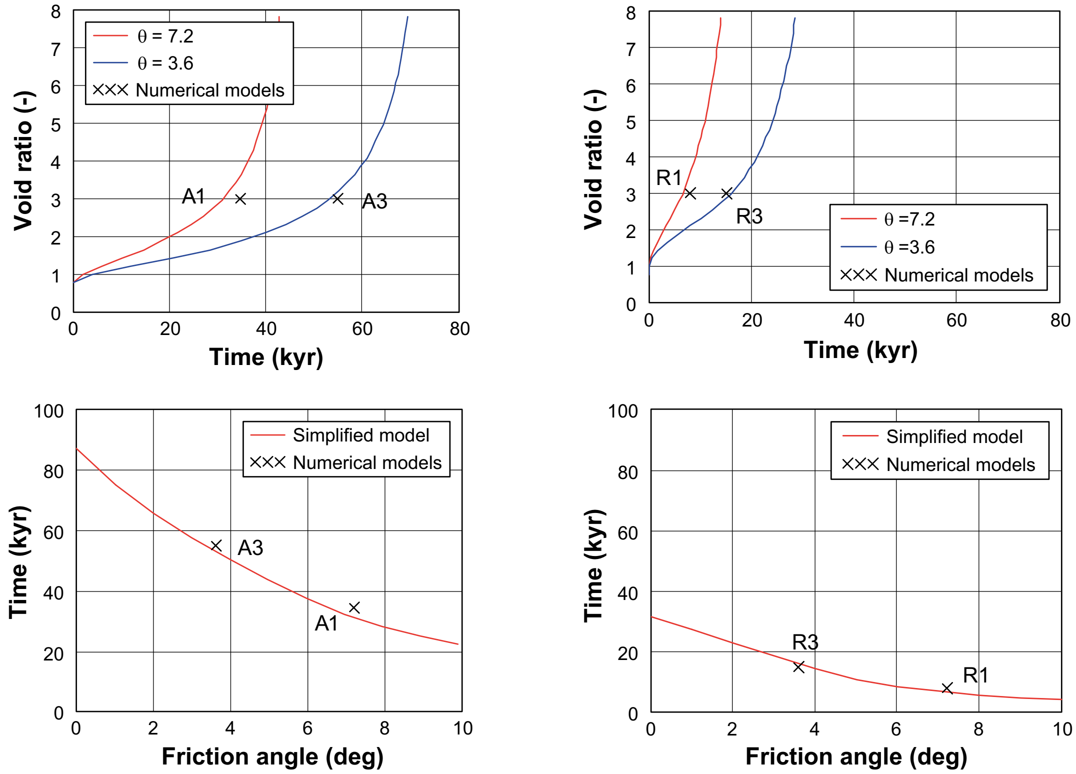

***Figure 9-8.** Model results for cases with mass loss rate 150 g/yr. Axial (left) and radial (right).*

The calculated relations between the boundary void ratio and time, especially for the axial swelling models, show that the rate by which the void ratio increase with time (i.e. de/dt) appears to increase markedly at a void ratio level of 3. This therefore illustrates that this value can be a regarded as a reasonable critical threshold for cavity formation. Even if the actual value would be twice as high, this relation indicates that the time to reach that level would be significantly shorter than twice as long.

These calculations generally justify the basic assumptions on which the analytical void ratio profiles are based. These profiles can therefore be utilized to make judgement regarding the likelihood of the development of certain shapes of the cavity. This in discussed further in the next chapter.

Finally, the simplified method for calculating the time to reach a specific void ratio for cases radial swelling was used to investigate the influence of the inner radius of the geometry (Figure 9-9). Changing the inner radius while keeping the outer radius constant will obviously influence the total volume, but this effect is marginal in comparison to the hydromechanical effects and was therefore disregarded. It can be noted that the influence of the inner radius is significant, and it is therefore not obvious how to justify a specific value. Nevertheless, erosion from a point fracture (with limited extension) should imply a radial swelling towards such a point. This was also the basis for the half-spherical geometries analysed by Åkesson et al. (2010a, Chapter 6). Beyond a certain distance from a point fracture (probably related to the width of the buffer) it should therefore be relevant to represent the void ration distribution with the analytical void ratio profiles outlined in this study.

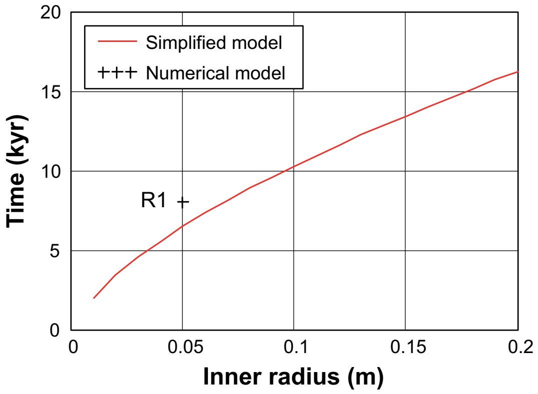

Figure 9-9. *Model results for radial swelling with mass loss rate 150 g/yr and $\theta = 7.2°$ with varying inner radius.*

10 Discussion

The geometries of the cavities formed in the models presented in this study was either rectangular (axial swelling) or cylindrical (radial swelling). This should of course not be taken literally since it would imply that bentonite was destroyed along the plane of erosion or the inner radius. A more realistic shape of cavities during the early stage of cavity formation should rather be that of a half torus (in the case of circular fracture) or a half sphere (in the case of a point fracture). An important question for this study was whether it's very pessimistic to assume that the shape of a half torus will be sustained once the width of buffer has been penetrated and the canister exposed to water. This issue can tentatively be addressed by considering void ratio profiles for axial and radial swelling, respectively.

The problem is illustrated in the left graph in Figure 10-1. The picture shows vertical sections through the buffer. The buffer in the left picture is penetrated by an idealized erosion plane corresponding to the axial swelling model, and the void ration profile above (and below) this plane can be described with the analytical profile for axial swelling. Such a profile with a boundary void ratio of 3 is shown in the diagram to the right.

A half-torus shaped cavity has been formed in the buffer in the adjacent graph. This cavity is simplified as a half cylinder with infinite length and with a half infinite buffer in which the radial void ratio profile towards the cavity can be described with the analytical expression obtained for the simple case without any friction. In order to relate such a profile with the axial swelling profile it should be most relevant to compare void ratios for the same distance from the plane of erosion. This can easily be done by calculating the distance (y) as a side of a triangle with the other side defined as the radius of the cavity (r_0), and the radial position (r) as the hypotenuse. Such profiles are shown for three different cavity radii (d/4, d/2 and d, where d is the width of the buffer) in the diagram to the right. This comparison shows that the void ratio gradient is highest for the case with small cavity radius (d/4), whereas the lowest gradient is found for the case with the large cavity radius (d). The void ratio gradient for the case with axial swelling is found between these extremes.

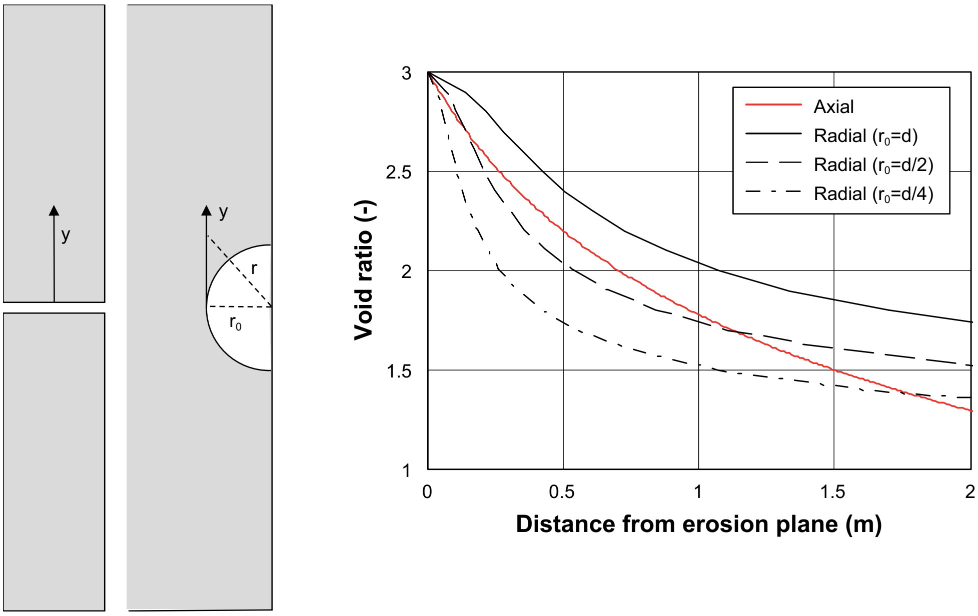

Figure 10-1. Schematic illustration of two modes of erosion (left). Calculated void ratio profiles (right).

The profile with the highest void ratio gradient implies a smaller loss of dry mass than for the profile with the lower void ratio gradient. This should also imply that a profile with a higher gradient is more stable. This means that for a localized mass loss along a circumferential fracture, this should initially lead to the formation of half torus shaped cavity. According to relation between time and the inner radius shown in Figure 9-9 there will actually be a cavity formation very soon after erosion begin, although the radius of the will be very small. This is consistent with models of self-sealing of long small pipes presented by Åkesson et al. (2010a) in which all calculations yielded a remaining hole after completed swelling. However, with a sustained rate of erosion the radius of the half-torus shaped will increase which in turn will imply a reduced void ratio gradient. At some stage during the growth of cavity it should however be more stable to have a void ratio gradient which is caused by wall friction, rather by the arching effect. This should therefore lead to the formation of a cavity with a more rectangular shape which penetrates the entire width of the buffer.

A hypothetical cavity exhibiting a semi-circular shape, which precisely reaches and thereby exposes the canister surface, is therefore not realistic. Such a shape would be equivalent to truncated arch in which the stress line would be replaced with the frictional forces acting on a horizontal slab on top of the truncated arch. However as illustrated in Figure 10-2, the radial stress at the surface of the cavity is zero, whereas the tangential stress is significantly larger than the radial stress and essential given by the maximum von Mises stress for the critical void ratio. In contrast, the shear stress caused by wall friction is significantly smaller than the normal stress, which in turn should be essentially zero. Such a stress balance is therefore not realistic.

Remaining uncertainties

The complexity of the analysed problem implies that there are several remaining uncertainties which should be observed. These can either be related to the understanding of the processes or to the capabilities of the hydromechanical model. The following remarks can be made regarding the process-related uncertainties:

The rate of erosion. This quantity was simply treated as a constant in the presented calculation, and the used values were adopted from results presented by Neretnieks et al. (2017). No feed-back mechanism through which the reduction of the dry density in the buffer could influence the rate of erosion was included.

The rate of sol formation. The erosion rate from a formed cavity can according to SKB (2011) (Section 10.3.11) be expressed as the product of the volumetric flow through the cavity and the concentration of clay particles in the cavity. However, such a description appears to evade the governing process, i.e. the rate of sol formation from the gel/sol interface, since this rate should be equal to the erosion rate at steady-state conditions. No information of such a process is available to the author's knowledge.

Notion and value of a critical void ratio. A maximum value for the void ratio was introduced in the presented model. The value of 3 was chosen since the material model simply hasn't been used above this level before. A maximum void ration should imply that the swelling pressure (or perhaps the Ψ_L function in the HBM model) is zero. Such a limit should correspond to the sol/gel interface, but at low salinities this should imply a void ratio level much higher than 3.

Potential influence of creep deformation. Data for deviatoric creep deformation was presented by Börgesson et al. (1995) and has been used for canister sinking calculations (Åkesson et al. 2010a). Such process could potentially influence the formation of cavities in two ways: i) by affecting the anisotropic stress conditions and thereby reducing the von Mises stresses in the bentonite; and ii) by affecting the anisotropic stress conditions and thereby reducing the friction angles at the lateral boundaries. The understanding of this process is however too limited to be taken into account for simulating cavity formation.

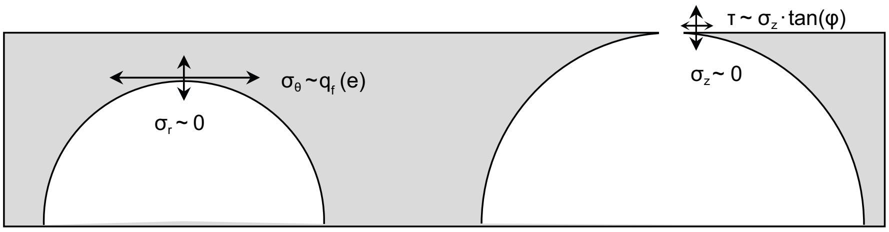

Figure 10-2. Schematic illustration of the mechanical consequences of a hypothetical cavity exhibiting a semi-circular shape precisely exposing the canister surface.

The following remarks can be made regarding the model-related uncertainties:

Complex geometries. The numerical models which were developed for this task were limited to simple 1-D geometries. There is currently no numerical tool which can handle the hydromechanical problem for the actual 3D or axisymmetric 2D geometry, especially not for cases in which there is a defined loss of dry mass localises to a fracture which intersects the deposition hole. In addition, the transition from a small semi-circular cavity caused by arching effects, to a large rectangular cavity caused by wall friction, may possibly involve a collapse which probably cannot be described by any hydromechanical model.

Large strains. The presented models included explicit quantification of strains and displacements. The used strains were however based on the small-strain definition. Moreover, the initial coordinates for the nodes were used to quantify the original coordinates used for strains in the model for radial swelling (e.g. r in $\partial u_r/\partial r$), although this is a simplification. The only use of the quantified displacements was to calculate the build-up of shear stresses for small displacements, and the shear modulus (K_s) was the controlling parameter for this. However, even if the magnitude of K_s is largely unknown, it was found that the value for this had only minor influence of the time to reach cavity formation.

11 Summary and conclusions

Numerical models were developed for two different one-dimensional geometries, with axial and radial swelling, respectively. These models were used to calculate the time until cavity formation and corresponding total mass loss for cases with assumed erosion rates and frictions angles. These models showed that:

- The base case model for axial swelling with an erosion rate of 150 g/yr and friction angle of 7.2° resulted in cavity formation after 34 kyr and a total mass of 5 160 kg. The corresponding result for radial swelling was 8 kyr and 1 206 kg.
- Models for axial swelling with the same friction angle, but with an erosion rate of 10 g/yr resulted in cavity formation after 517 kyr and a total mass of 5 170 kg. The corresponding result for radial swelling was 125 kyr and 1 250 kg. This showed that the hydraulic conductivity had a very limited influence on the results for the investigated erosion rates.
- Model cases for which the number of elements was increase with a factor of two resulted in virtually identical void ratio profiles which confirmed that the numerical solution was sufficiently accurate.
- Comparison of evaluated mean stresses and von Mises stresses from the model results showed that these were very similar to empirical data from swelling pressure tests and triaxial compression tests. The used material model could therefore be regarded as verified.
- Model cases for which the friction angle was decreased with a factor of two resulted in cavity formation after 55 and 15 kyr for axial and radial swelling, respectively. Cases in which the shear modulus was increased two orders of magnitude had however only a marginal influence on the time of shear cavity formation.

The stress equilibrium relations were used, together with the constitutive relations defined by the HBM model, to derive analytical expressions for stable void ratio profiles with a specified boundary void ratio. Such profiles were compared with results from the numerical methods (cases A1, A3, R1, R3) for the time when the critical void ratio level was reached in each case. And it was found that the numerical results could be fairly well reproduced with the simplified solutions.

The analytical void ratio profiles, especially for radial swelling without friction, was a novel outcome from this task which should be useful for the understanding of the stability of erosion channels.

The total dry mass of the entire geometry could be calculated by integrating the dry density distribution based on the analytical void ratio profiles. And by relating this mass to the initial dry mass and the rate of erosion, the time to reach a given void ratio profile could be calculated. Different dependencies were analysed in this way, for both axial and radial swelling: e.g. time versus boundary void ratio and time versus friction angle, and these showed fairly good agreement with the numerical models. Moreover, for radial swelling the relation between time and the inner radius was analysed and this displayed a quite strong relation, which implies that cavity formation may occur quite fast for a highly localized line of erosion.

Finally, a void ratio profile associated with axial swelling with wall friction, were compared with profiles associated with radial swelling without wall friction. From this comparison it was argued that a hypothetical cavity which exhibits a semi-circular shape which precisely exposes the canister surface is not realistic. An additional argument for this was that the forces upheld by the tangential stresses in an arch are much larger than the potential friction forces acting on the canister surface in such a condition.

Appendix B

The HBM model

B1 Introduction

The Hysteresis Based Material (HBM) model has been developed with the aim to obtain a robust hydro-mechanical model for high density bentonite materials, with a high predictive capability (Börgesson et al. 2020, Dueck et al. 2019). The HBM model was defined for water saturated conditions by making the following three basic assumptions:

1) The model is based on an expression for the *chemical potential* of the clay water and its pressure dependence. From this follows that the sum of *suction* (s) and *pressure* (p) is equal to a quantity, denoted the *clay potential* (Ψ), which in turn is a function of the void ratio (e), $s+p=\Psi(e)$. This means that the clay potential is equal to the suction value at unconfined conditions, ($p=0$), and also that it equals the pressure at confined conditions with free access of water, ($s=0$).
2) In order to obtain a description which captures the *hysteretic behaviour* (path dependency) observed in oedometer tests and water retention measurements, and the *shear strength* observed in unconfined compression tests and triaxial tests, the following assumptions have been adopted.
    (i) The clay potential for a specific void ratio is assigned a value in an *allowed interval bounded by two functions*. One function during swelling conditions (Ψ_L) and the other for conditions during consolidation (Ψ_H).
    (ii) The actual state between these functions for a given direction is governed by the *history of the strains* in that direction.
    (iii) The difference between the states in different directions *should not exceed half the allowed interval (i.e.* $\Psi_{\Delta/2}=(\Psi_{\mathrm{H}}-\Psi_{\mathrm{L}})/2$).
3) The *density of water* is defined as a function of suction, i.e. $\rho_w(s)$. This means that the compressibility of water is assumed to be applicable for positive suction values as well as for positive pore pressures (which basically are equivalent to negative suction values). For the models presented in this work it could however be assumed that water is incompressible.

B2 Isotropic model

The *chemical potential of the clay water* (μ) is used as a starting point for the mechanical material model. For isotropic conditions, this can be described as a function of the *relative humidity of the clay at free swelling conditions* (*RH*) and the (total) *pressure* (p):

$$\mu=\mu_0+RT\ln(RH)+v_c p, \tag{B-1}$$

where μ_0 is the chemical potential of a reference state, R is the universal gas constant, T is the absolute temperature and v_{c} is the molar volume of the clay water (Birgersson et al. 2010, Karnland et al. 2005). The relation above can be rearranged as,

$$-\frac{\mu-\mu_0}{v_0}=-\frac{RT}{v_0}\ln(RH)-\frac{v_c}{v_0}p, \tag{B-2}$$

where v_0 is the molar volume of bulk water. The term on the left-hand side can be identified as *suction* (s), while the first term on the right side from here on is denoted the *clay potential* (Ψ). Assuming that v_0 and v_{c} are equal the expression above can be written as:

$$s=\Psi-p. \tag{B-3}$$

It should be noted that the suction corresponds to the RH in an external gas phase. It also corresponds to the negative value of an external water pressure. This means that the clay potential is defined in a similar way as compared to an *effective stress*. It should also be noted that this description is based on the assumptions that the osmotic effect of any solution in the water can be disregarded and that the temperature is constant. An *isotropic* stress state is also assumed.

Common traits of experimental data for *RH* at free swelling conditions are: dependency on the *water content* (w) and presence of a hysteresis effect, i.e. path dependency. Since only water saturated conditions are considered here, w can be substituted with the void ratio (e). To indicate that the entire history of a variable up to time t is to be regarded, the variable is given a superscripted t, e.g. e^t. Using this notation, the clay potential can be defined as a function (indicated with a tilde above an entity) on the following format:

$$\tilde{\Psi}(e, e^t) = \tilde{\Psi}_M(e) + \tilde{\Psi}_{\Delta/2}(e)\tilde{f}(e^t) \tag{B-4}$$

where Ψ_M, $\Psi_{\Delta/2}$ and f denote the *mid-line*, the *half-allowed span*, and the *path variable*, respectively. It can be noted that Ψ_M, and $\Psi_{\Delta/2}$ are defined as functions of the void ratio, whereas f is a variable, with values belonging to $[-1,1]$, dependent on the void ratio history. The clay potential is thus confined to a region with two bounding lines: $\Psi_H = \Psi_M + \Psi_{\Delta/2}$ (the consolidation line obtained when $f = 1$) and $\Psi_L = \Psi_M - \Psi_{\Delta/2}$ (the swelling line obtained when $f = -1$), see Figure B-1.

The path variable (f) is obtained by integration over time,

$$f = f_0 + \int_{t_0}^{t} \frac{\partial f}{\partial e} \dot{e}\, d\tau, \tag{B-5}$$

where the differential is given by,

$$\frac{\partial f}{\partial e} = -\frac{K'}{1+e_0}(1 + \operatorname{sgn}(\dot{e})f). \tag{B-6}$$

The K'-parameter determine the path variable derivative at $f = 0$, the sign of the time derivative of the void ratio determines whether the value of f changes towards 1 or −1. The sign function is defined as:

$$\operatorname{sgn}(x) = \begin{cases} -1 & \text{if} \quad x < 0 \\ 0 & \text{if} \quad x = 0 \\ 1 & \text{if} \quad x > 0 \end{cases} \tag{B-7}$$

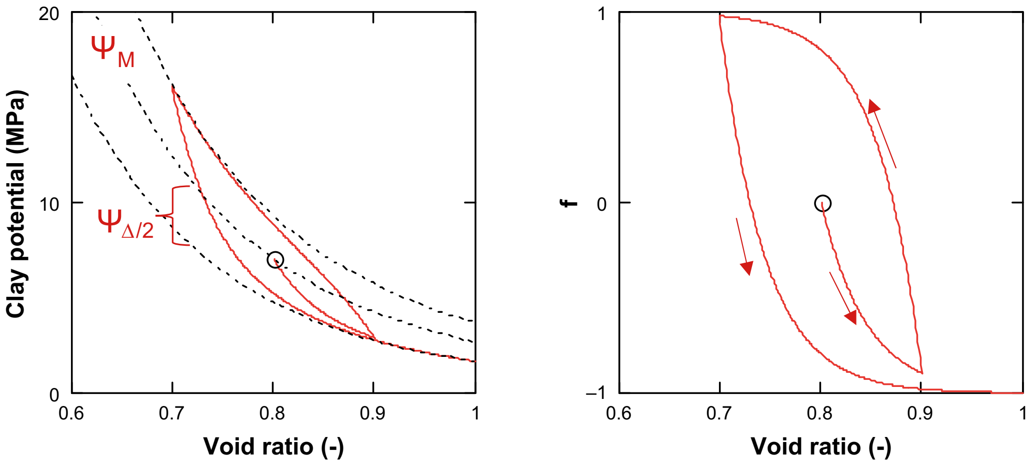

Figure B-1. *Clay potential and path variable (f) versus void ratio. Right graph shows an example of the path variable for a case with swelling, followed by consolidation and followed by swelling. Left graph shows the same path mapped on the region for the clay potential.*

B3 Principal direction model

The model applicable for cases of isotropic conditions has been expanded to also cover cases when the principal directions correspond to the Cartesian basis $\{e_1, e_2, e_3\}$. The generalized model reads:

$$
\begin{aligned}
-\boldsymbol{\sigma} &= \boldsymbol{\psi} - s\mathbf{1}\,,\\
\boldsymbol{\psi} &= \tilde{\psi}_M(\varepsilon_v)\mathbf{1} + \tilde{\psi}_{\Delta/2}(\varepsilon_v)\boldsymbol{f} \qquad \text{(B-8)}\\
\boldsymbol{f} &= \boldsymbol{f}_0 + \int_{t_0}^{t} \frac{\partial \boldsymbol{f}}{\partial \boldsymbol{\varepsilon}} \dot{\boldsymbol{\varepsilon}}\, d\tau .
\end{aligned}
$$

In this version of the model the path dependent variable f is a second order tensor,

$$\boldsymbol{f} = f_{11}\boldsymbol{e}_1 \otimes \boldsymbol{e}_1 + f_{22}\boldsymbol{e}_2 \otimes \boldsymbol{e}_2 + f_{33} \otimes \boldsymbol{e}_3 \otimes \boldsymbol{e}_3, \qquad \text{(B-9)}$$

and its derivative with respect to strain is given by,

$$
\begin{aligned}
\frac{\partial \boldsymbol{f}}{\partial \boldsymbol{\varepsilon}} = \frac{\partial f_{11}}{\partial \varepsilon_{11}}\boldsymbol{e}_1 \otimes \boldsymbol{e}_1 \otimes \boldsymbol{e}_1 \otimes \boldsymbol{e}_1 + \frac{\partial f_{22}}{\partial \varepsilon_{22}}\boldsymbol{e}_2 \otimes \boldsymbol{e}_2 \otimes \boldsymbol{e}_2 \otimes \boldsymbol{e}_2 + {}& \qquad \text{(B-10)}\\
\frac{\partial f_{33}}{\partial \varepsilon_{33}}\boldsymbol{e}_3 \otimes \boldsymbol{e}_3 \otimes \boldsymbol{e}_3 \otimes \boldsymbol{e}_3 \,.&
\end{aligned}
$$

The differential equations for the path variable components are given by:

$$\frac{\partial f_{\alpha\alpha}}{\partial \varepsilon_{\alpha\alpha}} = -K(\tilde{\kappa}(\boldsymbol{f}, \dot{\varepsilon}_{\alpha\alpha}) + \operatorname{sgn}(\dot{\varepsilon}_{\alpha\alpha}) f_{\alpha\alpha}), \qquad \text{(B-11)}$$

where $\alpha = \{1, 2, 3\}$ and no summation convention is to be used. In the expression above,

$$\tilde{\kappa}(\boldsymbol{f}, \dot{\varepsilon}_{\alpha\alpha}) = 1 - \Phi(\tilde{\gamma}(\boldsymbol{f}, \dot{\varepsilon}_{\alpha\alpha}))\tilde{\gamma}(\boldsymbol{f}, \dot{\varepsilon}_{\alpha\alpha}), \qquad \text{(B-12)}$$

where Φ is the Heaviside step function, and the $\tilde{\gamma}$-function is defined as,

$$\tilde{\gamma}(\boldsymbol{f}, \dot{\varepsilon}_{\alpha\alpha}) = f_T + \operatorname{sgn}(\dot{\varepsilon}_{\alpha\alpha}) f_P, \qquad \text{(B-13)}$$

f_T and f_P represents the "half-distance" and "mid-point" between the largest and smallest f-value, respectively, i.e.

$$f_T = \frac{\max(f_{ij}) - \min(f_{ij})}{2} \quad \text{and} \quad f_P = \frac{\max(f_{ij}) + \min(f_{ij})}{2}. \qquad \text{(B-14)}$$

The purpose of the $\tilde{\kappa}$- and the $\tilde{\gamma}$-function is to limit the maximum difference between the f-values in different directions to 1, thereby making sure that the shear strength of the material is taken into account (see Dueck et al. 2019 for further details).

B4 Parameter values

The presented model is specified with three parameter sets: the clay potential (i.e. $\Psi_M(e)$ and $\Psi_{\Delta/2}(e)$), the K parameter, and the hydraulic conductivity $K_H(e)$.

Clay potential

A swelling pressure function was adopted on the following form by Åkesson et al. (2010b), and with the following parameter values: $c_0 = -4.74$ $c_1 = 4.12 \times 10^{-3}$; $c_2 = -3.94 \times 10^{-7}$ (p_{sw} in MPa; p_d in kg/m^3):

$$\log^{10}(p_{sw}(\rho_d)) = c_2 {\rho_d}^2 + c_1 \rho_d + c_0 \qquad \text{(B-15)}$$

This can easily be converted to a function of the void ratio through the relation $e = \rho_s/\rho_d - 1$, where ρ_s is the solid density, for which the value 2 780 kg/m^3 has been used. This function has been used for lower bounding line $\Psi_L(e)$. A function with the same form was adopted for the Ψ_H relation by Börgesson et al. (2020). The following parameter values were found: $c_0 = -2.675$; $c_1 = 2.101 \times 10^{-3}$; $c_2 = 1.669 \times 10^{-7}$ (MPa). It should be noted that the used swelling pressure curve (B-15) to a large extent was based on free swelling retention data for an initial water content of 17 %. This curve is therefore less relevant for void ratios below a level of approximately 0.7. The bounding lines are in turn used to adopt the mid-line: $\Psi_M = (\Psi_L + \Psi_H)/2$, and the half-allowed span: $\Psi_{\Delta/2} = (\Psi_H - \Psi_L)/2$.

The K parameter

The *K* parameter was adopted from experimental results for three triaxial tests. This procedure resulted in a *K* value of 40.

Hydraulic conductivity

The hydraulic conductivity and its void ratio dependence were taken from the adoption by Åkesson et al. (2010b). Still, in order to mimic the results of the homogenization tests this parameterization was reduced with a factor of 2 which yields:

$$K_H(e) = 1.2 \cdot 10^{-13} e^{5.33}\ [m/s] \qquad \text{(B-16)}$$

Appendix C

One dimensional swelling models

C1 Problem description

The loss of bentonite due to erosion through a fracture intersecting the deposition hole will lead to a reduction of the dry density of the bentonite close to the fracture. This will lead to a local reduction of the swelling pressure which, in turn, will cause the surrounding bentonite to swell towards this zone. A sustained loss of bentonite and the reduction of the dry density to a hypothetical critical level at which the swelling pressure level is zero would mean that a cavity would form. Such homogenization processes have been investigated for simple one-dimensional geometries, axial and radial, and numerical methods were developed to solve these problems. The geometries of these models are shown in Figure C-1.

Apart from the hydromechanical behavior of the bentonite which was described with the HBM model, the numerical methods were based of four basic relations and conditions: i) Darcy's law; ii) the continuity equation; iii) relations between strains and displacements; and iv) the stress equilibrium relations. These are described in an analytical form below.

Darcy's law and flow rates

The volumetric flow rate of water (q_w) is given by Darcy's law, which here is formulated in terms of gradients of suction (s), the hydraulic conductivity (K) and the specific weight of water (γ_w). The gravity was disregarded in the flow calculation:

$$q_w = \frac{K}{\gamma_w} \nabla s \tag{C-1}$$

Since the bentonite is water saturated, and since both the bentonite and the water is regarded to be incompressible, this means that the volumetric flow rate of solids (q_s) is balanced by the volumetric flow rate of water:

$$q_w + q_s = 0 \tag{C-2}$$

Finally, boundary conditions can be specified for the outer boundary, close to the location of the erosion point, and the inner boundary at the far end from the erosion point:

$$q_s = \frac{r_m}{A \cdot \rho_s} \quad \textit{outer boundary} \tag{C-3}$$

$$q_w = 0 \qquad \textit{inner boundary}$$

where r_m is the erosion rate (mass per time unit), ρ_s is the solid density, and A is the area over which the erosion rate is evenly distributed.

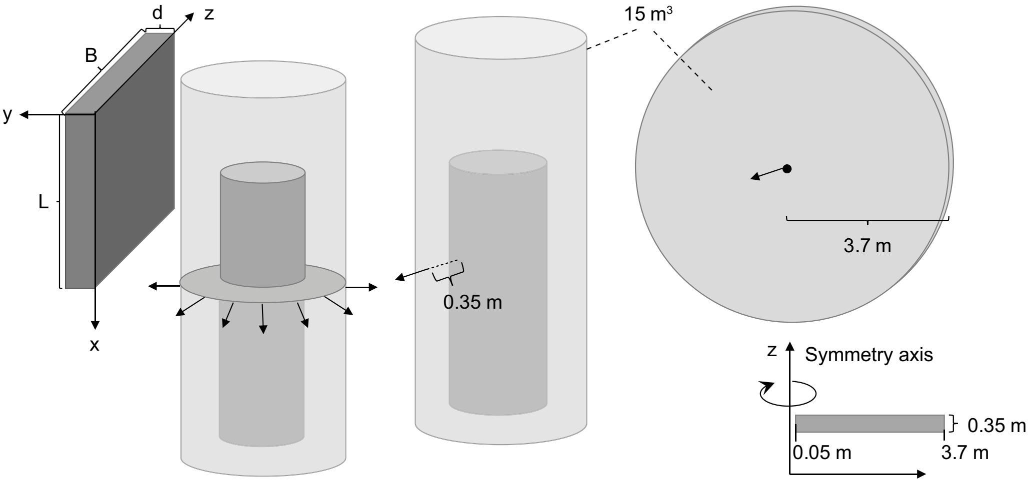

***Figure C-1.** Model geometry for axial and radial swelling*

Continuity equation

The mass flux of solids (j_s) is given as the product of the solid density and the volumetric flow rate of solids. According the continuity equation, the time derivative of the dry density (ρ_d) is equal to the negative value of the divergence of the mass flux of solids:

$$j_s = \rho_s \cdot q_s \qquad \text{(C-4)}$$

$$\frac{\partial \rho_d}{\partial t} + \nabla \cdot j_s = 0$$

Strains and displacements

A common condition for both geometries is that the sum of the strain components (i.e (ε_x, ε_y, ε_z)) for axial swelling and (ε_r, ε_θ, ε_z) for radial swelling) is equal to the volumetric strain (ε_v). Moreover, only axial and radial displacements (u_x and u_r) are considered in the two geometries, which means that the strain components can be identified as:

$$\varepsilon_v = \varepsilon_x + \varepsilon_y + \varepsilon_z = \frac{\partial u_x}{\partial x} + 0 + 0 \quad (axial\ swelling) \qquad \text{(C-5)}$$

$$\varepsilon_v = \varepsilon_r + \varepsilon_\theta + \varepsilon_z = \frac{\partial u_r}{\partial r} + \frac{u_r}{r} + 0 \quad (radial\ swelling) \qquad \text{(C-6)}$$

Stress equilibrium

The stress equilibrium conditions for the two geometries are defined as:

$$\frac{\partial \sigma_x}{\partial x} + \frac{2\tau}{d} = 0 \qquad (axial\ swelling) \qquad \text{(C-7)}$$

$$\frac{\partial \sigma_r}{\partial r} + \frac{\sigma_r - \sigma_\theta}{r} - \frac{2\tau}{d} = 0 \quad (radial\ swelling)$$

Where σ_x is the axial stress, σ_r and σ_θ is the radial and tangential stress, respectively, τ is the shear stress at the lateral boundary, and d is the thickness of the geometry. It should be noted that τ is included as a body force since a 1D approach is used. It should also be noted that stresses are defined as positive for compressive stresses. The shear stress is defined as positive in the opposite direction as the swelling. The shear stress is calculated as the minimum value of the product of the displacement and the shear module (K_s); and the product of the lateral stress and the tangent of the friction angle (φ):

$$\tau = \min\left[K_s \cdot u_x, \sigma_y \cdot tan\varphi\right] \quad (axial\ swelling) \qquad \text{(C-8)}$$

$$\tau = \min[-K_s \cdot u_r, \sigma_z \cdot tan\varphi\,] \quad (radial\ swelling)$$

This is combined with the stress equilibrium conditions and the relations between stresses, clay potentials and suction:

$$\frac{\partial \Psi_x}{\partial x} - \frac{\partial s}{\partial x} + \frac{2}{d}\min\left[K_s \cdot u_x, (\Psi_y - s) \cdot tan\varphi\,\right] = 0 \qquad (axial) \qquad \text{(C-9)}$$

$$\frac{\partial \Psi_r}{\partial r} - \frac{\partial s}{\partial r} + \frac{\Psi_r - \Psi_\theta}{r} - \frac{2}{d}\min[-K_s \cdot u_r, (\Psi_z - s) \cdot tan\varphi\,] = 0 \quad (radial)$$

C2 General considerations

Two numerical methods based on finite differences were developed to solve one-dimensional homogenization processes (axial and radial) for a water-saturated bentonite specimen, confined in all directions, but from which bentonite is lost at a specified rate at one of the boundaries (r_m). The specimen has also free access of water (i.e. zero suction) at this boundary and will therefore swell in this direction, but this is countered by the frictional forces acting along two of the lateral sides of the geometry. If the void ratio at the boundary reaches a critical value (e_M), then this void ratio will be kept constant. This will therefore act as a mechanical boundary condition, which in turn means that the length of the specimen will decrease (Figure C-2).

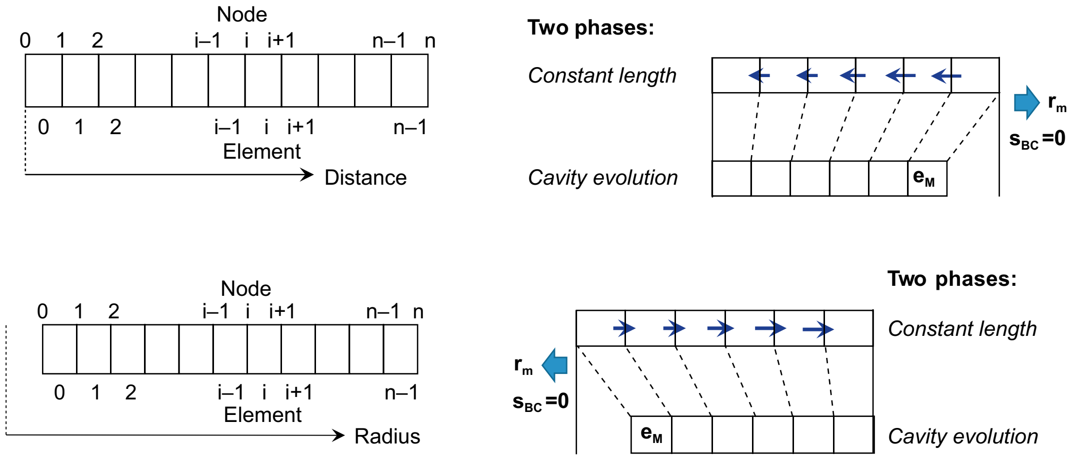

Figure C-2. *Geometry with defined distance from fixed boundary (left) and schematic illustration of two phases (right).*

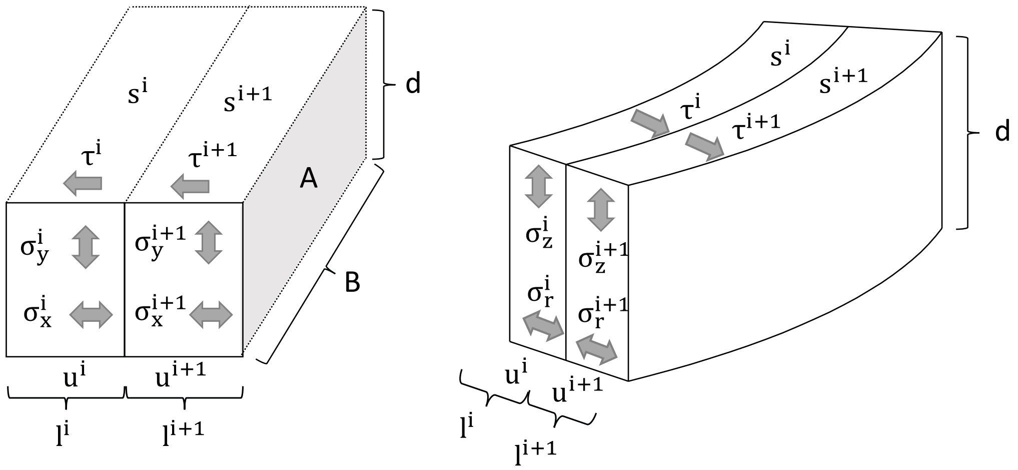

Figure C-3. *Schematic illustration of two adjacent element with variables of relevance for the integration of the suction profile. Axial swelling (left) and radial swelling (right).*

The geometry for each numerical method was discretized as an array of n elements (with index 0 to n-1) and with adjacent nodes (with index 0 to n). The nodes and elements in the axial geometry were numbered with zero at the fixed (unaffected) boundary, while in the radial geometry the nodes and elements were numbered with zero at the inner radius with a prescribed mass loss rate. The axial model was discretized so that all elements had equal initial length. In contrast, the radial model was discretized so the ratio between the radiuses of all adjacent nodes (γ) was the same. The length of all elements (axial) and the radius of all nodes (radial) stayed constant as long as the void ratio at the mass loss boundary was below the critical value. However, as soon as this value reached the grid was displaced with a homogenous size reduction of each element. This either implied equal length of all elements (axial) or equal ratio between radii of all adjacent nodes (radial).

In order to calculate the velocity of the nodes and the solids, three conditions is taken into account. The first is the fulfilment of the mass balance (or volume balance) at each node:

$$q_w^i + q_s^i + \mathrm{v}^i = 0 \qquad \text{(C-10)}$$

The second was condition for homogenous size reduction. For the axial model this means that the velocity of each node is a multiple of the node number, whereas for the radial model it means that the velocity can be described by a geometric relation:

$$\mathrm{v}^{\mathrm{i}} = \mathrm{i} \cdot v \qquad (axial\ swelling) \tag{C-11}$$

$$\mathrm{v}^{\mathrm{i}} = \mathrm{v}^{0} \frac{\mathrm{n}-\mathrm{i}}{\mathrm{n}} (\gamma)^{\mathrm{i}} \qquad (radial\ swelling)$$

The third condition is that the void ratio at the boundary is kept constant once a critical value is reached. This condition can be expressed for each geometry as:

$$[q_w^{n-1} - q_w^n] = e_M[q_s^{n-1} - q_s^n] \qquad (axial) \tag{C-12}$$

$$[r^1 q_w^1 - r^0 q_w^0] = e_M[r^1 q_s^1 - r^0 q_s^0] \qquad (radial)$$

Derived expressions for the unit-velocities for each geometry (v and v^0) are given below.

Several quantities were used for both geometries and almost all of these were defined for the elements. For the axial geometry these were: coordinate (x), length (l), displacement (u), dry mass (m), void ratio (e), axial path variable (f_x), suction (s), axial stress (σ_x), lateral stress (σ_y), and shear stress (τ). In addition, strains and strain increments (ε and Δε), as well as clay potentials (both axial Ψ_x and lateral Ψ_y) were also defined on the elements, but these were not saved for the output from the algorithm. Only the velocities for water (q_w), solids (q_s) and the nodes (v) were defined on the nodes.

For the radial geometry the following quantities were defined for the elements: centre radius (r_c), length (l), displacement (u), dry mass (m), void ratio (e), suction (s), path variables (f_r,f_θ,f_z), stresses (σ_r,σ_θ,σ_z), shear stress (τ) and strains (ε_r,ε_θ,ε_z). In addition, strain increments (Δε) were also defined on the elements, but these were not saved. For the nodes, only the radii (r) were saved, in contrast to the velocities for water (q_w), solids (q_s) and the nodes (v) and for the displacement field representative for the nodes (r_t).

The following notation for indices was used in the models:

- i: element (0 to n-1) and nodes (0 to n);
- j: time step (0 to jmax)
- k: direction (x,y,z) or (r,θ,z)

The algorithm was divided in two phases: one constant length phase, and one cavity evolution phase, during which the boundary void ratio was fixed. The initial conditions were defined so that suction was zero and stresses in all directions were equal to the clay potential (f = 0) for the initial void ratio. The processes were driven by differences in suction which in turn were caused by the loss of dry mass from the boundary. The simulation ended once the modelled time reached a pre-defined value.

With this framework of discretization and boundary conditions, and after assigning initial conditions to all quantities, the analysis was performed in a series of time steps quantified with a time-increment (Δt), which was held constant during pre-defined intervals, or through-out the calculation. The following operations were successively performed during each time step:

1. Water velocities are calculated from the suction gradients. The solid velocity is given by the boundary condition.
2. Velocities of nodes (in case of cavity formation) are calculated from the velocities at the boundary element.
3. Coordinates and lengths are calculated from node velocities.
4. Solid masses and void ratios are calculated from coordinates, lengths, water and node velocities.
5. Strains and displacements are calculated from void ratios, coordinates and lengths.
6. Path variable and clay potentials are calculated from void ratios and strain increments.
7. The suction profile is integrated from the stress equilibrium relation, clay potentials and boundary condition.
8. Stresses are calculated from clay potentials and suction.

These operations are described in detail below.

C3 Numerical solution for plane geometry

Darcy's law, flow rates and node velocity

The water velocity at each node (except i = 0 and n) is calculated from the void ratio, suction, and coordinates in the previous time step:

$$q_w^{j,i} = \frac{K(\mathrm{e}^{\mathrm{j-1,i}}) + K(\mathrm{e}^{\mathrm{j-1,i-1}})}{2} \frac{\mathrm{s}^{\mathrm{j-1,i}} - \mathrm{s}^{\mathrm{j-1,i-1}}}{\mathrm{x}^{\mathrm{j-1,i}} - \mathrm{x}^{\mathrm{j-1,i-1}}} \frac{1}{\gamma_w} \tag{C-13}$$

where γ_w is the unit weight of water and K is the hydraulic conductivity. The water velocity at node i = 0 is zero. The solid velocity at the boundary (i = n) is given by the mass loss rate (r_m), the solid density (ρ_s) and the section area (A):

$$q_s^{j,n} = \frac{r_m}{A \cdot \rho_s} \tag{C-14}$$

$$q_w^{j,0} = 0$$

The velocity v is zero if the boundary void ratio is below e_M, otherwise this can be calculated as:

$$v^j = -\left(q_w^{j,n-1} + q_s^{j,n}\right) \frac{1 + e_M}{(\mathrm{n} - 1)\, e_M + \mathrm{n}} \quad \text{if } \mathrm{e}^{\mathrm{j,n-1}} \geq e_M \tag{C-15}$$

$$v^j = 0 \quad \text{if } \mathrm{e}^{\mathrm{j,n-1}} < e_M$$

The water velocity at the boundary is finally calculated from the solid velocity and the node velocity:

$$q_w^{j,n} = -q_s^{j,n} - \mathrm{n} \cdot v^j \tag{C-16}$$

Coordinates and lengths

The length of each element is updated:

$$\mathrm{l}^{\mathrm{j,i}} = \mathrm{l}^{\mathrm{j-1,i}} + v^j \cdot \Delta t \tag{C-17}$$

Based on the lengths, the coordinate of the centre of each element is calculated:

$$\mathrm{x}^{\mathrm{j,0}} = \frac{\mathrm{l}^{\mathrm{j,0}}}{2} \qquad \mathrm{x}^{\mathrm{j,i}} = \mathrm{x}^{\mathrm{j,i-1}} + \frac{\mathrm{l}^{\mathrm{j,i}} + \mathrm{l}^{\mathrm{j,i-1}}}{2} \tag{C-18}$$

Continuity, masses and void ratios

The dry mass in each element is updated based on the velocities of water and nodes:

$$\mathrm{m}^{\mathrm{j,i}} = \mathrm{m}^{\mathrm{j-1,i}} + \left[q_w^{j,i+1} - q_w^{j,i} + v^j\right] A \cdot \rho_s \cdot \Delta t \tag{C-19}$$

Based on the dry masses and lengths, the void ratio of each element is calculated:

$$\mathrm{e}^{\mathrm{j,i}} = \frac{\rho_s \cdot \mathrm{l}^{\mathrm{j,i}} \cdot A}{\mathrm{m}^{\mathrm{j,i}}} - 1 \tag{C-20}$$

Strains and displacements

Based on the void ratios, the axial strain and the strain increment of each element are calculated:

$$\varepsilon_x{}^{\mathrm{j,i}} = \frac{\mathrm{e}^{\mathrm{j,i}} - e_{init}}{1 + e_{init}} \qquad \Delta\varepsilon_x{}^{\mathrm{j,i}} = \frac{\mathrm{e}^{\mathrm{j,i}} - \mathrm{e}^{\mathrm{j-1,i}}}{1 + e_{init}} \tag{C-21}$$

The lateral strains and strain increments (i.e. k = y, z) are zero. Based on the lengths and the axial strains, the displacement for each element is calculated:

$$\mathrm{u}^{\mathrm{j,0}} = \frac{\varepsilon_x{}^{\mathrm{j,0}} \cdot \mathrm{l}^{\mathrm{j,0}}}{2} \qquad \mathrm{u}^{\mathrm{j,i}} = \mathrm{u}^{\mathrm{j,i-1}} + \frac{\varepsilon_x{}^{\mathrm{j,i}} \cdot \mathrm{l}^{\mathrm{j,i}} + \varepsilon_x{}^{\mathrm{j,i-1}} \cdot \mathrm{l}^{\mathrm{j,i-1}}}{2} \tag{C-22}$$

Clay potentials, suction profile and stresses

Based on the strain increments, the axial path variable for each element is updated.

$$\mathrm{f}_T^{\mathrm{j-1,i}} = \frac{\max\left[\mathrm{f}_x^{\mathrm{j-1,i}}, \mathrm{f}_y^{\mathrm{j-1,i}}, \mathrm{f}_z^{\mathrm{j-1,i}}\right] - \min\left[\mathrm{f}_x^{\mathrm{j-1,i}}, \mathrm{f}_y^{\mathrm{j-1,i}}, \mathrm{f}_z^{\mathrm{j-1,i}}\right]}{2} \qquad \text{(C-23)}$$

$$\mathrm{f}_P^{\mathrm{j-1,i}} = \frac{\max\left[\mathrm{f}_x^{\mathrm{j-1,i}}, \mathrm{f}_y^{\mathrm{j-1,i}}, \mathrm{f}_z^{\mathrm{j-1,i}}\right] + \min\left[\mathrm{f}_x^{\mathrm{j-1,i}}, \mathrm{f}_y^{\mathrm{j-1,i}}, \mathrm{f}_z^{\mathrm{j-1,i}}\right]}{2}$$

$$\gamma_k^{\mathrm{j-1,i}} = \mathrm{f}_T^{\mathrm{j-1,i}} + \mathrm{sgn}\left(\Delta\varepsilon_k{}^{\mathrm{j,i}}\right) \cdot \mathrm{f}_P^{\mathrm{j-1,i}} \qquad k = x, y, z \qquad \text{(C-24)}$$

$$\mathrm{f}_k^{\mathrm{j,i}} = \mathrm{f}_k^{\mathrm{j-1,i}} - \left[1 - \Phi\left(\gamma_k^{\mathrm{j-1,i}}\right) \cdot \gamma_k^{\mathrm{j-1,i}} + \mathrm{f}_k^{\mathrm{j-1,i}} \cdot \mathrm{sgn}\left(\Delta\varepsilon_k{}^{\mathrm{j,i}}\right)\right] \cdot K \cdot \Delta\varepsilon_k{}^{\mathrm{j,i}} \qquad \text{(C-25)}$$

$k = x, y, z$

Based on the void ratio and the path variables the clay potentials for each element are calculated:

$$\Psi_k^{j,i} = \Psi_M\left(\mathrm{e}^{\mathrm{j,i}}\right) + \mathrm{f}_k^{\mathrm{j,i}} \cdot \Psi_{\Delta/2}\left(\mathrm{e}^{\mathrm{j,i}}\right) \qquad k = x, y, z \qquad \text{(C-26)}$$

The final operation of each time step is essentially the stepwise integration of the suction profile, from the zero value at the boundary (i = n−1) to the innermost element (i = 0). The suction profile can be evaluated through root-finding of the following expression (for simplicity, the time index j is omitted):

$$\Psi_{\mathrm{x}}^{\mathrm{i+1}} - \Psi_{\mathrm{x}}^{\mathrm{i}} - \left(\mathrm{s}^{\mathrm{i+1}} - \mathrm{s}^{\mathrm{i}}\right) \qquad \text{(C-27)}$$

$$+ \frac{2}{d} \frac{\mathrm{l}^{\mathrm{i+1}} + \mathrm{l}^{\mathrm{i}}}{2} \frac{\min\left[K \cdot u^{i+1}, \left(\Psi_y^{\mathrm{i+1}} - s^{i+1}\right) \cdot tan\varphi\right] + \min\left[K \cdot u^{i}, \left(\Psi_y^{\mathrm{i}} - s^{i}\right) \cdot tan\varphi\right]}{2} = 0$$

The integration is performed as a stepwise root-finding:

$$s^{j,n-1} = 0 \qquad s^{j,i} = f\left(s^{j,i+1}\right) \qquad i = n - 2..0 \qquad \text{(C-28)}$$

Finally, the axial and lateral stresses, as well as the shear stress are calculated for each element.

$$\sigma_k^{j,i} = \Psi_k^{j,i} - s^{j,i} \qquad \tau^{j,i} = \min\left[K \cdot u^{j,i}, \sigma_y^{j,i} \cdot tan\varphi\right] \qquad \text{(C-29)}$$

C4 Numerical solution for radial geometry

Darcy's law and flow rates

The water velocity at each node (except i = 0 and n) is calculated from the void ratio, suction, and coordinates in the previous time step:

$$q_w^{j,i} = \frac{K\left(\mathrm{e}^{\mathrm{j-1,i}}\right) + K\left(\mathrm{e}^{\mathrm{j-1,i-1}}\right)}{2} \frac{\mathrm{s}^{\mathrm{j-1,i}} - \mathrm{s}^{\mathrm{j-1,i-1}}}{r_c{}^{\mathrm{j-1,i}} - r_c{}^{\mathrm{j-1,i-1}}} \frac{1}{\gamma_w} \qquad \text{(C-30)}$$

where γ_w is the unit weight of water and K is the hydraulic conductivity. The water velocity at node i = n is zero. The solid velocity at the boundary (i = 0) is given by the mass loss rate (r_m), the solid density (ρ_s), the thickness d and the radius:

$$q_s^{j,0} = \frac{r_m}{2\pi d \cdot r_{j-1,0} \cdot \rho_s} \qquad \text{(C-31)}$$

$$q_w^{j,n} = 0$$

The velocity v is zero if the boundary void ratio is below e_M, otherwise this can be calculated as:

$$\mathrm{v}^{j,0} = -\frac{(1 + e_M)(\gamma q_w^1 + q_s^0)}{1 + e_M \frac{n-1}{n} \gamma^2} \quad if\ \mathrm{e}^{\mathrm{j,n-1}} \geq e_M \qquad \text{(C-32)}$$

$$v^{j,0} = 0 \quad if\ \mathrm{e}^{\mathrm{j,0}} < e_M$$

The water velocity at the boundary is finally calculated from the solid velocity and the node velocity:

$$q_w^{j,0} = -q_s^{j,0} - v^{j,0} \tag{C-33}$$

Coordinates and lengths

The radius of each node is updated:

$$r^{j,i} = r^{j-1,i} + v^{j,0}\frac{n-i}{n}\left(\gamma^{j-1}\right)^{i} \cdot \Delta t \tag{C-34}$$

The ratio between the radiuses of two adjacent nodes (γ) is calculated from the outer and inner radii.

$$\gamma^{j} = \left(\frac{R_{out}}{r^{j,0}}\right)^{\frac{1}{n}} \tag{C-35}$$

The length (l) and the center radius (r_c) of each element is calculated:

$$l^{j,i} = r^{j,i+1} - r^{j,i} \tag{C-36}$$

$$r_c^{j,i} = \frac{r^{j,i+1} + r^{j,i}}{2}$$

Continuity, masses and void ratios

The dry mass in each element is updated based on the velocities of water and nodes:

$$m_s^{j,i} = m_s^{j-1,i} - 2\pi d \cdot \rho_s \cdot \Delta t \cdot r^{j,i} \cdot \left[q_w^{j,i} - \gamma^{j} q_w^{j,i+1} + v^{j,0}\left(\gamma^{j}\right)^{i}\left(\frac{n-i}{n} - \frac{n-i-1}{n}\left(\gamma^{j}\right)^{2}\right)\right] \tag{C-37}$$

Based on the dry masses and radii, the void ratio of each element is calculated:

$$e^{j,i} = \frac{\rho_s \cdot d \cdot \pi \cdot \left({r^{j,i+1}}^{2} - {r^{j,i}}^{2}\right)}{m^{j,i}} - 1 \tag{C-38}$$

Strains and displacements

Based on the radii for all nodes and the void ratio for all elements a displacement field representative for the nodes (u_t) is integrated inwards, starting from (u_t=0) at the outer radius:

$$u_t^{j,i} = \frac{2r^{0,i+1}u_t^{j,i+1} - \left({r^{0,i+1}}^{2} - {r^{0,i}}^{2}\right)\dfrac{e^{j,i} - e_0}{1 + e_0}}{2r^{0,i}} \qquad u_t^{j,n} = 0 \quad i = n-1..0 \tag{C-39}$$

From this field, a displacement field representative for the elements (u) is calculated. In addition, the radial strain (ε_r) and the tangential strain (ε_θ) are also calculated:

$$u^{j,i} = \frac{u_t^{j,i+1} + u_t^{j,i}}{2} \quad \varepsilon_r^{j,i} = \frac{u_t^{j,i+1} - u_t^{j,i}}{r^{0,i+1} - r^{0,i}} \quad \varepsilon_\theta^{j,i} = \frac{u_t^{j,i+1} + u_t^{j,i}}{r^{0,i+1} + r^{0,i}} \quad \varepsilon_z^{j,i} = 0 \tag{C-40}$$

Strain increments are calculated from the strains in the current and the previous time step:

$$\Delta\varepsilon_k^{j,i} = \varepsilon_k^{j,i} - \varepsilon_k^{j-1,i} \qquad k = r, \theta, z \tag{C-41}$$

Clay potentials, suction profile and stresses

Based on the strain increments, the path variables for all directions in each element are updated.

$$f_T^{j-1,i} = \frac{\max\left[f_r^{j-1,i}, f_\theta^{j-1,i}, f_z^{j-1,i}\right] - \min\left[f_r^{j-1,i}, f_\theta^{j-1,i}, f_z^{j-1,i}\right]}{2} \tag{C-42}$$

$$f_P^{j-1,i} = \frac{\max\left[f_r^{j-1,i}, f_\theta^{j-1,i}, f_z^{j-1,i}\right] + \min\left[f_r^{j-1,i}, f_\theta^{j-1,i}, f_z^{j-1,i}\right]}{2}$$

$$\gamma_k^{\mathrm{j-1,i}} = \mathrm{f}_T^{\mathrm{j-1,i}} + \mathrm{sgn}\left(\Delta\varepsilon_k{}^{\mathrm{j,i}}\right) \cdot \mathrm{f}_P^{\mathrm{j-1,i}} \qquad k = r, \theta, z \tag{C-43}$$

$$\mathrm{f}_k^{\mathrm{j,i}} = \mathrm{f}_k^{\mathrm{j-1,i}} - \left[1 - \Phi\left(\gamma_k^{\mathrm{j-1,i}}\right) \cdot \gamma_k^{\mathrm{j-1,i}} + \mathrm{f}_k^{\mathrm{j-1,i}} \cdot \mathrm{sgn}\left(\Delta\varepsilon_k{}^{\mathrm{j,i}}\right)\right] \cdot K \cdot \Delta\varepsilon_k{}^{\mathrm{j,i}} \tag{C-44}$$

$$k = r, \theta, z$$

$$\Psi_k^{j,i} = \Psi_M\left(\mathrm{e}^{\mathrm{j,i}}\right) + \mathrm{f}_k^{\mathrm{j,i}} \cdot \Psi_{\Delta/2}\left(\mathrm{e}^{\mathrm{j,i}}\right) \qquad k = r, \theta, z \tag{C-45}$$

The final operation of each time step is essentially the stepwise integration of the suction profile, from the zero value at the boundary (i=0) to the innermost element (i=n−1). The suction profile can be evaluated through root-finding of the following expression (for simplicity, the time index j is omitted):

$$\begin{aligned}&\left(\Psi_r^{i+1} - \Psi_r^i\right) - \left(s^{i+1} - s^i\right) + \frac{l^{i+1} + l^i}{2 \cdot r^i}\left(\frac{\Psi_r^{i+1} + \Psi_r^i}{2} - \frac{\Psi_\theta^{i+1} + \Psi_\theta^i}{2}\right) \\ &- \frac{2}{d}\frac{l^{i+1} + l^i}{2}\frac{\min\left[-K \cdot u^{i+1}, \left(\Psi_z^{\mathrm{i+1}} - s^{i+1}\right) \cdot tan\varphi\right] + \min\left[-K \cdot u^i, \left(\Psi_z^{\mathrm{i}} - s^i\right) \cdot tan\varphi\right]}{2} = 0\end{aligned} \tag{C-46}$$

The integration is performed as a stepwise root-finding:

$$s^{j,0} = 0 \qquad s^{j,i} = f\left(s^{j,i-1}\right) \qquad i = 1..n-1 \tag{C-47}$$

Finally, the stresses and the shear stress are calculated for each element.

$$\sigma_k^{j,i} = \Psi_k^{j,i} - s^{j,i} \qquad \tau^{j,i} = \min\left[-K \cdot u^{j,i}, \sigma_z^{j,i} \cdot tan\varphi\right] \tag{C-48}$$

Appendix D

Analytical void ratio profiles

D1 Plane geometry with friction

The stress equilibrium for axial swelling is described with the following equation in which τ is the shear stress at the lateral boundary

$$\frac{\partial \sigma_x}{\partial x} + \frac{2\tau}{d} = 0 \quad \text{(D-1)}$$

This is simplified for the condition that s = 0, which means that the axial clay potential is equal to the axial stress. The stress gradient can then be developed as the product of the derivative of the clay potential and the void ratio gradient:

$$\frac{\partial \sigma_x}{\partial x} = \left[\frac{\mathrm{d}\Psi_M}{de} + f_x \cdot \frac{\mathrm{d}\Psi_{\Delta/2}}{de}\right]\frac{\partial e}{\partial x} \quad \text{(D-2)}$$

The shear stress in assumed to equal a fully develop wall friction, i.e. the product of the lateral clay potential and the tangent of friction angle. And since no swelling takes place in lateral direction the corresponding path variable (f_y) is assumed to be zero, which gives:

$$\frac{2\tau}{d} = \frac{2\tan\varphi}{d}\Psi_M \quad \text{(D-3)}$$

By combining the previous three equations the following relation between two axial coordinates (x_0 and x_1) and two void ratios (e_0 and e_1) can be derived:

$$x_1 = x_0 + \frac{d}{2\tan\varphi}\int_{e_0}^{e_1} \frac{\frac{\mathrm{d}\Psi_M}{de} + f_x \cdot \frac{\mathrm{d}\Psi_{\Delta/2}}{de}}{\Psi_M} de \quad \text{(D-4)}$$

Moreover, since the lateral strains and paths variables are zero and the axial strain increments is assumed to be positive, the relation between the axial strain and path variables can be described by:

$$\frac{df_x}{d\varepsilon_x} + (1 + f_x) \cdot K = 0 \quad \text{(D-5)}$$

For the initial condition that $f_x = 0$ for $e = e_{init}$ this differential equation has the following solution:

$$f_x(\mathrm{e}) = \exp(-\mathrm{K} \cdot \varepsilon_x) - 1 = \exp\left(-\mathrm{K} \cdot \frac{e - e_{init}}{1 + e_{init}}\right) - 1 \quad \text{(D-6)}$$

This expression can be substituted into the x(e)-relation above.

D2 Radial geometry without friction

The stress equilibrium for radial swelling without wall friction is described with the following equation:

$$\frac{\partial \sigma_r}{\partial r} + \frac{\sigma_r - \sigma_\theta}{r} = 0 \quad \text{(D-7)}$$

This is simplified for the condition that s = 0, which means that the radial clay potential is equal to the radia stress. The stress gradient can then be developed as the product of the derivative of the clay potential and the void ratio gradient:

$$\frac{\partial \sigma_r}{\partial r} = \left[\frac{\mathrm{d}\Psi_M}{de} + f_r \cdot \frac{\mathrm{d}\Psi_{\Delta/2}}{de}\right]\frac{\partial e}{\partial r} \quad \text{(D-8)}$$

The difference between the radial and the tangential stress is assumed to correspond to fully developed shear strength and thereby equal to the half-allowed span:

$$\frac{\sigma_r - \sigma_\theta}{r} = -\frac{\Psi_{\Delta/2}}{r} \tag{D-9}$$

By combining the previous three equations the following relation between two radial coordinates (r_0 and r_1) and two void ratios (e_0 and e_1) can be derived:

$$r_1 = r_0 \cdot \exp\left[\int_{e_0}^{e_1} \frac{\frac{\mathrm{d}\Psi_M}{de} + f_r \cdot \frac{\mathrm{d}\Psi_{\Delta/2}}{de}}{\Psi_{\Delta/2}} de\right] \tag{D-10}$$

There is no simple expression for the relation between the f_r and the void ratio. However, results from the numerical models for radial swelling, analyzed in this work indicate that the f_r-variable tend to reach a level of approximately −0.6.

D3 Radial geometry with friction

The stress equilibrium for radial swelling with wall friction is described with the following equation:

$$\frac{\partial \sigma_r}{\partial r} + \frac{\sigma_r - \sigma_\theta}{r} - \frac{2\tau}{d} = 0 \tag{D-11}$$

As previously, the stress gradient can then be developed as the product of the derivative of the clay potential and the void ratio gradient:

$$\frac{\partial \sigma_r}{\partial r} = \left[\frac{\mathrm{d}\Psi_M}{de} + f_r \cdot \frac{\mathrm{d}\Psi_{\Delta/2}}{de}\right]\frac{\partial e}{\partial r} \tag{D-12}$$

As previously, the next two terms can be replaced with an expression with the void ratio dependent clay potential functions, the radius and the friction angle:

$$\frac{\sigma_r - \sigma_\theta}{r} - \frac{2\tau}{d} = -\frac{\Psi_{\Delta/2}}{r} - \frac{2\tan\varphi}{d}\Psi_M \tag{D-13}$$

By combining the previous three equations the following expression for the void ratio gradient can be derived:

$$\frac{\partial e}{\partial r} = \frac{\frac{\Psi_{\Delta/2}}{r} + \frac{2\tan\varphi}{d}\Psi_M}{\frac{\mathrm{d}\Psi_M}{de} + f_r \cdot \frac{\mathrm{d}\Psi_{\Delta/2}}{de}} \tag{D-14}$$

This can easily be integrated with a numerical scheme. As previously, a f_r-value of approximately −0.6 appears to be a relevant level.

References

SKB's (Svensk Kärnbränslehantering AB) publications can be found at www.skb.com/publications.

ABAQUS, 2017. Dassault Systèmes Simulia Corp.

Birgersson M, Karnland O, Nilsson U, 2010. Freezing of bentonite. Experimental studies and theoretical considerations. SKB TR-10-40, Svensk Kärnbränslehantering AB.

Börgesson L, Johannesson L, Sandén, T, Hernelind J, 1995. Modelling of the physical behaviour of water saturated clay barriers. Laboratory tests, material models and finite element application. SKB TR 95-20, Svensk Kärnbränslehantering AB.

Börgesson L, Åkesson M, Hernelind J, 2020. EBS TF – THM modelling. Homogenisation task. SKB P-18-05, Svensk Kärnbränslehantering AB.

Dueck A, Börgesson L, Kristensson O, Malmberg D, Åkesson M, Hernelind J, 2019. Bentonite homogenisation. Laboratory study, model development and modelling of homogenisation processes. SKB TR-19-11, Svensk Kärnbränslehantering AB.

Karnland O, Muurinen A, Karlsson F, 2005. Bentonite swelling pressure in NaCl solutions – experimentally determined data and model calculations. In Alonso E E, Ledesma A (eds). Advances in understanding engineered clay barriers: Proceedings of the International Symposium on Large Scale Field Tests in Granite, Sitges, Barcelona, 12–14 November 2003. London: Taylor & Francis, 241–256.

Neretnieks I, Liu L, Moreno L, 2009. Mechanisms and models for bentonite erosion. SKB TR-09-35, Svensk Kärnbränslehantering AB.

Neretnieks I, Moreno L, Liu L, 2017. Clay erosion – impact of flocculation and gravitation. SKB TR-16-11, Svensk Kärnbränslehantering AB.

SKB, 2010. Corrosion calculations report for the safety assessment SR-Site. SKB TR-10-66, Svensk Kärnbränslehantering AB.

SKB, 2011. Long-term safety for the final repository for spent nuclear fuel at Forsmark. Main report of the SR-Site project. SKB TR-11-01, Svensk Kärnbränslehantering AB.

Åkesson M, Kristensson O, Börgesson L, Dueck A, Hernelind J, 2010a. THM modelling of buffer, backfill and other system components. Critical processes and scenarios. SKB TR-10-11, Svensk Kärnbränslehantering AB.

Åkesson M, Börgesson L, Kristensson O, 2010b. SR-Site Data report. THM modelling of buffer, backfill and other system components. SKB TR-10-44, Svensk Kärnbränslehantering AB.